KU LEUVEN

FACULTEIT INGENIEURSWETENSCHAPPEN

Epitaxial metal template development for Graphene growth

Bart Vermeulen

Thesis voorgedragen tot het behalen van de graad van Master of Science in de nanowetenschappen en de nanotechnologie, afstudeerrichting burgerlijk ingenieur

Promotor:
Prof. Dr. Stefan De Gendt

Assessoren:
Prof. Dr. Ir. Marc Heyns
Prof. Dr. Chris Van Haesendonck

Begeleider:
Dr. Ir. Steven Brems

Academiejaar 2014 – 2015

© Copyright KU Leuven

Without written permission of the thesis supervisor and the author it is forbidden to reproduce or adapt in any form or by any means any part of this publication. Requests for obtaining the right to reproduce or utilize parts of this publication should be addressed to Faculteit Ingenieurswetenschappen, Kasteelpark Arenberg 1 bus 2200, B-3001 Heverlee, +32-16-321350.

A written permission of the thesis supervisor is also required to use the methods, products, schematics and programs described in this work for industrial or commercial use, and for submitting this publication in scientific contests.

Zonder voorafgaande schriftelijke toestemming van zowel de promotor als de auteur is overnemen, kopiëren, gebruiken of realiseren van deze uitgave of gedeelten ervan verboden. Voor aanvragen tot of informatie i.v.m. het overnemen en/of gebruik en/of realisatie van gedeelten uit deze publicatie, wend u tot Faculteit Ingenieurswetenschappen, Kasteelpark Arenberg 1 bus 2200, B-3001 Heverlee, +32-16-321350.

Voorafgaande schriftelijke toestemming van de promotor is eveneens vereist voor het aanwenden van de in deze masterproef beschreven (originele) methoden, producten, schakelingen en programma's voor industrieel of commercieel nut en voor de inzending van deze publicatie ter deelname aan wetenschappelijke prijzen of wedstrijden.

Preface

This Master's thesis explores the production of metal templates suitable for epitaxial Graphene Chemical Vapor Deposition, during the last year of my Master's degree in Nanoscience and Nanotechnology, at KU Leuven. The work reported in this thesis was carried out at imec, Belgium, and occasionally at the department of Physics of KU Leuven.

The topic of Graphene is indubitably one of the most fascinating and challenging ones that I could investigate in this time and place. The research on epitaxial metal templates is not closely related to my background as a (nano-)electronics engineer, which makes it even more interesting. It allowed me to broaden my knowledge and practical skills in a way I could not have expected.

Of course, it has not always been easy. Experiments would fail without a warning. Critical tools would go out of order at the moment they are needed most. Results where not a single pattern would be discernable. And these are only a few examples of the daily torments of research. Fortunately, a great many people have supported me throughout the year, who deserve my utmost gratitude.

I would like to thank first of all Dr. Steven Brems, my supervisor at imec, who through his brilliant daily advice set and kept me on the right tracks. Special thanks go to my promotor, Prof. Stefan De Gendt, who through his priceless counsel guided me to a successful completion of this project. I would also like to thank Prof. Chris Van Haesendonck for granting me access to the Microscience Lab in the Physics department of KU Leuven, who along with Prof. Marc Heyns showed great interest in my work.

From imec, I would like to thank Ken Verguts and Nandi Vrancken for the constant collaboration concerning Graphene CVD, Kim Baumans for the systematic assistance in case of processing-related issues, Anja Vanleenhove for the assistance related to XPS characterisation and my fellow thesis and internship students for stimultating me to give it more than my best shot.

From the department of physics I would like to thank Koen Schouteden for performing STM measurements, and for the valuable discussions concerning the results thereof. I would also like to thank Stijn Vandezande for his patience and useful input concerning the use of *Cu* sputtering tools at KU Leuven.

Finally, I would like to express my greatest gratitude to all my friends and especially my entire family. From the beginning of my studies, they have supported me and challenged me to reach results I would often not hope to achieve myself. For this, one can only trust their family.

Bart Vermeulen

Contents

Preface i

Abstract vii

Samenvatting viii

List of Figures ix

List of Tables xiii

List of Abbreviations and Symbols xiv

1 Introduction 1
- 1.1 Why Graphene? . . . 2
  - 1.1.1 Properties . . . 2
  - 1.1.2 Production methods . . . 4
    - Chemical Vapor Deposition . . . 5
    - Requirements for the optimal template . . . 5
- 1.2 Problem Statement . . . 6
- 1.3 Objective . . . 6
- 1.4 Modus Operandi . . . 6
  - 1.4.1 Substrate selection and preparation . . . 7
  - 1.4.2 Catalyst selection and deposition . . . 7
  - 1.4.3 Graphene growth . . . 9
  - 1.4.4 Characterization . . . 9
  - 1.4.5 Starting point . . . 9

2 Literature Review 11
- 2.1 Epitaxial Cu Deposition . . . 12
  - 2.1.1 The Cu on Sapphire system . . . 12
    - Orientation Relationships . . . 13
    - Parametric Targets . . . 14
  - 2.1.2 Influence of the substrate . . . 15
    - Roughness . . . 15
    - Termination . . . 15
  - 2.1.3 Processing the substrate . . . 16
    - Cleaning . . . 16
    - Grinding/CMP . . . 17
    - Ion Milling . . . 17

Annealing 17
Oxygen Plasma Cleaning 18
2.1.4 Sputtering 18
Sputtering Pressure 19
Temperature 19
Target-to-substrate Distance 20
Sputtering Power 20
Sputtering Rate 21
2.1.5 Challenges 21
2.2 Graphene Growth 22
2.2.1 Chemical Vapor Deposition (CVD) 22
Pre-growth anneal 23
2.2.2 Influence of the template 23
Chemical termination 24
Crystallinity 24
OR Mix 24
Roughness 25
2.2.3 Challenges 25
2.3 Conclusion 25

3 Preparation of the Al_2O_3 substrate **27**
3.1 Original state 27
3.1.1 Crystallinity 28
3.1.2 Surface roughness 28
3.1.3 Surface termination 28
3.2 Cleaning 31
3.2.1 Motivation 31
3.2.2 Effect 31
3.3 Annealing 33
3.3.1 Motivation 33
3.3.2 Effect 33
Low Temperature Anneal (LTA) 33
High Temperature Anneal (HTA) 34
Oxygen Plasma Treatment (OPT) 36
3.4 Sources of variability 38
3.5 *In situ* Vacuum Anneal 38
3.5.1 Motivation 38
3.5.2 Effect 39
3.6 Ion Milling 39
3.6.1 Motivation 39
3.6.2 Effect 39
3.7 Conclusion 40

4 Deposition of the Cu layer **41**
4.1 Objective 42
4.1.1 State-of-the-Art 42

4.1.2 Thesis objective 43
4.2 Towards the State-of-the-Art 44
4.2.1 Stability of the Oxygen termination 44
4.2.2 *In situ* vacuum anneal 46
4.2.3 Temperature Window 46
4.3 Towards the thesis objective 47
4.4 Influence of intrinsic parameters 48
4.5 Influence of extrinsic parameters 49
4.6 Conclusion 51
4.6.1 Objective 51
4.6.2 Influence of the substrate preparation 51
4.6.3 Influence of the deposition parameters 51

5 Graphene Chemical Vapor Deposition 53
5.1 Thesis objective 54
5.1.1 Cu quality 54
5.1.2 Stability 55
5.2 Towards the State-of-the-Art: Oxygen treatments 55
5.3 Towards the thesis objective 56
5.4 Influence of intrinsic parameters 57
5.4.1 Growth time 57
5.4.2 Conclusion 58
5.5 Influence of extrinsic parameters 59
5.5.1 Sapphire substrate preparation 59
Why cleaning? 61
5.5.2 *Cu* deposition 62
5.5.3 Conclusion 64
5.6 Graphene quality 64
5.6.1 STM 64
5.6.2 Raman 65
5.7 Issues 67
5.7.1 Yield 67
5.7.2 Necessity of epitaxy 67
5.7.3 Transfer 67
5.8 Conclusion 68

6 Conclusion 69
6.1 Objective 69
6.1.1 State-of-the-Art 70
Issues 70
6.1.2 Thesis objective 70
Process flow 72
6.2 Outlook 73

7 Publishable Summary 75

A Methods and Materials 83

A.1 Materials . . . 84
A.1.1 Sapphire . . . 84
General properties . . . 84
Unit Cell . . . 84
The (0001) surface . . . 85
A.1.2 *Cu* . . . 85
General properties . . . 85
Unit Cell . . . 86
The (111) plane . . . 87
A.1.3 Graphene . . . 87
General properties . . . 87
Unit Cell . . . 88
A.2 Processing steps . . . 88
A.2.1 Acid Clean . . . 89
Sulphuric Acid . . . 89
Phosphoric Acid . . . 89
A.2.2 Anneal . . . 89
Sapphire substrate . . . 89
LTA . . . 89
HTA . . . 89
Vacuum . . . 89
Deposited *Cu* layer . . . 90
A.2.3 Other . . . 90
Oxygen Plasma . . . 90
Ion Milling . . . 90
A.2.4 Sputtering . . . 90
Microscience Lab . . . 90
Nimbus tools . . . 90
A.2.5 Graphene growth . . . 91
A.3 Process Flows . . . 91
A.3.1 From Miller et al.[1] . . . 91
A.3.2 Towards the State-of-the-Art . . . 91
Immediate deposition . . . 91
Vacuum Anneal . . . 91
A.3.3 Epitaxial *Cu* . . . 91
Microscience Lab . . . 92
Room Temperature . . . 92
High Temperature . . . 92
Nimbus tools . . . 92
Nimbus 310 . . . 92
Nimbus 314 . . . 92
A.3.4 Graphene growth . . . 92
A.4 Atomic Force Microscopy . . . 92
A.4.1 Modes of operation . . . 93
Contact Mode . . . 93

Tapping Mode . . . 94
Non-Contact Mode . . . 94
A.4.2 Beam deflection measurement . . . 95
A.4.3 Tool technical aspects . . . 95
A.5 X-Ray Photoelectron Spectroscopy . . . 96
A.5.1 Experimental system . . . 96
A.5.2 Modes of operation . . . 97
A.5.3 Tool technical aspects . . . 98
A.6 X-Ray Diffraction . . . 98
A.6.1 Diffraction . . . 99
Scattering and interference . . . 99
Bragg Condition . . . 100
Von Laue Condition . . . 101
Allowed reflections . . . 102
Diffraction as a Fourier Transform . . . 103
A.6.2 Modes of operation . . . 103
2θ scan . . . 103
Φ scan . . . 104
A.6.3 Tool technical aspects . . . 105
A.7 Raman Spectroscopy . . . 106
A.7.1 Scattering . . . 106
A.7.2 Raman Shift . . . 107
A.7.3 Graphene . . . 107
A.7.4 Tool technical aspects . . . 108
A.8 Scanning Tunneling Microscopy . . . 109
A.8.1 Tunneling and the principle of operation . . . 109
A.8.2 Additional possibilities . . . 110
A.8.3 Tool technical aspects . . . 110
A.9 Conclusion . . . 110
B Crystallography of Sapphire **113**
B.1 XRD background of pure $\alpha - Al_2O_3\,(0001)$ . . . 114
B.2 Analysis of the features . . . 114
B.3 XRD characteristic of a $Cu\,(111)\,/\alpha - Al_2O_3\,(0001)$ stack . . . 117
B.4 Conclusion . . . 119
C Additional Figures **121**
Bibliography **131**

Abstract

Graphene holds a great potential as a future electronics material. It has been discovered more than ten years ago, and nowadays numerous institutes engaged into intensive research on the best production method for Graphene. Chemical Vapor Deposition is widely accepted as the most promising contender, and the $Cu\,(111)\,/\alpha - Al_2O_3\,(0001)$ material stack is seen as an interesting template for growing Graphene through CVD.

In this thesis, the best way to produce a monocrystalline Cu on Sapphire template for Graphene growth is investigated. Two classes of template production methods are studied, the main difference residing in the treatment of the Sapphire substrate before depositing the Cu layer.

In the first class, the aim is to produce an Oxygen terminated Sapphire substrate. This is, according to many theoretical and experimental results to date, the most suitable for Cu epitaxy. The Oxygen termination is, unfortunately, thermodynamically unstable. Any treatment prior Cu deposition aimed at promoting this Oxygen termination results in completely unreliable Cu crystalline structures.

In the second class, the hydroxylated Aluminum termination of Sapphire is used. The undeniable advantage of the latter is its stability. This greatly improves the reproducibility of results and, most importantly, proved to significantly promote Cu epitaxy. The Cu layers deposited on OH-Aluminum terminated Sapphire display wafer-sized untwinned single crystals when heated up to Graphene CVD temperatures.

The quality of these Cu layers is investigated with XRD and optical microscopy. The former allows to determine that the Cu was grown epitaxially, without twinning of the Orientation Relationships (ORs). This had, to this date, never been done. The latter technique confirms that the defects are, just like in many standard semiconductor process flows, concentrated along the edges of the templates.

With these results, the issue of polycrystalline Cu templates negatively influencing the quality of Graphene can be considered solved. The next steps are to optimize the Graphene growth procedure, the transfer methods, and ultimately to expand the conclusions on epitaxy to other sets of materials.

Samenvatting

Grafeen is een materiaal dat immense mogelijkheden biedt voor de elektronica industrie. Net meer dan tien jaar na de ontdekking ervan, wordt in vele instituten hoogtechnologisch onderzoek gevoerd naar de beste manier om Grafeen te maken. *Chemical Vapor Deposition*[1] wordt algemeen beschouwd als de beste mogelijkheid, en de $Cu\,(111)\,/\alpha - Al_2O_3\,(0001)$ materiaalstapel is een interessant patroon waarop Grafeen via CVD kan groeien.

In deze thesis wordt de beste manier om monokristallijn Koper op Saffier te deponeren onderzocht. Twee manieren om dit patroon te produceren zullen bekeken worden, het verschil zit in de voorbereiding van het Saffier substraat voordat Koper gedeponeerd wordt.

Ten eerste wordt er gestreefd naar een Zuurstofterminatie van het Saffier oppervlak. Vele theoretische en experimentele resultaten duiden er vandaag de dag op dat dit de beste optie zou zijn voor epitaxiale Koper depositie. Helaas blijkt deze Zuurstofterminatie thermodynamisch onstabiel te zijn. Dit zorgt ervoor dat procedures met als doel een Zuurstofterminatie een volledig onvoorspelbaar resulterende Koperkwaliteit veroorzaken.

Vervolgens wordt er gestreefd naar een gehydroxyleerde Aluminiumterminatie van het Saffier oppervlak. Het onbetwistbaar voordeel hiervan is de stabiliteit van deze oppervlakteterminatie. Dit zorgt voor significant betrouwbaardere resultaten, en blijkt achteraf ook epitaxiale groei van Koper te vergemakkelijken. Deze Koperlagen werden afgebakken tijdens Grafeen CVD procedures, met resulterende kristalgroottes enkel beperkt door de dimensies van de Saffier substraatwafers.

De kwaliteit van deze Cu lagen werd door middel van XRD[2] en optische microscopie geanalyseerd. Met XRD kon de kristallijne structuur van Koper beoordeeld worden, namelijk monokristallijn zonder twinning. Met optische microscopie kon de locatie van de meeste defecten bekeken worden. Net als in vele halfgeleider processen, konden de meeste defecten tegen de rand van de substraatwafers gevonden worden.

Met deze resultaten kan het probleem de negatieve invloed van polykristallijne Koper patronen op de kwaliteit van Grafeen als opgelost beschouwd worden. Toekomstig onderzoek zal zich focusen op de parameters voor Grafeengroei en -transfer, en zou uiteindelijk de conclusies van dit werk kunnen uitbreiden naar andere materiaalcombinaties.

[1] Vaktermen worden niet naar het Nederlands vertaald
[2] X-Ray Diffraction; Afkortingen van vaktermen worden niet naar het Nederlands vertaald

List of Figures

1.1 The honeycomb lattice of Graphene, and the corresponding first Brillouin zone. From Castro Neto et al. [2]. 3
1.2 The band structure of Graphene is the source of its interesting properties. From Castro Neto et al. [2]. 4
1.3 The final stack of materials to be produced during this thesis. Adapted from Ago et al. [3]. 5
1.4 Common metals used for catalysing the dissociation of a Graphene-CVD precursor. 7

2.1 Graphical representation of the Orientation Relationships of $Cu\,(111)$ onto $\alpha - Al_2O_3\,(0001)$[4]. 13
2.2 Influence of the Ar pressure and substrate temperature (normalized with respect to the melting point of the sputtered species in its bulk form) on the structure of a sputtered metallic layer. From Thornton et al. [5]. . . 20

3.1 AFM image of the surface of pristine Sapphire wafers. 28
3.2 Angle-Resolved XPS measurement of the surface of pristine Sapphire wafers. The low exit angles stand for the bulk concentrations, while the higher exit angles represent the surface concentrations. 29
3.3 Normalized Angle-Resolved XPS spectra of the Oxygen signal for pristine Sapphire wafers. The 22° curve describes the bulk concentrations and the 78° describes the surface concentrations. 30
3.4 Vertical section of the Unit Cell of Sapphire[6]. 30
3.5 AFM image of the surface of chemically cleaned Sapphire wafers. 31
3.6 Angle-Resolved XPS spectra of cleaned samples for Oxygen (normalized) and surface Aluminum (absolute). 32
3.7 AFM image of the surface of Sapphire wafers after a chemical clean and a LTA. 33
3.8 Angle-Resolved XPS spectra of cleaned + LTA samples for Oxygen (normalized) and surface Aluminum (absolute). 34
3.9 AFM image of the surface of Sapphire wafers after a chemical clean and a HTA. 35
3.10 Angle-Resolved XPS spectra of cleaned + HTA samples for Oxygen (normalized) and surface Aluminum (absolute). 35

3.11 AFM image of the surface of Sapphire wafers after a chemical clean and OPT. . . . 36
3.12 Angle-Resolved XPS spectra of cleaned + Oxygen plasma samples for Oxygen (normalized) and surface Aluminum (absolute). . . . 37
3.13 Angle-Resolved XPS spectra of cleaned + Oxygen plasma samples for surface Fluorine. . . . 37
3.14 AFM image of the surface of Sapphire wafers after a chemical clean and an Ion Milling treatment. . . . 39

4.1 XRD Line scan for as-deposited (left) and annealed (right) $Cu\,(111)$ crystals for different substrate deposition temperatures. From Miller et al. [1]. . . . 42
4.2 XRD Line scan for an as-deposited sample that, upon annealing, adopts untwinned epitaxial $Cu\,(111)$ grains. . . . 43
4.3 Line scan of the as-deposited Cu structure, for two samples deposited after a LTA. (procedure in Appendix A.3.2). . . . 45
4.4 Line scan of the as-deposited Cu structure, for the different surface treatment procedures described in Chapter 3. . . . 46
4.5 XRD Line scan of the as-deposited Cu structure, for three samples deposited at slightly different substrate temperatures after an *in situ* vacuum anneal. . . . 47
4.6 XRD Line scan of the as-deposited Cu structure, for four samples deposited under different conditions. . . . 48
4.7 XRD Line scans of three samples with different substrate preparations. 50

5.1 XRD Line scan and 2θ-scan of an untwinned epitaxial Cu layer, after Graphene growth. . . . 54
5.2 XRD Line scan of an epitaxial Cu layer, after Graphene growth, for different surface treatment procedures described in Chapter 3. The curves for the as-deposited structures are given in Figure 4.4. . . . 55
5.3 XRD Line scans of annealed samples that underwent Cu deposition in different systems under different conditions. . . . 56
5.4 XRD Line scan of annealed epitaxial Cu layers for different Graphene growth durations. . . . 58
5.5 XRD Line scan of as-deposited Cu layers for different surface treatments. 59
5.6 XRD Line scan of annealed epitaxial Cu layers for different surface treatments. . . . 60
5.7 (a) Optical microscopy image of an annealed Cu layer, where the substrate was cleaned prior to Cu deposition. (b) Optical microscopy image of an annealed Cu layer, where the substrate was not cleaned prior to Cu deposition. (c) Giant grain. (d) AFM image of a grain boundary (Phase image in Fig. C.9). . . . 61
5.8 Optical microscopy image of an (annealed) Cu layer that is sputtered in the Microscience tool at $85°C$. The position of the PFL, and orientation of the grain boundaries of Cu in Sapphire coordinates are given in white. 63

5.9 (a) Three-Dimensional view of a Graphene layer grown on an epitaxial Cu (111) template. (b) STM image of a grain boundary (bright line) between two Graphene crystals. 65
5.10 Raman Spectra of graphene, with and without a Cu background and transferred onto SiO_2. 66

6.1 XRD Line scan of epitaxial Cu: OR-Ia. 71
6.2 Optical microscopy image of the edge of an epitaxial Cu layer 72

A.1 (a) Spacial distribution of the Aluminum ions in the rhombohedral Unit Cell. (b) Representation of the Sapphire basal plane (c-plane). Large circles are Oxygen ions, small filled circles Aluminum, and small empty circles the empty sites used to define the Unit cell. From Kronberg et al. [7]. 85
A.2 The Unit Cell of an FCC metal, in this case Cu. The lattice constant $a_0 = 361.5\ pm$ is indicated. 86
A.3 The (111)-plane of Cu is shown. The different layers of Cu atoms are displayed in different colors. 87
A.4 The Unit Cell of Graphene is indicated in dark red. The distance between two Carbon atoms is 146 pm and the lattice parameter $a_0 = 246 pm$. 88
A.5 Schematic of a typical AFM setup. From P. Eaton [8] 93
A.6 The photodetector, consisting of four separate photodiodes A, B, C, and D, can detect both vertical and lateral bending. From P. Eaton [8] . . . 95
A.7 The basic principle of XPS. An electron can be ripped off its atom by an incoming photon and detected. From H. Bender [9]. 96
A.8 When planar waves encounter objects (here slits in a screen) in the order or smaller than their wavelength, they act as sources for new spherical wavefronts. These wavefronts will interfere, in case there is more than one. From Van Holde [10]. 99
A.9 Two waves reflecting on Bragg planes. The angle of incidence (and of "reflection") is θ, so two waves will travel along paths of different lengths. From Van Holde [10]. 101
A.10 Diffraction of light waves due to the electron clouds of a one dimensional crystal of atoms. From Van Holde [10]. 102
A.11 Schematic representation of the four relevant $Cu(111)$ planes. The horizontal plane represents the sample surface. The three other planes are buried, and can be imaged by rotating the sample over an angle of 70.5°. 105
A.12 Schematic representation of the processes undergone by an **atom** which scatters a visible photon. 107
A.13 Typical Raman spectrum of a Graphene flake. From Chung et al. [11]. . 108
A.14 Schematic representation of an STM setup. From W. Vandervorst [9]. . 109
A.15 Tunneling current density in STM. From W. Vandervorst [9]. 110

B.1 Backgound signal from a Sapphire substrate. In the lower part of the figure, a zoomed characteristic in allows to identify the location of the repeated features. 114
B.2 Stereographic projection, with the c-plane taken as the reference plane (the centre). From Dobrovinska et al. [12]. 115
B.3 Tilt angle and respective 2θ scans on a Sapphire substrate. 116
B.4 Upgraded version of the stereographic procjection of Figure B.2. The stereographic projection is taken from [12]. 118
B.5 Phi scan of an epitaxial Cu (111) layer on Sapphire. Both the curves of Cu and the Sapphire background are shown. 120

C.1 Surface XPS spectra for C on pristine Sapphire wafers, after a chemical clean, and after three days of ageing in a Teflon container. 121
C.2 Surface XPS spectra for F on pristine Sapphire wafers, after a chemical clean, and after three days of ageing in a Teflon container. 122
C.3 XPS spectra for Oxygen. 123
C.4 XPS spectra for Aluminum. 124
C.5 XPS spectra for Carbon. 125
C.6 XPS spectra for Fluorine. 126
C.7 XPS profiles derived from the XPS spectra. 127
C.8 XRD Phi scan of the relative stability of the Oxygen and Aluminum terminations. The two first samples underwent exactly the same treatment and underwent Cu sputtering at exactly the same parameters. Nevertheless, due to the unstabel O termination, the results vary very strongly. The two last samples were simply cleaned, and then underwent Cu sputtering after the indicated time. The sputtering parameters were different than those of the two first samples. Regardless of the time spent before Cu deposition, the results are identical, as opposed to the results of the Oxygen annealed samples. 128
C.9 Phase image of a Cu grain boundary. The diagonal stripe in the middle of the figure is ascribed to a Graphene grain boundary. Original figure is Figure 5.7d. 129
C.10 AFM investigation of a grain boundary in an epitaxially grown Cu on Sapphire sample. The angle of 60° between the grain boundaries can be clearly seen in this image. The grain boundaries are approximately 30 nm deep, but are nevertheless visible under an optical microscope. 130

List of Tables

1.1 Properties of Graphene, compared to typical electronics materials. [2] . 2
1.2 Comparison of the important properties of potential catalysts. 8

2.1 Parameters for giant grain growth according to Miller et al. [1]. 15

3.1 Relative surface concentrations of atomic species. The error is in the order of 1%. 36

4.1 Comparison of the different Cu sputtering setups. 49

A.1 Physical properties of Sapphire [12]. 84
A.2 Physical properties of Cu [13]. 86
A.3 Physical properties of Graphene [2]. 88

List of Abbreviations and Symbols

Abbreviations

AFM	Atomic Force Microscopy
CTE	Coefficient of Thermal Expansion
CVD	Chemical Vapor Deposition
FCC	Face Centered Cubic
FWHM	Full Width at Half Maximum
GB	Grain Boundary
HCP	Hexagonal Close Packed
HTA	High-Temperature Anneal
IR	InfraRed
LTA	Low-Temperature Anneal
MOSFET	Metal Oxide Semiconductor Field Effect Transistor
OPT	Oxygen Plasma Treatment
OR	Orientation Relationship
PFL	Primary Flat Location
PMMA	Poly (Methyl Methacrylate)
RMS	Root Mean Square
RT	Room Temperature
sccm	Standard Cubic Centimeters per Minute
SE	Secondary Electrons
SPM	Scanning Probe Micrsocopy
TEM	Transmission Electron Micrsocopy
TSD	Target-to-Substrate Distance
UPW	Ultra Pure Water
XPS	X-Ray Photoelectron Spectroscopy
XRD	X-Ray Diffraction Spectroscopy

Symbols

μ	Adatom Mobility (Cu Sputtering)
PD	Path Difference (Bragg's law of Diffraction)

Chapter 1

Introduction

In this short introduction on the topic of this thesis -templates for Graphene growth- the motivation for growing Graphene is explained. This material has been fascinating scientists and engineers alike since it was discovered, ten years ago, by Geim and Novoselov [14](Nobel Prize in Physics, 2010). Here, some of the most interesting properties of Graphene are discussed, with the focus laying on its electronic properties, and how these could revitalise the electronics industry which is struggling to keep up with Moore's law.

The next step is to discuss how to actually make Graphene. The theoretically wonderful properties of this material are influenced by the production method in many ways (but mostly negatively). A suitable production method will be chosen, and the requirements related to the chosen production methods will be highlighted.

This discussion is followed by the problem statement, and the objective of this thesis. In the conclusion of this work, a reflection will be made concerning whether or not this objective was reached.

Finally, the method used to reach this objective is discussed. In the Modus Operandi section, the different work packages that make up the core of the activities conducted in this thesis are considered. The choice for the materials used in this thesis, which is of capital importance in the successful growth of Graphene, is defended.

1.1 Why Graphene?

Graphene can, without a doubt, be considered a wonder material. Its theoretical properties would allow to revolutionize more than one aspect of our modern society. As is often the case for potentially revolutionary breakthroughs in modern technology, a critical aspect related to its implementation tampers with the enthousiasm of the scientific community. In the case of Graphene, the issues related to producing a material with properties decently matching the theoretical ones prove to be more tenacious than expected.

1.1.1 Properties

The theoretical properties of Graphene are truly astonishing. The best way to get an accurate feeling of exactly how exceptionnal these are, is to compare Graphene with other materials typically used in the semiconductor industry. For this, Graphene is put up against typical metals (Cu and Al are commonly used for their good electrical properties) and today's workhorse of the semiconductor industry, Silicon, see Table 1.1. Some additional properties are given in Appendix A.1.3.

Table 1.1: Properties of Graphene, compared to typical electronics materials. [2]

Property	Graphene	Cu	Al	Si
Mobility $\left[\frac{cm^2}{Vs}\right]$	~200.000	44	13	$\frac{1400(e^-)}{450(h^+)}$
Thermal Conductivity $\left[\frac{W}{mK}\right]$	~5000	400	237	149
Young's Modulus $[GPa]$	1000	110-128	70	130-188
Tensile strength $[MPa]$	130.000	210	40-50	5000-9000
Bandgap $[eV]$	0-0.3 [15]	0	0	1.12

The reason for the enthousiasm for Graphene is obvious when its electronic properties are compared to those of conventional materials. The electrical and thermal mobilities/conductivities are orders of magnitude higher, as are the mechanical properties. Graphene can have a bandgap, or it can behave as a metal. It could be used both as a semiconductor for devices[1], and as a metal for interconnects.

In case of a semiconducting Graphene system, the exceptionally high charge carrier mobilities (compared to both metals and Si), would make it possible to make semiconductor circuits with attainable speeds far above the current standards[2]. In the light of Moore's law, this is one of the fundamental requirements for a successful semiconductor industry.

[1] This requires to tune the bandgap and increase its value, to make it easier to turn devices off.

[2] The mobilities decrease with increasing bandgap [16], but nevertheless represent a tremendous improvement compared to Si.

The origin of these properties can be found in the band structure of Graphene. It can be derived from the Graphene lattice (shown in Figure 1.1) by using the tight-binding approach. This falls outside of the scope of this work, and the curious reader is referred to the review paper of Castro Neto et al. [2]. The Graphene crystalline lattice (the so-called honeycomb lattice) in fact consists of two interpenetrating triangular lattices (indicated in the two colours of Figure 1.1). This gives Graphene a 120° rotational symmetry.

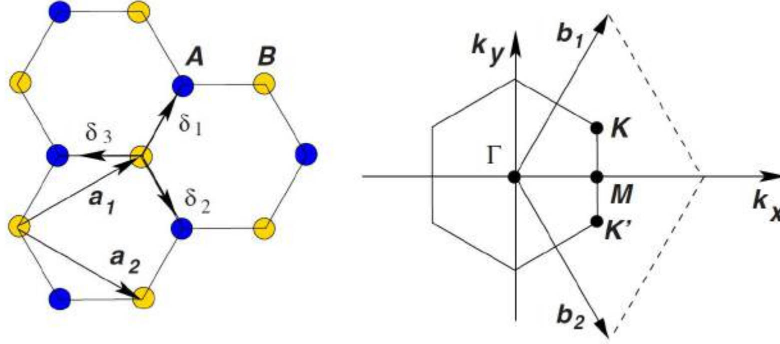

Figure 1.1: The honeycomb lattice of Graphene, and the corresponding first Brillouin zone. From Castro Neto et al. [2].

In the left figure, the lattice unit vectors $a\vec{_{1,2}}$ are shown , and the two colors indicate the two interwoven triangular lattices used to represent Graphene. On the right, the reciprocal lattice vectors $b\vec{_{1,2}}$ are drawn, and different interesting points are indicated. The $\vec{K}$ and $\vec{K}'$ points are called the Dirac points.

The energy dispersion relation of Graphene is given in Figure 1.2. The otherwise gapped structure displays interesting features in the Dirac points. There, the conduction and valence bands intersect, and locally the electronic dispersion relation is linear. A clearer view of such a $\vec{K}$ point can be found on the right side of the image. This locally linear dispersion relation is at the basis of the interest in Graphene, and is what allows this material to act either as a metal or a semiconductor, depending on the topology.

The topology of a Graphene system determines which states in momentum space are available for charge carriers [2]. One can think of it as which "section" of the band structure applies to a given system (imagine a vertical plane intersecting with the band structure, if it passes through a $\vec{K}$ point, the Graphene will be metallic, and vice versa). Additionally, the charge carriers located in $\vec{k}$ space close to the $\vec{K}$ points experience the effects of the locally linear dispersion relation. In a conventional semiconductor, the dispersion relation is parabolic.

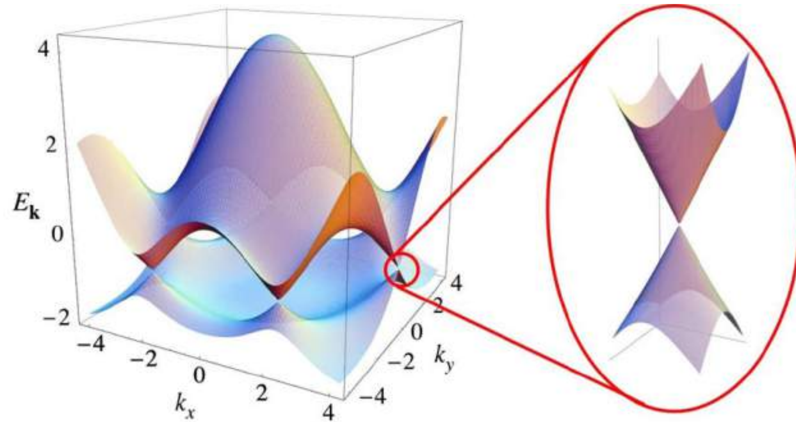

Figure 1.2: The band structure of Graphene is the source of its interesting properties. From Castro Neto et al. [2].

1.1.2 Production methods

The quality of a material is in many cases dominated by the production process, and this is no different for Graphene. The properties cited in Table 1.1 are theoretically calculated, and typically the measured properties of a real-world system are orders of magnitude worse than the theoretical ones.

One must therefore carefully choose the method of fabrication to apply. The three methods available at this time are: Mechanical exfoliation, Thermal evaporation, and Chemical Vapor Deposition (Molecular Beam Epitaxy has also been proposed, but very little is known about its potential). Mechanical exfoliation was developed by Geim and Novoselov [14], in the publication that earned them the Nobel Prize. This technique offers by far the highest quality of Graphene, but has the important drawback that it is neither scalable nor reproducible. For industrial purposes, it is therefore worthless.

Thermal evaporation of Si out of SiC wafers requires the aforementioned SiC wafers. These are expensive, and currently only available in small sizes. This technique therefore likely doesn't qualify for the industry either.

Chemical Vapor Deposition (CVD) is the last option, and the most viable one. This technique is scalable to any desired size of Graphene crystal, given the template can be made large enough. It is potentially very cheap, and can be optimized following many different paths. This is therefore the production method that is chosen for the work performed in this thesis.

Chemical Vapor Deposition

In CVD, a C containing precursor gas is flown over a template which catalyses the dissociation into Graphene Carbon and Hydrogen gas. A general form of this dissociation reaction is given below:

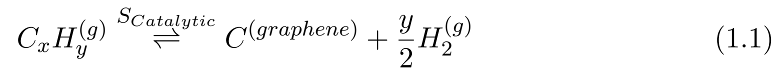

$$C_x H_y^{(g)} \overset{S_{Catalytic}}{\rightleftharpoons} C^{(graphene)} + \frac{y}{2} H_2^{(g)} \tag{1.1}$$

Many parameters are important in CVD, of which a few will be cited: the temperature in the reaction chamber, the pressure, the different gasses chosen for the reaction and their flow rates, and the growth time. Optimizing these falls outside of the scope of this thesis. Another (maybe even more) important factor is the template onto which the Graphene crystal is grown. This work focusses on the selection and production of the best suited template.

Requirements for the optimal template

The template used for Graphene growth has to fulfill a set of important constraints, most of which can be translated into requirements for the catalytic metal. A graphical representation of a suitable template is shown in Figure 1.3. As can be seen, the template consists of a stack of two different materials. The bottom "substrate" is used purely for mechanical purposes. The "catalyst" layer indeed doesn't need to be very thick (in the order of half a μm still, to improve recrystallisation, and compensate for sublimation), which in the case of an expensive catalyst, may be a considerable advantage.

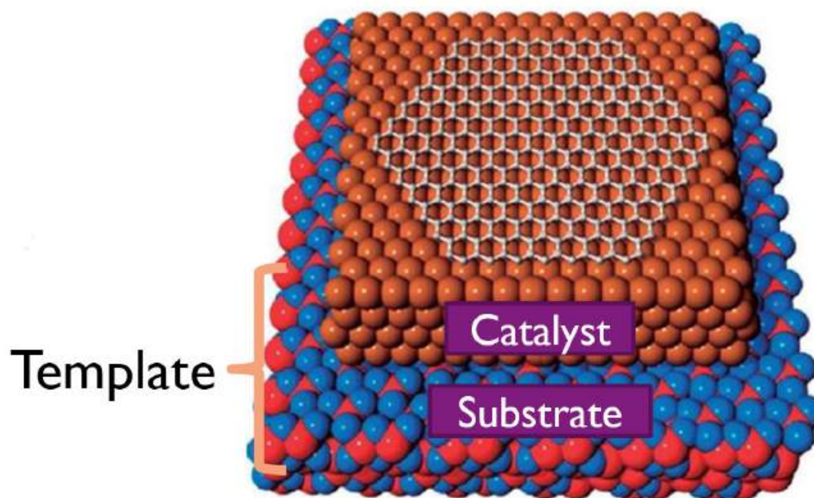

Figure 1.3: The final stack of materials to be produced during this thesis. Adapted from Ago et al. [3].

The templates, besides the obvious requirement that they should catalyze the dissociation of the precursor, should also be monocrystalline and atomically flat. Indeed, if a defectless two dimensional crystal must be grown, the slightest topology feature, or grain boundary may compromise the quality of the Graphene. Additionally, it should be physically and chemically stable, even under very harsh conditions (temperatures reaching above $1000°C$, reactive chemicals, etc.). The template should also have a low Carbon solubility, even at high temperatures. This will allow to easily limit the growth to one layer. Finally, from a purely industrial point of view, the template should be reusable and cheap.

The many and complex requirements cited in this section have, to this day, not been solved, let alone been solved together. This leads to the problem that will have to be solved in this work.

1.2 Problem Statement

The problem addressed in this work can be described as follows:

> The difficulty of growing wafer scale **monolayer monocrystalline** Graphene.

From the point of view of the template, this is translated in two sub-problems:

> The need for a monocrystalline catalyst/template.
> The absence of a clear pathway to **epitaxy**.

1.3 Objective

With this problem statement in mind, the objectives for this thesis can be set. The central goal is:

> to investigate the production of a template suitable for the growth of a large crystal of Graphene.

The optimal template to fulfill this objective would satisfy all the requirements of Section 1.1.2. Additionally, it should be compatible with the crystalline properties of Graphene, being its lattice parameter ($a_0 = 246\ pm$) and the symmetry of the Graphene lattice. The room temperature Coefficient of Thermal Expansion ($RT\ CTE = -6 * 10^{-6} K^{-1}$) should also be considered. Note that the CTE of Graphene is negative, this means that the material expands upon cooling down, which is in sharp contrast with the behaviour of conventional materials.

1.4 Modus Operandi

This section describes the different work packages that make up the core of this thesis. These are shortly discussed here, and the materials used in this thesis are

selected. The choice of these materials is of crucial importance, and may very well determine the best possible achievable result.

The two first sections treat these materials selection issues, and how these materials are processed in order to optimize the result. The third section discusses the Graphene growth step, which, due to the harsh conditions it applies on the template, has a decisive effect on the result. Finally, the characterisation of each step of the process is reviewed. Each of the four work packages discussed in this section are further explored in a chapter of this thesis.

1.4.1 Substrate selection and preparation

The substrate material is of paramount importance for the crystalline quality of the deposited catalyst layer. Two materials compete for this application, they are Al_2O_3 (commonly known as Sapphire) and MgO. Since Al_2O_3 is commonly available at *imec*, and the state-of-the-art in literature is favourable to using it, Sapphire will be used as substrate material. Additionally, it is available in monocrystalline wafers of large sizes[3], and the (0001) plane of the α phase of Sapphire can be used as a template for the (111) plane of an FCC metal.

Before the metallic catalyst can be deposited onto this substrate, the latter needs to be processed. Many different interesting procedures are advocated in literature, and their respective effect needs to be analyzed in order to determine the optimal substrate processing.

Chapter 3 gives an account of the results concerning the preparation of the Sapphire substrate.

1.4.2 Catalyst selection and deposition

The choice of the catalyst is the most important one, it will determine every other step of the process. Figure 1.4 gives a non-exhaustive list of metals that can be used as Graphene growth catalysts. At first sight, all these metals look suitable for Graphene growth, and most are. In order to make a wise choice, the properties of some commonly used metals is given in Table 1.2. The specific crystalline plane mentioned for each material is the one considered most adequate for growing Graphene, because of its geometrical similarities with the graphene crystal (i.e. lattice constant and rotational symmetry of 120°).

26 Fe	27 Co	28 Ni	29 Cu
44 Ru	45 Rh	46 Pd	47 Ag
76 Os	77 Ir	78 Pt	79 Au

Figure 1.4: Common metals used for catalysing the dissociation of a Graphene-CVD precursor.

[3] Note that, unfortunately, the price of such a wafer increases exponentially with its size.

Table 1.2: Comparison of the important properties of potential catalysts.

Material	C Solubility @ $1273K$ $[at\%]$	Melting Point $[°C]$	Lattice Parameter $[nm]$	RT CTE $[K^{-1}]$
$Cu\,(111)$	7.4 at ppm	1083	0.221	$16.5 * 10^{-6}$
$Ni\,(111)$	0.58	1453	0.216	$13.4 * 10^{-6}$
$Pt\,(111)$	1.16	1770	0.277	$8.8 * 10^{-6}$
$Co\,(0001)$	10.3 at ppm	1495	~0.27	$13 * 10^{-6}$
$Pd\,(111)$	>4.52	1555	0.277	$11.8 * 10^{-6}$

The first property displayed in this table is also the most important one. The C solubility of the catalyst strongly influences the possibility of controlling the amount of layers. Three of the five potential materials can now be eliminated, being: Ni, Pt, and Pd. To determine whether Cu or Co will make the cut, the possiblilities for grain growth (which is necessary if an epitaxial template is the target) are studied.

Cu has a much higher atomic mobility, and a lower melting point. It therefore undergoes giant grain growth much more easily than Co. This motivates the choice for Cu (111) as the catalytic material. Additionally, Co is not a FCC but HCP metal, and will therefore not show the (111) crystalline plane, but the (0001), when deposited on Sapphire(0001) [17]. The symmetry of a HCP(0001) plane is in theory also suitable for Graphene. Still, the grain growth potential of Cu makes it the most attractive catalytic material. The additionnal properties in the table are given for informative purposes. The reader should notice that the CTE of all these metals is positive. It does not vary significantly, and is not considered in the choice of the catalyst material.

The catalyst now has to be deposited onto a substrate. The most promising deposition technique is sputtering. It allows to accurately and quickly deposit a layer of the desired thickness onto the substrate. Note that, due to the nature of sputtering, the as-deposited layer consists of many small Cu domains separated by grain boundariess. This means that it needs to undergo a high-temperature treatment to reach its final structure.

Chapter 4 gives an account of the results concerning the deposition of the Cu catalytic layer.

1.4.3 Graphene growth

Finally, the template needs to undergo a Graphene growth procedure. In this work, the focus does not lie on the quality of this Graphene crystal, this is outside the scope of this thesis. Instead, the behaviour of the sputtered Cu layers under the high Graphene growth temperatures (often in excess of $1000°C$) is meticulously analyzed. The purpose here is to produce a perfectly epitaxial Cu/Al_2O_3 stack after the Graphene growth. Chapter 5 gives an account of the results concerning the effects of the Graphene growth step onto the template.

1.4.4 Characterization

Maybe the most important aspect of the work conducted in this thesis is the Characterization work package. This consists of applying all the available measurement techniques in order to accurately determine the effect of all the experiments that are conducted.

Appendix A describes, among other topics, the different characterization methods used in this thesis. Note that this package cannot really be considered on its own. The result of each process step has to be characterized in detail, and so this work package is involved in the discussion of every chapter of this thesis.

1.4.5 Starting point

In the next chapter of this thesis, a detailed analysis of the available literature on the subject of Cu epitaxy will be given. From this analysis, the work of Miller et al. [1] will be chosen to act as the basis of the experimental work conducted in this thesis. The authors not only report an encouraging result, they give a very detailed account of the procedure to reach it.

Chapter 2

Literature Review

Since the discovery of Graphene in 2004 [14], the interest in this material has seen a steady increase. This is due to the remarkable properties discussed by Geim, Novoselov et al. [14], and calculated by several others [2]. If Graphene is to be used on an industrial scale, a production method is required that offers a high degree of reproducibility, is relatively cheap, offers a high throughput, and allows the synthesis of high quality Graphene. Chemical Vapor Deposition (CVD) is thought to fulfill these requirements, and several groups have concentrated their efforts on the growth of CVD of Graphene on Ni[18], Ir[19], Pt[20, 21], Ru[22], Cu[23], Pd[24], Ge[25].

The use of Cu as a template is particularly interesting for a number of reasons. One of its crystalline planes, $Cu(111)$, has the same hexagonal crystalline structure as Graphene, and an interestingly small lattice mismatch. Furthermore, Cu is a Graphene growth catalyst with an exceptionally low solubility for C [26]. On other metals, e.g. Ni, where the C solubility is much higher, outwards diffusion of C during the cooldown causes an increase of the number of Graphene layers grown. Of all templates yet investigated, $Cu(111)$ could pave the way towards industrial scale production of monolayer Graphene. The Cu layer itself needs to be of high crystalline quality [23], which imposes strong constraints on the production and processing of the substrate. Ideally, a monocrystalline layer of $Cu(111)$ paves the way towards a high quality Graphene layer.

An interesting substrate for deposition of this $Cu(111)$ layer is $\alpha - Al_2O_3(0001)(c - plane$ Sapphire). Its low lattice mismatch (8.6%) [27] allows epitaxial growth. The surface properties can be manipulated to enhance the crystallinity of deposited Cu layers. Furthermore, monocrystalline $\alpha - Al_2O_3(0001)$ wafers can be bought at low cost or in sizes up to 15 inch [28].

In this literature study, a bottom up approach is followed. First the requirements for the Sapphire substrate are discussed, and the means to reach them. Second, the various procedures for depositing $Cu(111)$ are considered, as well as the properties of the desired result. Finally, the effect on Cu of growing Graphene (which is equivalent to annealing the Cu layer) are discussed.

2.1 Epitaxial Cu Deposition

Depositing atomically flat monocrystalline $Cu(111)$ on C-plane Sapphire is not an easy task. However, a moderate quality of small-grained $Cu(111)$ with changing in-plane orientations has been deposited, and could be subsequently annealed to cm sized grains (with pronounced grain boundaries) [1]. The grain size, layer thickness, possible contamination, and the ratio of the in-plane orientations of the Cu-grains need to be accurately controlled, and depend on a large amount of parameters. A proper $Cu(111)$ layer can be deposited either by Molecular Beam Epitaxy (MBE) [29], evaporation [4] or, if a higher deposition speed or thick layers are needed, sputtering[1, 30, 31].

If a reusable template is needed, the latter technique needs to be employed. The exact meaning of the word reusable depends on the way in which the Graphene is transferred to its final substrate and the Graphene growth parameters (Cu has a low melting point, close to typical process temperatures). One can dissolve the Cu layer on the sapphire substrate [32], thereby liberating the Graphene into the Cu etching solution. In that case the epitaxial $Cu(111)$ layer is lost, and has to be re-deposited on the sapphire substrate. Another method is to "peel" the Graphene off of the Cu template, e.g. using polydimethylsiloxane (PDMS)[33], where the Cu layer is in fact preserved and can be reused after little processing. To facilitate peeling, a so-called "bubbling transfer" can be used, where Hydrogen bubbles detach Graphene from the substrate. This method preserves the metallic substrate, but can damage the Graphene [34]. A third method is to use the Sapphire substrate to deposit a thick layer of $Cu(111)$ which is then peeled off[27]. This creates a mould of the Sapphire surface, and can be used to make a high quality (yet not perfect) Cu films. They need to be very thick however, for mechanical strength, and are discarded after one graphene growth step.

Two types of constraints have to be respected in order to deposit the ideal $Cu(111)$ substrate. On the one hand the properties of the Sapphire substrate are of the utmost importance, and on the other hand several parameters of the sputtering step can be tuned.

2.1.1 The Cu on Sapphire system

When the specific example of epitaxial $Cu(111)$ sputtering onto $\alpha - Al_2O_3(0001)$ substrates is observed, one must first of all consider the different in-plane orientations these surfaces can adopt with respect to each other. In a second subsection, different interesting sets of sputtering parameters are discussed.

Orientation Relationships

The respective symmetries of the $Cu(111)$ and $\alpha - Al_2O_3(0001)$ surfaces allow for two groups of thermodynamically equivalent relative orientations of these surfaces. These two groups are called Orientation Relationships (OR) and have been described in detail. The definitions hereafter are taken from [1, 4, 29]:

$$\begin{aligned} OR-I &\equiv (111)_{Cu} \parallel (0001)_{\alpha} \wedge \left[\bar{1}10\right]_{Cu} \parallel \left[10\bar{1}0\right]_{\alpha} \\ OR-II &\equiv (111)_{Cu} \parallel (0001)_{\alpha} \wedge \left[\bar{1}10\right]_{Cu} \parallel \left[2\bar{1}\bar{1}0\right]_{\alpha} \end{aligned} \tag{2.1}$$

A good graphical representation of these two ORs can be found in Figure 2.1.

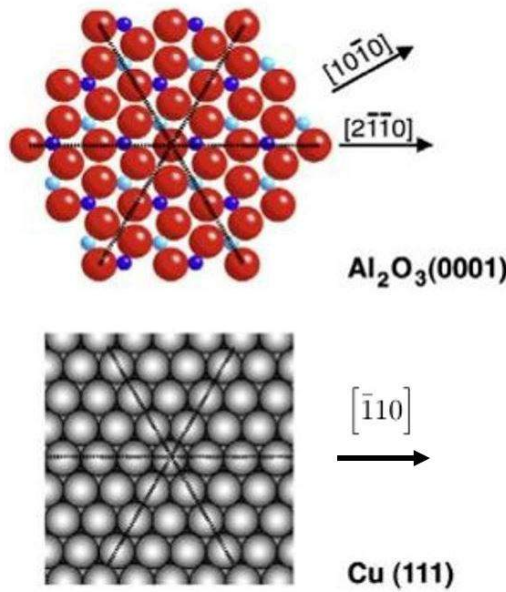

Figure 2.1: Graphical representation of the Orientation Relationships of $Cu\,(111)$ onto $\alpha - Al_2O_3\,(0001)$[4].

In the top part of Figure 2.1, the (0001) Sapphire surface is shown, where the red dots represent Oxygen atoms, and the light and dark blue dots the two respective layers of Aluminum atoms. The arrows, with corresponding crystalline coordinates, indicate the two possible directions along which the $\left[\bar{1}10\right]$-direction of the $Cu\,(111)$ surface can be oriented. This $Cu\,(111)$-surface is shown in the bottom part of the figure. The first atomic layer has sixfold symmetry, but when one looks at the second layer (it can be seen in the interstices between the atoms), the threefold symmetry of $Cu\,(111)$ appears clearly.

According to the definitions given in Eqs 2.1, the ORs have a 60° symmetry, so a Cu grain onto sapphire can be rotated over 60°, and yield a system in the same

energetic state. The Cu grain itself, however, has a 120° symmetry, which means that what is called $OR-I$ or $OR-II$ in literature in fact consists of two different grains (called twins, this effect is called twinning). Therefore, a complete definition for the possible ORs will be given here which takes the symmetry of the Cu grains into account as well:

$$\begin{aligned} OR-Ia \equiv (111)_{Cu} \parallel (0001)_{\alpha} \quad & \wedge \quad \left[\bar{1}10\right]_{Cu} \parallel \left[10\bar{1}0\right]_{\alpha} \\ & \vee \quad \left[\bar{1}10\right]_{Cu} \parallel \left[0\bar{1}10\right]_{\alpha} \\ & \vee \quad \left[\bar{1}10\right]_{Cu} \parallel \left[\bar{1}100\right]_{\alpha} \end{aligned} \tag{2.2}$$

$$\begin{aligned} OR-Ib \equiv (111)_{Cu} \parallel (0001)_{\alpha} \quad & \wedge \quad \left[\bar{1}10\right]_{Cu} \parallel \left[1\bar{1}00\right]_{\alpha} \\ & \vee \quad \left[\bar{1}10\right]_{Cu} \parallel \left[\bar{1}010\right]_{\alpha} \\ & \vee \quad \left[\bar{1}10\right]_{Cu} \parallel \left[01\bar{1}0\right]_{\alpha} \end{aligned} \tag{2.3}$$

$$\begin{aligned} OR-IIa \equiv (111)_{Cu} \parallel (0001)_{\alpha} \quad & \wedge \quad \left[\bar{1}10\right]_{Cu} \parallel \left[2\bar{1}\bar{1}0\right]_{\alpha} \\ & \vee \quad \left[\bar{1}10\right]_{Cu} \parallel \left[\bar{1}\bar{1}20\right]_{\alpha} \\ & \vee \quad \left[\bar{1}10\right]_{Cu} \parallel \left[\bar{1}2\bar{1}0\right]_{\alpha} \end{aligned} \tag{2.4}$$

$$\begin{aligned} OR-IIb \equiv (111)_{Cu} \parallel (0001)_{\alpha} \quad & \wedge \quad \left[\bar{1}10\right]_{Cu} \parallel \left[1\bar{2}10\right]_{\alpha} \\ & \vee \quad \left[\bar{1}10\right]_{Cu} \parallel \left[\bar{2}110\right]_{\alpha} \\ & \vee \quad \left[\bar{1}10\right]_{Cu} \parallel \left[11\bar{2}0\right]_{\alpha} \end{aligned} \tag{2.5}$$

It is obvious that when the two different ORs are present on a substrate, the template cannot be homogeneous and consists of grains with the different orientations. It is therefore important that a process would result in a single OR. Keep in mind that the Graphene deposition step is, for the Cu equivalent to an anneal. The quality of the layer is influenced by this procedure, and by the (mix of) OR(s) present on the surface before deposition.

Whether or how the sputtering parameters and the properties of the substrate influence which OR is deposited is not yet entirely clear. Some studies claim that the substrate preparation significantly influences the OR [29, 35, 36], and similarly for the substrate temperature [37], the deposition rate [37], or various other parameters [4]. On the other hand, Curiotto et al. [4] claim the chemical termination of the Sapphire substrate does not influence the orientation.

Parametric Targets

A perfectly monocrystalline layer of $Cu(111)$ can be deposited in two ways. Either the as-deposited crystalline structure is the desired one, or a subsequent series of steps (e.g. annealing) is needed to induce grain growth and recrystallization.

In the first case, Lee et al. [38] claim that very low deposition rates (in the order of 0.1 nm/s) could lead to monocrystalline as-deposited $Cu(111)$, despite unfavorable deposition conditions (working pressure below $0.1Pa$, sputtering power of $40W$, substrate temperature between room temperature and $200°C$). On the other hand Miller et al. [1] claim that a very specific mix of OR-I and OR-II can lead, after high temperature annealing, to grain growth yielding crystals with sizes in the order of 1 cm. Table 2.1 gives an overview of the parameters used by the authors.

Table 2.1: Parameters for giant grain growth according to Miller et al. [1].

Pre-deposition Anneal	
Temperature	1100°C
Duration	24 hrs
Ambient	O_2
Sputtering	
Temperature	80°C
TSD	8 cm
Power	100 W
Pressure	0.17 Pa
Duration	500 sec

2.1.2 Influence of the substrate

The quality of the $\alpha - Al_2O_3(0001)$ surface is paramount to the epitaxial deposition of $Cu(111)$. Both the topology of the surface and its chemical properties strongly influence the properties of the deposited layer.

Roughness

The roughness of the surface is strongly influenced by the cleaning and annealing steps performed prior to the deposition of Cu. A high temperature step causes reflow of the structure, and for most topologies leaves behind a relatively flat surface, with huge terraces bound by steps approximately 0.2 nm high [39]. The shape and width of these terraces is strongly dependent on the original miscut angle of the Sapphire surface and the annealing temperature [39]. AFM pictures allow to investigate the roughness of a substrate, and subsequently assert its usability in further processing.

Since the Sapphire substrate serves as a template for the crystallinity of the deposited Cu layer, any steps or inhomogeneities must be avoided. This could jeopardize the transfer of the crystalline symmetry of the Sapphire to the metal upon it, thereby promoting polycrystalline growth instead of the (in the end) desired monocrystalline layer.

Termination

The C-plane of Sapphire can have three different terminations: stoichiometric Aluminum terminated (1 layer of Al), Oxygen rich (1 layer of O) and Aluminum rich (2 layers of Al) [40]. Of these surface terminations, theory predicts the single-layer Al-termination to be the most stable even under high Oxygen partial pressures and at high temperatures [6, 40, 41, 42]. However, it has been speculated that the Oxygen-termination of Sapphire would be most suited for the epitaxial deposition of

$Cu(111)$: Hashibon et al. [43] claim that Cu atoms have a predilection for threefold Oxygen sites.

Furthermore, the surface is quickly hydroxylated, upon exposure to as little as $1 * 10^2$ Pa partial pressure of H_2O [41, 44, 45]. These Hydroxyl groups may undergo a surface chemical reaction with the metal adatoms to be deposited. This influences the wetting behaviour of the deposited layers, as well as their crystalline quality [44, 45, 46]. Whether the effect of Hydrogen on the Sapphire surface is beneficial or deleterious is not fully obvious: Oh et al. [36] claim an Oxygen terminated surface, without Hydrogen, would be best suited for depositing a metal. However, epitaxial growth onto hydroxyl-Aluminum terminated surfaces also seems possible [36], though it would be limited to less than a monolayer. Additionally, Curiotto et al. [4] claim the surface termination does not influence the resulting OR.

2.1.3 Processing the substrate

In this section, the effect of different surface treatments is reviewed. Note that, in most cases, a pristine Sapphire wafer is assumed. Wherever this does not apply, preceding process steps are documented.

Cleaning

The necessity for cleaning a substrate before any deposition step is evident. Should this not happen, the surface could be covered in mostly unknown contaminants, including metals, adsorbed water, polymers from plastic containers, dust, and biological deposits (hair, skin). What is subject to discussion, however, is which cleaning method to employ, and the influence of different methods on the chemical termination of the Sapphire afterwards.

Scheu et al. [35] provide a comparison between different cleaning procedures utilizing solvents. The authors conclude that, in case of a wet chemical etch, the surface is most likely to be oxygenated or hydroxylated, with a strong preference for the latter, as it is the most stable when the surface has come in contact with water [41]. Note that, even though solvents do not contain water, the chemicals the authors use all have plenty of hydroxyl groups.

Acid-based etchants, like H_2SO_4, H_3PO_4 and the $3:1$ mixture of the respective chemicals are very interesting. These can be heated up to much higher temperatures (not flamable), and are less selective (thus remove a broader range of contaminants). This last advantage can also be an inconvenience, as Phosphoric Acid and the $3:1$ solution have been reported to etch Sapphire, preferentially at defect sites [47]. A pure H_2SO_4 etch, at $300°C$ for 30 min, has been shown to yield a smooth and pit-free surface [47]. For longer etching times, the risk of material redeposition on the surface becomes higher.

Grinding/CMP

Chemical-Mechanical Polishing and other mechanical steps are common in most procedures involving deposition onto a substrate. These steps are well understood, and necessitate the use of corrosive particles, which are not welcome in a regular cleanroom environment[1]. It is, therefore, a step that is typically performed by the retailer of the substrate. This is especially true for small wafers (Sapphire wafers of larger sizes are available as well, but become more expensive).

Ion Milling

An Ar^+ ion bombardment, with energies typically ranging between 200 and 1000 eV can be used to remove several types of contaminants from a surface. After detecting metallic *Cu*-*Al* bonds at the interface of deposited *Cu* and Sapphire, Scheu et al. [35] conclude that a 1000 eV Argon sputtering step can deplete a surface from its Hydroxyl or Oxygen termination and transform it into an *Al*-terminated surface.

Besides depleting a substrate from its contaminants, an ion bombardment step also removes or damages a few layers of the substrate itself (this is the principle behind sputtering). Chemical bonds inside are broken, and the substrate may locally become amorphous. The higher the energy of incident ions, the deeper they penetrate into the substrate, the thicker the damaged layer.

Annealing

Annealing is, just like cleaning, a common step in most production procedures. It influences both the surface termination of the Sapphire, and the roughness of the wafer. For the first parameter the ambient and the pressure of the anneal are most important. For the roughness of the wafer, the temperature has the highest impact.

The environment in which the Sapphire wafer is annealed strongly influences the chemical termination of the surface. One can distinguish roughly five ambients in which it would be interesting to anneal a sapphire wafer: Oxygen, Hydrogen, Nitrogen, Argon and vacuum. Scheu et al. [35] found that an anneal performed in vacuum leaves the surface Al-terminated, whereas an anneal in Oxygen atmosphere (temporarily) leaves the surface Oxygen terminated. Argon and Nitrogen do not chemically react with Sapphire, and therefore the effect on the termination is not significantly different from that of a vacuum anneal. Finally, annealing Sapphire in a reducing Hydrogen atmosphere has not shown to substantially influence its morphology or termination, as compared to an inert atmosphere. Curiotto et al. [48] report surface compositions and morphologies entirely similar to the case of vacuum, thus only depending on the temperature and, to a lesser extent, the anneal time.

[1] The particles must be contained in a closed off environment to avoid contamination. In an industrial environment this is standard available, but for purely experimental work it sets additional constraints that can be avoided.

Annealing a Sapphire wafer at high temperatures (typically well above 1000 $°C$) causes its surface to reflow into a lower energy structure. This may not necessarily be the flattest one. Steps, which are bound to be present, start moving, and, in the case of surfaces with a high nominal miscut angle, undergo step bunching or facetting due to the attractive interaction between steps [39, 49, 50]. Note the difference between step bunching and step facetting; step bunching corresponds to parallel steps superimposing, thus yielding a higher step, while step facetting corresponds to changes in step direction. The higher this miscut angle, the slower the step bunching disappears [39, 49]. Furthermore, Cuccuredu et al. [39] claim that an increase in the annealing temperature accelerates step bunching and thus increase the average step height. Step bunching is thought to be temporary and should decrease for longer anneal times [39, 49, 51]. It is possible, according to Yoshimoto et al. [52], to obtain an ultrasmooth surface with atomic steps and wide terraces, given the initial wafer has a low miscut angle and the annealing parameters are well tuned (1000 $°C$ for 1h).

In case of a substrate with a very rough surface, e.g. damaged due to a very aggressive chemical etch, a high temperature anneal may prove useful nevertheless. Indeed, Dwikusuma et al. [47] claim that damaged wafers (with defects in the range of at least $1\mu m$) can be annealed to a terrace-and-step structure by annealing for 1h in air at 1400 $°C$. According to the same authors still, a Hydrogen anneal at 1100$°C$ can remove most chemical contaminants, but does not smooth out surface scratches.

Oxygen Plasma Cleaning

Oxygen plasma contains highly energetic Oxygen ions at a high temperature, it could thus be assumed that exposing a Sapphire substrate to such a treatment would result in an Oxygen terminated surface. A clean dehydroxylated surface can be given an Oxygen termination by exposing it to Oxygen plasma at 750 $°C$ according to Scheu et al. and Oh et al. [35, 36].

These plasma-treated samples show an inhomogeneous deposited Cu layer. This suggests that, even though the Oxygen plasma is thought to leave the surface O-terminated, there is more going on. Indeed, Oh et al. [36] further claim that the Cu-Al_2O_3 surface is not uniform, but instead consists of atomically abrupt areas and regions with unfavorable crystalline quality (amorphous or with a different structure).

2.1.4 Sputtering

The deposition system undoubtedly strongly influences the quality of the sputtered material. The parameters which are thought to be most influencial are the pressure inside the sputtering chamber, the temperature at which the sample is held during deposition, the distance between the Cu target and the Sapphire substrate, and the sputtering power. The deposition rate is important as well. However, it cannot be

tuned on its own, as it is influenced by the four previous parameters. In the following sections, these five parameters are discussed.

Sputtering Pressure

The highly energetic plasma used inside sputtering tools can only be generated in a very specific pressure window. On the one hand, a sufficiently low pressure is necessary, else the deposition rate drops due to many of the sputtered particles being scattered away [53]. On the other hand, if the pressure is too low, there are not enough ions in the plasma, and it fails to ignite. Within this window (typically between 1 and $10 * 10^{-3} mbar$), the exact pressure has an effect on the energy and the amount of sputtering ions reaching the target, and henceforth the depth of penetration and the energy transferred to the sputtered particles. This influences their size and energy.

As sputtered species collide with neutral and charged particles, they lose some of their acquired energy, in a process known as thermalization. A higher pressure (as well as a longer target-to-substrate distance) therefore decreases the mobility of the deposited adatoms, and impedes recrystallization and growth [54]. According to Chawla et al. [55], on the other hand, since a higher sputtering pressure increases the number of collisions involving sputtered species, they are more likely to agglomerate and form bigger as-deposited grains. A side effect is that the deposited film can be porous, since these grains may not merge into a continous film.

Temperature

A heatable substrate holder allows to modulate the substrate temperature during a deposition step. This temperature influences the mobility of sputtered atoms, which is translated in a changed crystalline structure of the deposited layer [5]. It is customary to express the temperature of the substrate with respect to the melting temperature of the sputtered material: T/T_m. Three mechanisms are suggested to influence the structure of the sputtered layer: recrystallization and grain growth, shadowing, and adatom diffusion [56].

At low temperatures, shadowing can cause open grain boundaries, as the two other mechanisms are virtually frozen. As the temperature increases, adatom diffusion smoothes out the sputtered layer and grain growth may happen. This process is in fact nothing different than what is seen when a material is annealed in vacuum. When the temperature is increased even further, porous structures can be formed due to the interplay of shadowing and agglomeration of grains.

This appears to be one of the main parameters to control when depositing a thin Cu layer. Miller et al. [1] found that for temperatures ranging from room temperature to 600 $°C$ the crystalline quality of the Cu could be tuned over a wide range. Figure 2.2 shows the combined influence of the temperature and the Ar pressure, and is considered generally applicable to sputtering of metals.

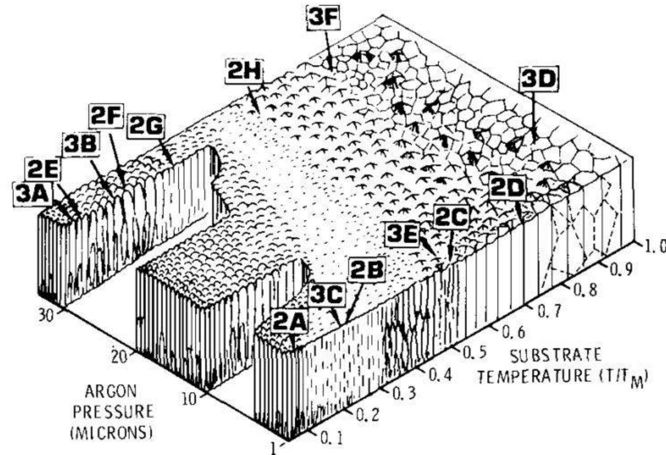

Figure 2.2: Influence of the *Ar* pressure and substrate temperature (normalized with respect to the melting point of the sputtered species in its bulk form) on the structure of a sputtered metallic layer. From Thornton et al. [5].

Figure 2.2 shows the surface and bulk structure (by picturing the grain boundaries) in the pressure-temperature parametric plane. A general trend that can be seen is that, for increasing pressure, the same crystalline structure can be obtained at a higher substrate temperature. It also shows that, at higher temperatures, generally larger grains with fewer defects are deposited. This is due to the fact that the metallic layer is basically being annealed *in situ* during the deposition.

Target-to-substrate Distance

The distance between the sputter-target and the substrate to be coated influences the amount of collisions the sputtered particles undergo before reaching the substrate. Every such collision decreases the energy of a particle and scatter it in a slightly different direction [53]. This has an effect on the crystallinity of the deposited layer and on the relative size of the different grains. Furthermore, the further the substrate is away from the target, the less sputtered particles reach it, effectively decreasing the rate at which the thickness of the deposited layer increases. This effect is enhanced by increasing the Argon pressure. For a longer target-to-substrate distance (TSD), the sputtered species will have lost more energy, which is not only equivalent to a higher sputtering pressure, but also to a lower substrate temperature.

Sputtering Power

The sputtering power influences the amount and energy of the Argon ions incident on the sputtering target, and, as a result, the amount and energy of the sputtered particles themselves [53]. As a rule of thumb, the amount of sputtered particles can be related to the current and their energy to the sputtering voltage. Increasing

the sputtering power thus increases the deposition rate, but also causes a higher scattering rate. More neutral species are present between the target and the substrate, and, therefore, a higher portion of the sputtered particles are scattered away from the substrate. This increases, in a similar fashion to the effect of pressure, the probability that sputtered species agglomerate before reaching the surface. A higher sputtering power thus increases the as-deposited grain size and the surface roughness [57]. A higher energy of the sputtered species also causes a higher surface mobility of the deposited Cu. This contributes to a rough structure, due to recrystallization (similarly to a higher temperature).

Sputtering Rate

The sputtering rate is affected by three of the the four previously cited parameters. A higher pressure scatters more of the sputtered species, thereby decreasing not only their energy, but also the amount of particles reaching the substrate. An increasing TSD decreases the sputtering rate; sputtered species are propelled at a random angle into the chamber. When the substrate is further away from the target, it occupies a smaller solid angle, and hence it collects a smaller portion of the sputtered species. Additionally, the TSD has the same effect as the sputtering pressure, a longer distance to cross means more scattering, so lower species energy and a lower portion of them reaching the substrate. Finally a higher sputtering power increases the amount of Cu sputtered into the chamber, but also increases the portion of species scattered away.

As can be seen, the sputtering rate is not an extrinsic parameter of the deposition step. It cannot be tuned directly, but depends on the interplay of the other parameters. If necessary, it can be measured by using a thin crystal vibrating at its natural frequency. By measuring the change in this natural frequency, the thickness of the layer sputtered onto this crystal can be calculated.

2.1.5 Challenges

From the previous section, it can be concluded that both the parameters of the deposition itself and the quality of the used substrate are important for producing the desired quality of Cu. When this desired quality is reached, the Cu layer still has to endure (multiple) Graphene growth cycle(s). This acts as an annealing step.

As was mentioned in Section 2.1.1, the procedure developped by Miller et al. [1] is used as a starting point for the experimental work conducted in this thesis. Though their result is not optimal (the authors have both OR-Ia and OR-Ib after anneal), the procedure can be optimized to reach a better result.

2.2 Graphene Growth

In order to grow a Graphene flake onto a surface, a Carbon-containing species (the precursor) needs to undergo a chemical dissociation reaction (catalyzed by the substrate) under specific temperature, pressure and flow rate conditions. The parameters of this chemical reaction are of the utmost importance, as well as the properties of the substrate onto which the Graphene is to be grown. A general form of the dissociation reaction is again given below:

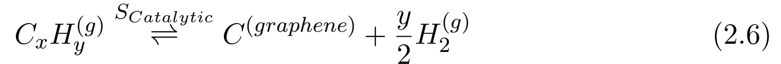

$$C_xH_y^{(g)} \overset{S_{Catalytic}}{\rightleftharpoons} C^{(graphene)} + \frac{y}{2}H_2^{(g)} \tag{2.6}$$

2.2.1 Chemical Vapor Deposition (CVD)

In CVD, a precursor molecule is made to flow over a surface, such that it chemically dissociates and produces a Graphene layer to cover a given substrate. In the case of the CVD of Graphene, the precursor is a C containing species, that dissociates under high temperature conditions. The main process parameters are the type of precursor (and other gasses in the chamber), the temperature and the growth time. One can also discuss (partial) pressures of the various chemicals involved, as well as their flow rates. This dissertation does not focus on the latter.

The choice of the precursor has a direct effect on the chemistry employed inside the CVD chamber. Not only does it provide the C atoms for the Graphene, every chemical group attached to the hydrocarbon chain can potentially interact with the substrate and/or the Graphene flake. Two options are presented for the type of precursor used in the CVD system: liquid or gaseous. Note that there is a third option, solid precursors [58]. This is not a CVD technique, however, and is not discussed.

Liquid precursors (alcohols: Methanol, Ethanol and Propanol) have been used to grow Graphene. Exposure to alcohol vapors at a temperature of 850°C for 5 min shows monolayer graphene growth onto a large portion of the Cu surface [59]. The precursor does not seem to influence the result drastically, as opposed to the temperature. The presence of O in the precursor does not seem to dope the Graphene. Additionally, the authors claim that the Cu surface has a low Oxygen affinity, and base this claim on the account of Sun et al. who claim to have achieved graphene growth using sugars [58]. This sounds counterintuitive, Cu is very prone to oxidize even under ambient conditions.

Gaseous precursors are more common than liquid precursors. Possible gaseous precursors used for growing Graphene can be: Methane[3, 26, 60], Ethylene [23], and Acetylene [61].

The concentration of Hydrogen gas in the CVD chamber is of high importance for the kinetics of Graphene growth. Its role is multiple, Ago et al. [3] describe the effect of Hydrogen on Methane-based graphene growth. First of all, H_2 etches the

surface Cu oxide, thereby increasing the catalytic activity of the Cu surface, and the dissociation of Methane. On the other hand, it influences the kinetics of the graphene growth chemical reaction (Li et al. [60] give a simple description of the process):

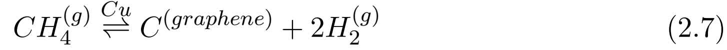

$$CH_4^{(g)} \overset{Cu}{\rightleftharpoons} C^{(graphene)} + 2H_2^{(g)} \tag{2.7}$$

As can be seen, the chemical equilibrium shifts to the left hand side of the equation when the H_2 concentration increases. It is even thought that a high concentration of Hydrogen gas in the reaction chamber could actually etch existing Graphene [3, 62], thereby dividing grains into smaller ones. It appears that the concentration of H_2 must be neither too high, nor too low. A similar reasoning can be applied for the Methane supply: too high and the nucleation density increases; too low and the supply of C atoms decreases. In both cases, the domain size significantly decreases.

Graphene growth typically occurs between 900 and 1100 $°C$. The lower boundary for Graphene growth seems to be in the order of 850 $°C$ [63], where highly defective Graphene is produced. The upper boundary is determined by the melting point of the template materials, in this case, Cu, which has a melting point of 1083$°C$. Between these boundaries, the domain size can be increased with increasing temperature (due to decreased nucleation of grains) [60]. An increase in temperature also decreases the amount of defects, and suppresses the formation of multilayer Graphene [30]. Large area Graphene flakes have been grown at temperatures up to 1080 $°C$ [3].

Pre-growth anneal

Graphene is typically grown at high temperatures (above 900$°C$), and before the growth procedure is started by introducing the C-holding precursor, the temperature of the reactor needs to be increased and stabilized. This corresponds to an annealing step, and makes the Cu grain boundaries move. This step is actually of real importance, the Cu that is formed is used for growth right after its formation. It has already been shown that a high temperature anneal smoothes out the surface of an epitaxial Cu film [31]. This anneal could, given exactly the right quality of Cu as input, result in the growth of giant Cu grains most suited for potential large area Graphene growth [1].

2.2.2 Influence of the template

The role of the template in the CVD of Graphene is multiple. It first catalyzes the chemical dissociation of C containing precursors. The liberated C atoms then diffuse over the surface of the template, until they nucleate and start growing into a Graphene flake. The less nucleation points, the better the potential quality of the grown structure.

Chemical termination

The Cu metal of the template is responsible for the catalytic dissociation of the precursor. It is therefore necessary to remove the layer of native Cu oxides before any deposition steps. Typically, this can happen with a dilute acid treatment. However, according to Liu et al. [33], this makes the surface of Cu rough, which is undesirable as is shown in the next sections. Furthermore, they found that the purity of the Cu substrate influences the amount of Graphene layers, with a lower purity promoting the growth of bilayer and multilayer Graphene.

Crystallinity

Nucleation of Graphene growth is thought to happen at these loci of lower energy (at the grain boundaries and surface steps [30, 33, 64, 65], due to the higher chemical activation energy of these sites). Grain growth further happens by the arrival of additional C atoms at the edges of the growing flake. Orofeo et al. [66] further show that for a polycrystalline Cu substrate, the grain boundaries of the substrate can be related to the grain boundaries of the grown Graphene. They observe no grain boundaries in Graphene grown on (hetero-)epitaxial $Cu(111)$ and attribute this to the unified orientation of Graphene hexagons (even though different grains might have nucleated, their relative orientation allows them to merge into larger grains). Most sources indeed indicate that a monocrystalline $Cu(111)$ template would be optimal for large area Graphene growth [27, 64].

On the other hand, Rasool et al. [67] and Yu et al. [68] claim that it is possible to grow monocrystalline Graphene even onto polycrystalline templates. They observe large area monocrystalline growth on surfaces showing polycrystalline features. These polycrystalline surfaces display facets with a different crystalline orientation (from low index faces (100) to higher indices (311)). This once again illustrates the contradictions that are present in the literature on the topic of Graphene growth. Note that even in the cases where monocrystalline Graphene is reported growing over Cu grain boundaries, the growth rate seems to drop when the flake crosses these boundaries [69].

OR Mix

The specific OR present on the surface (given it is monocrystalline, after anneal) is in fact of no importance, since both present the same $Cu(111)$ surface. When at least two different ORs are present simultaneously, however, the deposited Cu has grain boundaries. The same objection as in the previous section can thus be raised here, the grain boundaries in the Cu template will increase nucleation of Graphene[30, 33]. This causes smaller Graphene flakes.

Another issue is the relative orientation of the nucleated Graphene flakes themselves. Graphene has a hexagonal symmetry, so when two Graphene flakes nucleate on the two different ORs (with a respective angle of 30° with respect to each other),

they have a different orientation. There is no possibility for these flakes to grow together after that without the formation of a grain boundary. Additionally, Li et al. [70] found that the actual growth rate of the Graphene flake is anisotropic (up to a factor 2). This complicates even more the growth of large Graphene domains on templates withouth homogeneous orientation.

Finally, the resulting crystalline quality of the Cu layer is also influenced by the initial OR mix. As is explained in Section 2.1.1, the different orientation relationships are thermodynamically different from each other. They may thus behave differently under a high temperature step. More specifically, the most stable OR should result, given the Sapphire substrate is of good quality [1].

Roughness

The $Cu(111)$ template should be atomically flat. It is generally accepted that steps in the surface are preferential sites for the nucleation of Graphene growth [33, 65, 69]. It is preferable, for monocrystalline growth, to suppress these nucleation sites as much as possible, and thus to improve the flatness of the template. While these surface steps are nucleation centers for the flake growth, a single step does not seem to impede the growth of Graphene [69]. Rasool et al. go even further [67], and claim that Graphene growth can happen undisturbed over larger defects on the Cu substrate, even those exposing other crystalline faces.

2.2.3 Challenges

The challenges in growing Graphene are numerous, but this is not the topic of this dissertation. The purpose here is to produce a monocrystalline Cu substrate, which is the first step towards the growth of monocrystalline Graphene. The main parameters were already discussed previously, it is of paramount importance that the quality of the as-deposited Cu layer be perfectly controllable. When the perfect OR mix is reached, the template can be annealed to form a crystal consisting solely of non-twinned OR-I. By improving upon this procedure, epitaxy of a single crystal should be possible.

2.3 Conclusion

In this short and in no way exhaustive review of the available literature on epitaxy of Cu and growth of Graphene, the different important parameters for the work conducted in this thesis were discussed. Two of the key aspects in Cu (111) epitaxy are the Sapphire surface preparation and properties, and the deposition parameters of the Cu sputtering setup.

On the one hand, the surface of the Sapphire wafer should be perfectly clean (one cannot hope to deposit a Cu layer of good quality if there are unwanted foreign

species on the Sapphire surface), atomically flat and have the right chemical termination.

On the other hand, the deposition parameters of the Cu sputtering setup need to be tuned accurately. It is not impossible that different sets of parameters exist at which the sputtered layer is of the desired quality. The sputtering setup itself might also have a non negligible influence on the quality of the Cu layer

Only if both these aspects are controlled, will it be possible to anneal the sputtered layer into an epitaxial Cu grain the size of the substrate wafer.

Chapter 3

Preparation of the Al_2O_3 substrate

The preparation and subsequent condition of the Sapphire substrate has a decisive effect on the crystalline properties of the $Cu\,(111)$ layer. This chapter is dedicated to the experimental findings on this aspect of Cu epitaxy. The importance of the crystallinity, chemical termination and surface topology of the Sapphire cannot be stressed enough.

The first section gives a brief overview of the properties of pristine Sapphire wafers. The next three sections detail the results of the procedures applied on the pristine Sapphire wafers *ex situ*. Sections 3.5 and 3.6 then discuss the results of the procedures applied on the Sapphire wafers *in situ*. Finally, in the concluding remarks, the importance of the different properties of the Sapphire wafers is stressed.

The measurement technique that is most used throughout this chapter is XPS. With XPS, it is possible to calculate the *relative* concentrations of different elements close to the surface of a material (within the first 10 nm, see Appendix A.5). Since the output is relative, a strong increase or decrease in surface contamination influences the *relative* amount of Aluminum and (Sapphire-) Oxygen at the surface. The *absolute* concentration, reflecting the Sapphire lattice termination, is derived from the individual elemental spectra whenever necessary.

3.1 Original state

Before processing, the Sapphire wafers are stored on the shelf for an undetermined amount of time. It is therefore important that the (surface) properties of this original state be analyzed, as well as the possible influence they could have on the results of further processing steps. The 2 *inch* Sapphire substrates are provided by Roditi (the webpage can be found in reference [71]), and are grown with the Czochralski process.

3.1.1 Crystallinity

According to the supplier, the Sapphire wafers are highly monocrystalline, with an atomic purity above 99.995%. They are optically perfect, including under microscope investigation. The crystalline orientation of the surface is the c-plane (0001), with a miscut angle below 0.3°.

A small flat piece is intentionally left out of the otherwise perfectly circular Sapphire wafers to indicate the crystalline in-plane orientation of the surface. This feature is referred to as the Primary Flat Location (PFL). The orientation of this flat is parallel to the a-axis $\left\langle 11\bar{2}0 \right\rangle$. Note that the triangular brackets here indicate that all $\left\langle 11\bar{2}0 \right\rangle$ directions are possible. In practice, this means that the primary flat location could be either at $\left(\bar{1}\bar{1}20\right)$ or $\left(11\bar{2}0\right)$, or any of the equivalent orientations.

This unknown in the exact orientation of the surface with respect to the PFL will have to be taken into account in the analysis of the crystallographic results (XRD).

3.1.2 Surface roughness

The pristine Sapphire substrates are very smooth (RMS roughness of 0.11 nm). AFM investigation shows that the surface of these substrates is almost atomically flat (see Figure 3.1). The surface shows vertical linear patterns that can be interpreted as a terrace-and-step structure with parallel steps and atomic step dimensions (below 0.25 nm).

Additional diagonal linear features can be seen on the AFM images of the original Sapphire substrates. These are larger, deeper, and further away from each other. The best explanation for these stripes is that they originate from the mechanical polishing of the substrates.

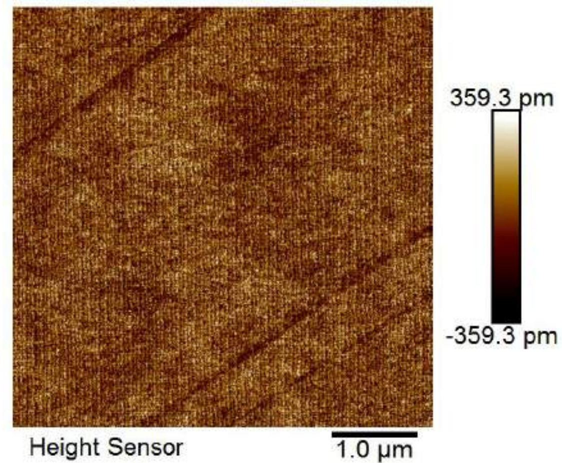

Figure 3.1: AFM image of the surface of pristine Sapphire wafers.

3.1.3 Surface termination

In Chapter 2 of this thesis, the literature review, the thermodynamic stability of the different possible chemical terminations of c-plane Sapphire is discussed. Of the three possibilities, the single Al termination appears to be the most stable in

vacuum, and would be hydroxilated when exposed to humidity. This is therefore the expected initial state of the Sapphire wafers.

To investigate this question, angle-resolved XPS studies are conducted on pristine Sapphire wafers (see Figure 3.2). Unsurprisingly, these measurements report significant C and F contamination of the surface of the wafers. This can likely be attributed to the Teflon containers in which the wafers are stored. The two main components of Teflon are C and F, hence the contamination. The relative concentrations of C and F signals increases with the exit angle, indicating that they originate from the surface. Additionally, surface C contamination is also characteristic for materials exposed to air.

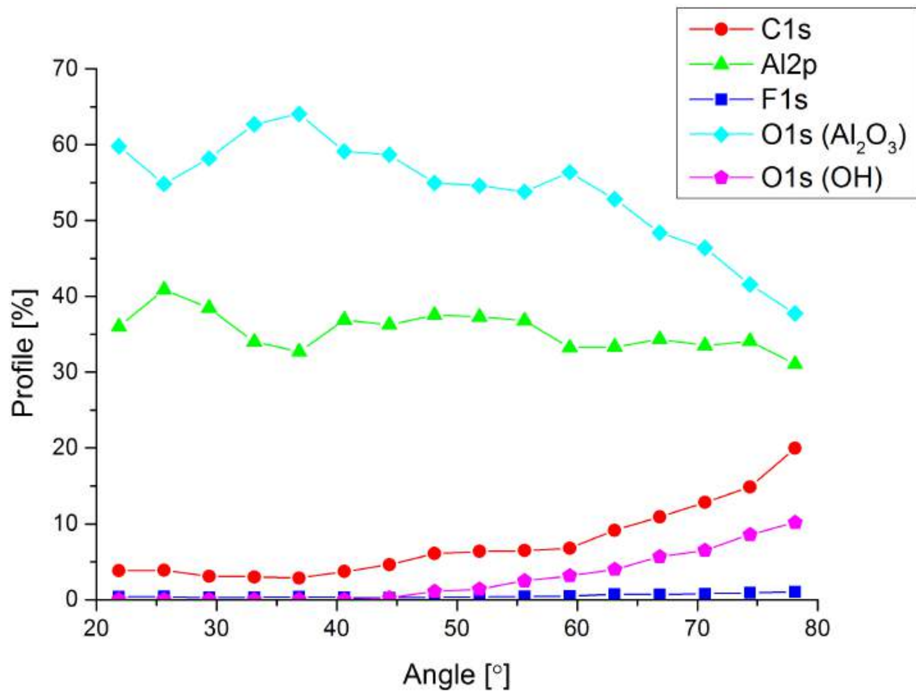

Figure 3.2: Angle-Resolved XPS measurement of the surface of pristine Sapphire wafers. The low exit angles stand for the bulk concentrations, while the higher exit angles represent the surface concentrations.

The Oxygen signals recorded in these measurements can be distinguished using the measured binding energy. On the one hand, a signal displaying a binding energy of $E_B = 531\ eV$ (typical for Sapphire Oxygen [44, 45]) decreases with the exit angle. This is due to the lower amount of electrons emitted at a higher exit angle. The other Oxygen signal, with a binding energy of $E_B = 532\ eV$ (typical for $C-O$ or $O-H$ bonds [44, 45, 72]) increases with increasing exit angle (relative to the Sapphire Oxygen signal). The two XPS spectra of Figure 3.3, taken at different exit

angles, show the relative increase of the OH signal. These results indicate an increase in the concentration of hydroxyl Oxygen on the surface, compared to the bulk.

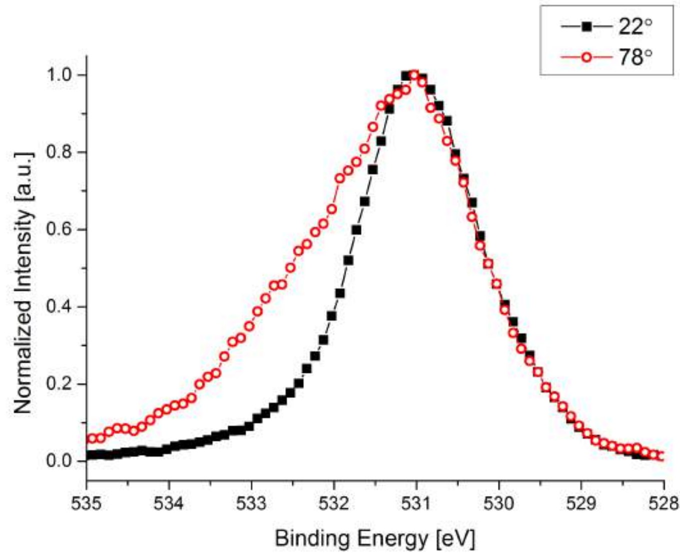

Figure 3.3: Normalized Angle-Resolved XPS spectra of the Oxygen signal for pristine Sapphire wafers. The 22° curve describes the bulk concentrations and the 78° describes the surface concentrations.

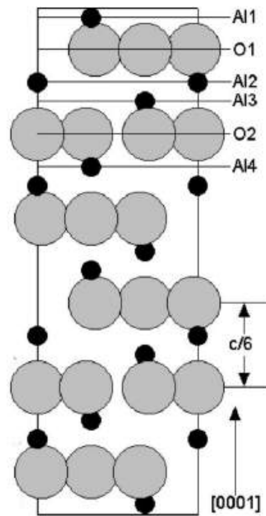

Figure 3.4: Vertical section of the Unit Cell of Sapphire[6].

Finally, the Al signal is analyzed. At low exit angles, the ratio of the Al to the (low binding energy) O signals is approximately 2/3, which is close to the stoichiometry of Sapphire. Additionally, the Al signal decreases much less with increasing exit angle than the O signal, indicating a relative increase in Al content of the surface. This could point towards an Al termination. One interesting detail is the ratio between Al and (low binding energy) O at large exit angles. It does not indicate a stoichiometric content anymore. As can be seen in Figure 3.4, the single Al termination is supposed to be stoichiometric. This difference can be explained by the limitations of XPS. Surface contamination may influence the calculated concentrations. Additionally, the composition accuracy is in the order of 20% relative. The repeatability over several measurements is much better (1%), and is what matters here.

One can conclude that the chemical termination of pristine Sapphire wafers is indeed the hydroxilated single Aluminum termination, as literature would suggest.

3.2 Cleaning

The chemical cleaning procedure detailed in Section A.2.1 is performed on all the substrates used in this thesis unless stated otherwise. It is a standard technique for cleaning Sapphire. The aggressive chemicals used in this procedure make it suitable for removing a broad range of contaminants from the surface.

3.2.1 Motivation

As is shown in Section 3.1.3, the surface of the pristine substrate is C and F-contaminated due to the long shelf time. In order to remove those, a harsh chemical treatment is necessary. Additionally, it would not be unlikely that some unidentified particles are present on the surface in concentrations below the measurement threshold of XPS. Therefore, the cleaning procedure should be as broad as possible, hence this choice.

3.2.2 Effect

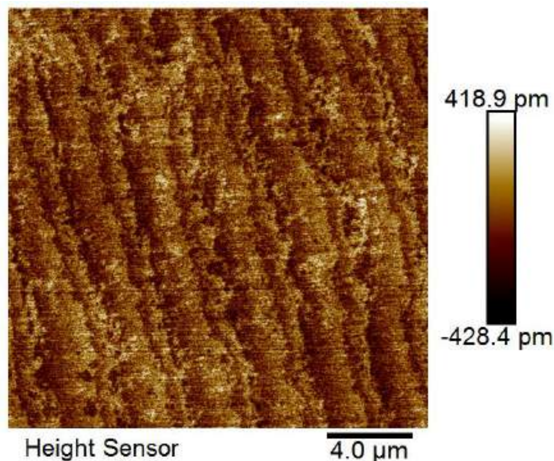

Figure 3.5: AFM image of the surface of chemically cleaned Sapphire wafers.

The acid clean applied in this thesis increases the roughness of the Sapphire substrates. An AFM investigation of a cleaned Sapphire substrate can be seen in Figure 3.5. Instead of being completely ruined, the terrace-and-step structures remain approximately conserved, though the steps are not as straight as on the initial substrates. The step height is not disturbed, and remains in the order of one atomic diameter. The RMS roughness has increased to 0.12 nm. The chemical cleaning procedure clearly impacts the surface, but not as dramatically as claimed in literature.

To assess the stability of the chemical termination of the surface after a clean, the Oxygen signals of the XPS characteristic are compared in Figure 3.6a. The figure shows six curves, respectively the bulk and surface Oxygen signals for a pristine sample, after it has been cleaned and after three days of storage in a Teflon container. The bulk spectra display the Sapphire Oxygen feature at 531 eV. The surface spectra additionally show the hydroxyl Oxygen bump (seen as a skewing of the curve towards 532 eV), indicating that the surface is likely hydroxylated. The bulk spectra are identical, and so are the surface spectra. The Oxygen signal is stable after cleaning and storage for three days.

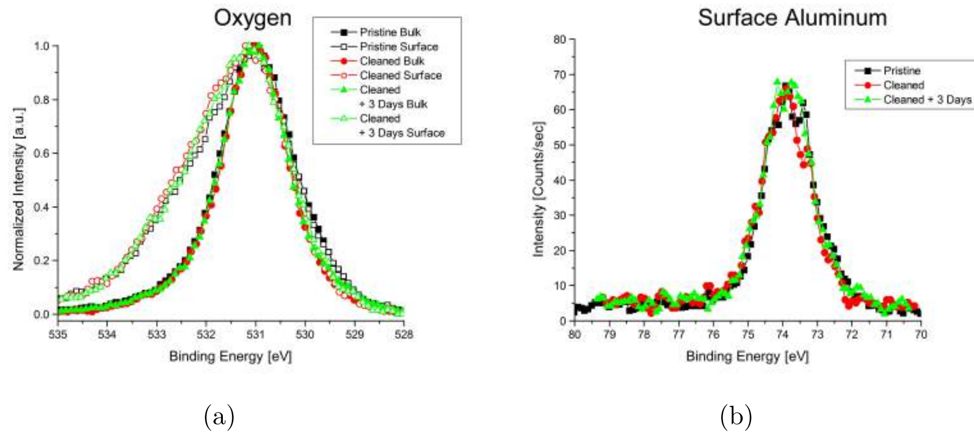

(a)

(b)

Figure 3.6: Angle-Resolved XPS spectra of cleaned samples for Oxygen (normalized) and surface Aluminum (absolute).

Additionally, the Al content of the surface of the cleaned wafer also is stable. Figure 3.6b shows the (absolute) curves for the signals of Al coming from the surface, for the same sample. The Aluminum signal is not affected by the cleaning nor by the three days storage[1]. The cleaning procedure very likely does not interfere with the hydroxylated Al termination of the surface.

The absolute C and F spectra are shown in Figures C.1 and C.2. Both the C and F surface contamination levels increase after the chemical clean, and again after three days. The contamination is due to contact with the Teflon containers, and ambient air, which makes those almost impossible to avoid (except by using metallic vacuum containers).

While the contamination by C and F is indeed expected to increase upon air/container exposure, the fact that it is low before cleaning is remarkable. This indicates that the pristine Sapphire wafers may have been treated by the retailer to avoid contamination. A possible way is by covering the substrate in a very thin layer of hydrocarbons, so that no additionnal contamination can be adsorbed.

[1]The variation of the integral of the three signals is in the order of the error between measurements.

3.3 Annealing

Annealing of a Sapphire wafer (mostly in O) prior to depositing a Cu layer is a widely accepted procedure in literature. In this section, the effect of high temperature steps on the quality of the Sapphire surface is analyzed.

3.3.1 Motivation

In Section 2.1.2, the position of the majority of literature concerning the optimal chemical termination for Cu epitaxy on Sapphire is discussed. According to both theory and experiment, an Oxygen termination would be best suited for this task. Therefore, different types of annealing steps in Oxygen (at "low", at $850°C$, and "high" temperature, at $1100°C$, and in Oxygen plasma, the procedures can be found in Appendix A.2.2) are investigated.

Additionally, a high temperature step should allow the surface structure of the Sapphire, which is affected by the harsh chemical etch discussed in the previous section, to reflow towards a flatter terrace-and-step structure.

3.3.2 Effect

The effect of the three methods of pre-deposition-annealing that are used in this thesis on the chemical termination and the surface structure of the Sapphire substrates are discussed here.

Low Temperature Anneal (LTA)

The terrace-and-step structure (see AFM image in Figure 3.7) generated upon annealing the Sapphire wafers at $850°C$ shows larger terraces than the original untreated Sapphire wafer. The steps are also better defined and more parallel than right after the chemical clean, though not as periodic as on the original wafers. The height of these steps is also in the order of one atomic step and the RMS roughness of the surface has increased to 0.15 nm.

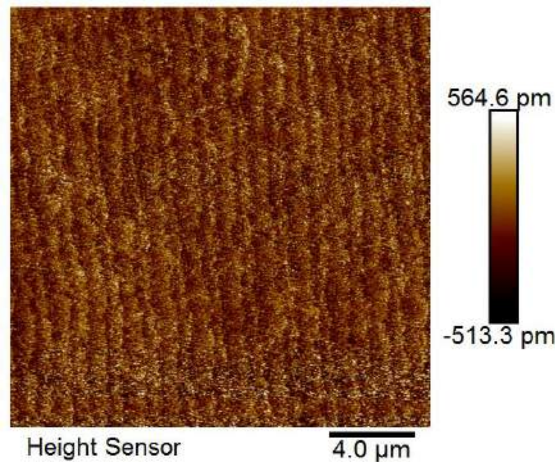

Figure 3.7: AFM image of the surface of Sapphire wafers after a chemical clean and a LTA.

The chemical analysis of the surface in the case of an LTA is given in Figure 3.8. The (normalized) Oxygen spectrum reveals that the hydroxyl-Oxygen fraction has decreased compared to the pristine

surface. This relative decrease of the hydroxyl fraction of the surface Oxygen indicates that the LTA influences the surface composition. The spectrum after three days storage does not look significantly different from the original LTA spectrum.

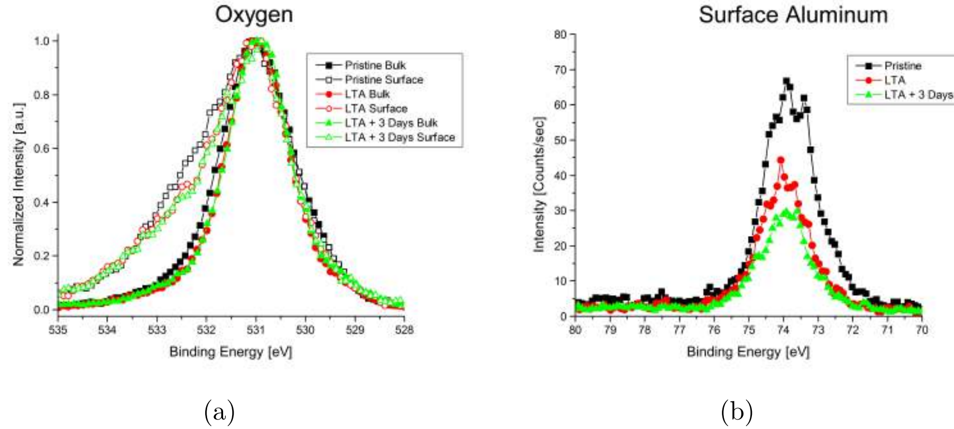

(a) (b)

Figure 3.8: Angle-Resolved XPS spectra of cleaned + LTA samples for Oxygen (normalized) and surface Aluminum (absolute).

The Aluminum spectrum is shown in absolute terms in Figure 3.8b. The intensity of the signal significantly decreases after a LTA (the integral, which is proportional to the concentration of Al decreases by $41\% \pm 1\%$). The signal also slightly decreases after three days of storage ($25\% \pm 1\%$). The LTA clearly has an influence on the Aluminum content of the Sapphire surface. Additionally, the XPS measurements revealed an increase in the Fluorine contamination of the surface (by a factor of respectively 5 ± 1 and 2 ± 1[2]), as compared to the pristine and cleaned state.

High Temperature Anneal (HTA)

The terrace-and-step structure (see Figure 3.9) generated upon annealing the Sapphire wafers at $1100°C$ has the same dimensions as on the original unprocessed Sapphire wafers. The terraces have the same width and are nicely aligned, while the steps also have a height in the order of one atomic step. The AFM image also shows that the substrate is covered with brighter points. These might be particles. The height scale shows that these are not really high (at most 1 nm). The RMS roughness is nevertheless influenced and increases to 0.18 nm. Their composition will become clear from XPS measurements.

[2] Relative concentrations. The absolute signals remain in the order of the pristine and cleaned signals. Both values are close to the measurement threshold. The ratio can be interpreted only qualitatively.

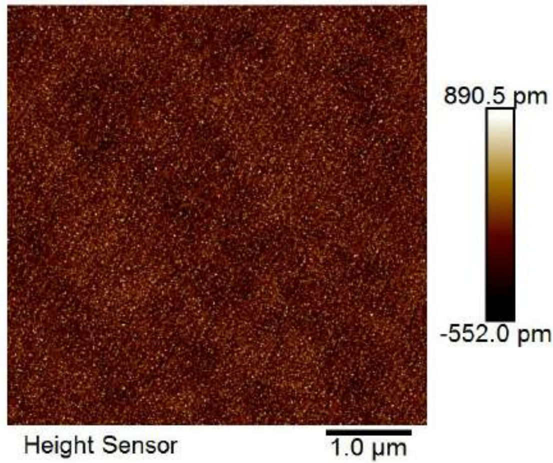

Figure 3.9: AFM image of the surface of Sapphire wafers after a chemical clean and a HTA.

The XPS spectra for the O signal can be easily interpreted (see Figure 3.10). Just like for the case of the LTA Oxygen spectra, it can be seen that the feature for hydroxyl Oxygen at 532 eV has decreased as compared to the pristine sample. The bulk spectra are also influenced (in the range of $E_B = 529..530eV$), but the deviation is too small to draw a solid conclusion.

The Al spectra also show a significant effect of the HTA. Here it is not possible to detect a trend, because the signal increases after the HTA (by $19\% \pm 1\%$) and decreases again thereafter (by $33\% \pm 1\%$). What can be said is that the HTA clearly influences the chemical termination of Sapphire. The absence of a trend indicates that this is not predictable. This is an important drawback.

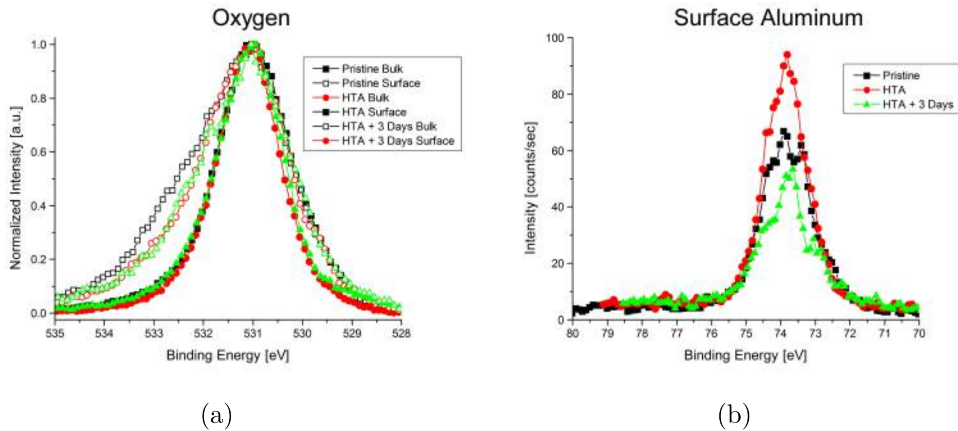

Figure 3.10: Angle-Resolved XPS spectra of cleaned + HTA samples for Oxygen (normalized) and surface Aluminum (absolute).

The combined analysis of the Oxygen- and Aluminum-spectra indicates that the effect of the HTA is similar to the effect of the LTA from the point of view of Oxygen. The effect on the Aluminum concentration is more pronounced, and unpredictable.

Finally, Table 3.1 presents the relative concentrations of all the species detected on the surface of HTA Sapphire samples. Besides the expected C and F contaminations,

there appears to be a non negligible amount of Na and Si. These contaminants likely are at the origin or the bright dots detected on the AFM picture, and constitute a significant issue.

Table 3.1: Relative surface concentrations of atomic species. The error is in the order of 1%.

Species	Pristine	Cleaned and HTA	Three days later
Aluminum	31.06	26.18	15.70
Oxygen (Sapphire)	37.74	37.36	33.51
Carbon	19.98	11.35	22.8
Fluorine	ϵ	4.65	5.86
Oxygen (OH)	10.18	5.58	4.74
Potassium	N.A.	ϵ	ϵ
Sodium	N.A.	7.14	7.65
Silicon	N.A.	6.93	9.13

Oxygen Plasma Treatment (OPT)

The terrace-and-step structure (see Figure 3.11) generated upon annealing the Sapphire wafers in Oxygen Plasma can be related to the structure after a LTA. The surface is not significantly more damaged than in the case of a LTA, with the exception of the few black dots present in the image. These correspond to small pits in the surface (depth of half a nm). These pits may negatively influence the quality of deposited Cu layers. The RMS roughness of the surface is 0.15 nm

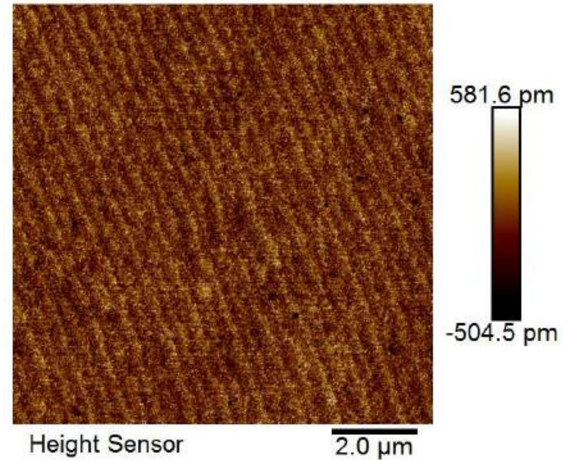

Figure 3.11: AFM image of the surface of Sapphire wafers after a chemical clean and OPT.

The chemical analysis of the surface of the Sapphire samples after Oxygen plasma treatment is shown in Figure 3.12. The bulk Oxygen signal is identical to spectrum of the pristine wafers, as is

the case for LTA and clean also. The surface Oxygen signal shows a slight increase in the hydroxyl-Oxygen feature, unlike in the previous procedures. The Al signal is very strongly influenced by the O plasma treatment. An additional feature at 75.5 eV appears and is ascribed to $Al - F$ bonds. This indicates that the O plasma treatment not only influences the surface contamination, but also the chemical nature of the crystal itself, be it locally.

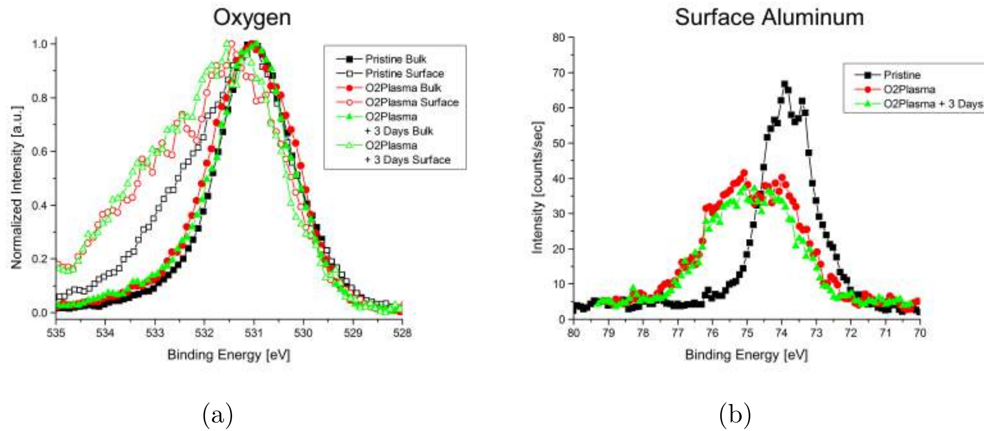

(a) (b)

Figure 3.12: Angle-Resolved XPS spectra of cleaned + Oxygen plasma samples for Oxygen (normalized) and surface Aluminum (absolute).

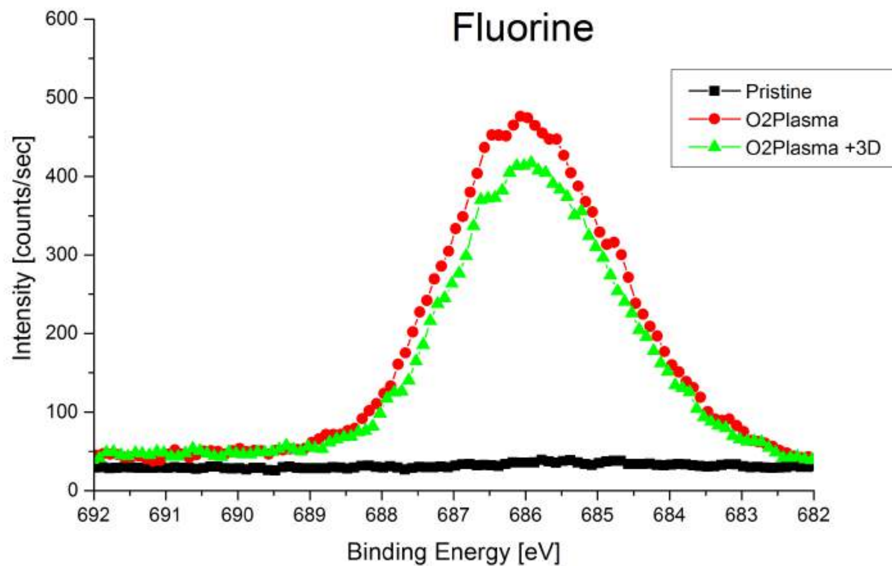

Figure 3.13: Angle-Resolved XPS spectra of cleaned + Oxygen plasma samples for surface Fluorine.

The Fluorine signal is also interesting, since an important amount of $Al - F$ bonds was detected. It is shown in Figure 3.13. The signal for the pristine surface cannot be discerned from the noise level. On the pristine Sapphire, the F contamination is of the order of the measurement accuracy. This spectrum can be compared with the peaks related to the plasma treated samples. There clearly is a large F contamination on the surface.

3.4 Sources of variability

In the previous sections, it is pointed out that some of the procedures used in this thesis result in an unstable and/or heavily contaminated surface termination. The importance of this termination, and of its stability cannot be stressed enough. Whereas literature (see Section 2.1.2) claims that the O-termination is the most suitable for Cu epitaxy, it goes together with unstable Al surface contents and often contamination (mainly C and F but also Na and Si). This is an important drawback for industrial processes.

A reason for the increase in contamination in the case of the Oxygen treatments in general can be postulated. In all three cases (LTA, HTA and plasma), the Sapphire substrate is heated up significantly in an Oxygen (ions) atmosphere. When the samples are taken out, they may still be at temperatures above $100°C$, and covered in the reactive oxygen termination. As soon as the surface comes into contact with air (or Teflon) it will saturate with whatever atomic species are in its vincinity.

If $Cu\,(111)$ is to be deposited on a Sapphire surface, it must be accurately controlled. Any kind of contamination (F, Na, Si) may be problematic, even more so if it interferes with the crystalline lattice itself ($Al - F$ bonds). The single chemical clean does not interfere significantly with the chemical termination of Sapphire, but it will remove contaminants and particles which may be below the detection levels. Unfortunately, as soon as the substrates come into contact with Teflon containers, the C and F contamination can be restored. The Cu deposition should happen immediately after the chemical cleaning, ideally in the same room.

3.5 *In situ* Vacuum Anneal

In this work, several Cu deposition experiments are performed where the Sapphire substrate is annealed in vacuum *in situ* right before sputter deposition. This procedure is systematically performed in combination with a chemical clean and a LTA.

3.5.1 Motivation

The purpose of annealing Sapphire wafers in vacuum right before Cu deposition is to desorb water molecules from the surface. It will not restore the Oxygen termination,

in Section 2.1.2, it is shown that the hydroxylated Aluminum termination is the most stable in vacuum.

3.5.2 Effect

The effect of this procedure onto the surface of the sample is hard to assess. The surface topology should not be affected, the temperature of this anneal ($200°C$) is too low compared to the temperatures used in LTA and HTA. The effect on the chemical termination cannot be measured, no *in situ* XPS measurements are possible. There is a good reason to doubt that this restores the O-termination of the substrate, as was explained in Section 2.1.2, the Al-termination is thermodynamically the most stable in vacuum. Theoretically the *in situ* vacuum anneal should result in a (de-) hydroxylated Al termination.

Whether the Al termination resulting from an *in situ* vacuum anneal is hydroxylated is not known. XPS measurements performed at room temperature indicate that the hydroxylation is maintained, even in vacuum. The same question in the case of $200°C$ remains unanswered, no XPS characterisation could be carried out *in situ*.

3.6 Ion Milling

Two samples are subjected to a light Ion Milling step, executed *in situ* right before the Cu deposition procedure.

3.6.1 Motivation

According to Scheu et al. [35], this procedure can be used to deplete a surface from hydroxylation. Note that in this work, the energy of the Ar ions is taken much lower than what Scheu et al. prescribe. This because the setup does not allow such high energies, and because of the (realistic) risk that this would damage the surface of the Sapphire.

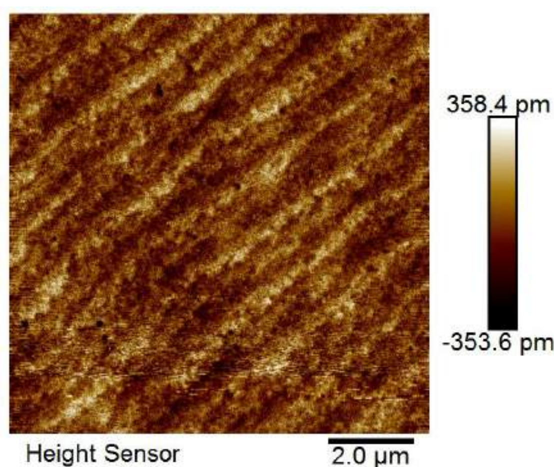

Figure 3.14: AFM image of the surface of Sapphire wafers after a chemical clean and an Ion Milling treatment.

3.6.2 Effect

Regardless of the possible dehydroxilation caused by this process step (which could not be investigated, due to the impossibility to carry out XPS measurements *in*

situ), the surface of the Sapphire substrate is slightly damaged. An AFM image is shown in Figure 3.14. The results are not significantly different for the different sputtering energies and durations, in both cases the RMS roughness is relatively low, at 0.11 nm. Though the terrace-and-step structure is still present, and looks generally similar to the one observed in the case of the chemical clean, the surface arguably looks slightly more damaged. The same black pits (still with depths of approximately half a nm) are present as in the case of an Oxygen Plasma treatment.

The available data does unfortunately not provide enough information on the effect of an Ion Milling procedure. The quality of subsequently deposited Cu is heavily compromised by this procedure, but this might be due to the chemical termination of the Sapphire as well as to the surface morphology.

3.7 Conclusion

In this chapter, the different surface preparation methods applied on the Sapphire substrates are investigated, and their effects, both chemically and topologically, are analyzed. The results indicate the decisive effect of these procedures on the chemical termination and topology of the Sapphire surface.

The chemical cleaning procedure does not influence the chemical termination of the Sapphire surface. Both the Oxygen and Aluminum XPS spectra are identical. It only removes undesired contaminants. C and F contamination is restored (and increases) as soon as the cleaned wafers are stored in a Teflon container.

The LTA and HTA procedures do influence the chemical termination of Sapphire. A clear decrease of the hydroxyl-Oxygen fraction can be measured, and the Al signal is influenced as well (though not in a predictable way). Additionally, the two procedures tend to introduce contaminants on the surface. This is best seen in the case of the HTA, where significant amounts of Na and Si are detected.

The Oxygen plasma treatment strongly influences the O and Al contents. Even more importantly, the Sapphire surface ends up covered in Fluorine, and presents $Al - F$ bonds. A chemical reaction takes place between the Sapphire Al and the F. The reactivity of the Sapphire surface is likely enhanced by the energetic Oxygen plasma to which it is exposed.

Additionnal XPS data is given in Appendix C. The absolute XPS spectra for O, Al, C, and F are given for every procedure discussed in this chapter. The calculated concentration profiles are given as well.

Chapter 4

Deposition of the Cu layer

In this chapter, the experimental work conducted on the deposition of Cu and the subsequent characterisation results are discussed. The Cu layers discussed here are analyzed as deposited, before the subsequent anneal treatment. The analysis of the final epitaxial state of the Cu, after thermal treatments, is a topic on itself and will be treated in Chapter 5.

In the first section, the desired Cu layer is discussed. This target is split into two separate topics. On the one hand, an attempt is made to reproduce the State-of-the-Art. These results are suboptimal, unfortunately. Up to this date, no group has been able to deposit a perfectly epitaxial Cu layer (without twinning of the ORs, see Section 2.1.1). Therefore, an additional subsection is added, where the updated objectives are given (aiming at perfectly epitaxial Cu without twinning).

Following on the discussion of the objective of this thesis, the general procedure followed to reach it is discussed. As will become clear throughout this chapter, it appears that this procedure may be much simpler than what transpires from literature. The implemented simplifications have no negative effect on the result of the procedure, on the contrary.

Furthermore, the influence of some of the deposition parameters and of the initial quality of the substrate is discussed. The influence of the sputtering parameters is investigated, and the effect of modifying them is studied. The properties of the substrate are discussed in the following section. It will become clear that the substrate imposes a condition *sine qua non* for the epitaxy of Cu.

Finally, two sections are dedicated to the issues encountered during this thesis, and the lessons and conclusions one can draw from those. The differences between the target as derived from the State-of-the-Art, and the updated target as it appears from this work, are highlighted.

4.1 Objective

In this section, the target structure for as-deposited Cu is described. This is an intermediary target structure, meaning that, in order to achieve perfect epitaxy of Cu, it should undergo a high temperature treatment. In practice, this treatment (which is equivalent to annealing the Cu layer) is provided by the Graphene growth cycle, where the process temperatures typically are in the order of $1000°C$.

The result of this thermal treatment is the topic of Chapter 5. Without overlapping with the content of the next chapter, Section 4.1.2 describes the qualities of the Cu layer which, in retrospect, would yield the best results.

4.1.1 State-of-the-Art

In the literature review of this thesis, a discussion of the current State-of-the-Art concerning epitaxial deposition of $Cu\,(111)$ is given (see Section 2.1). The results of Miller et al. [1] stand out in this discussion. The authors succeed in depositing a Cu layer on Sapphire that, upon annealing at typical Graphene growth temperatures, yields an excellent result, as compared to the State-of-the-Art. The annealed $Cu\,(111)$ layer consists of perfect OR-I, although with significant twinning.

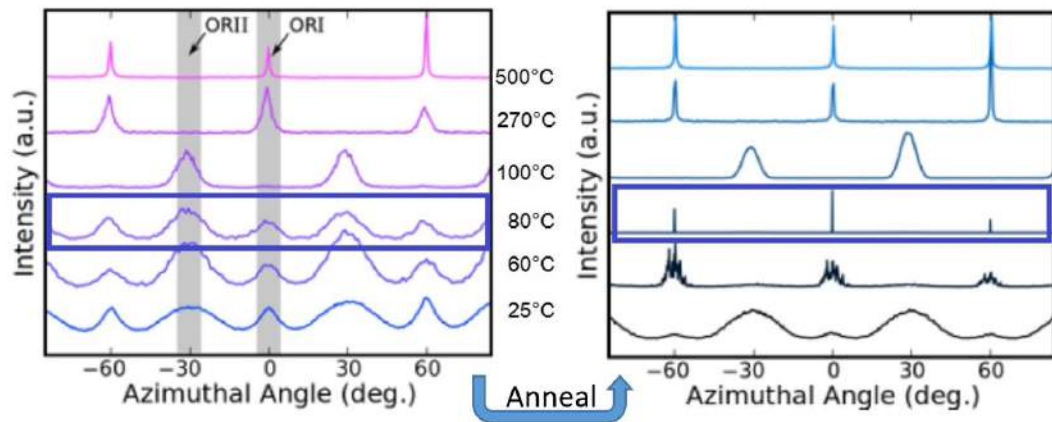

Figure 4.1: XRD Line scan for as-deposited (left) and annealed (right) $Cu\,(111)$ crystals for different substrate deposition temperatures. From Miller et al. [1].

The relevant results of the authors are shown in Figure 4.1, in the blue rectangle. The Cu deposited at a temperature of $80°C$ adopts an epitaxial yet significantly twinned structure upon annealing. Counterintuitively, the crystalline structure of the as deposited Cu layer should not consist of one OR. On the contrary, it should consist of many small grains with different orientations (the FWHM of the peaks in the Line scan of Figure 4.1 contains information concerning the size and distribution from the grains, the higher this FWHM, the smaller the grains; additionally, a high FWHM also indicates these small grains all have slightly different in-plane orientations). No

numerical value for the ratio of the two ORs was given, but a very rough estimate can be made: 60% OR-II and 40% OR-I.

The reason small grains with different in-plane orientations should (in theory) adopt a monocrystalline structure is the following. The different ORs are not thermodynamically equivalent in terms of stability (see Section 2.1.1). One could therefore assume that, upon exposure to temperatures very close to the melting point, the resulting structure will contain only one of the two ORs (the most stable one). This also means that, once the most stable crystalline structure of $Cu\,(111)$ has been obtained, additionnal high temperature steps should not alter this structure. Most of the research into Cu epitaxy, including the present work, is based upon this assumption.

The work of Miller et al. [1] is the starting point of the experimental work in this thesis.

4.1.2 Thesis objective

The literature target discussed in the previous section is everything but optimal. The reported Cu layers indeed consist of OR-I exclusively, but contain both twins in approximately equal amounts. The ideal result would of course be the Cu layer which, once it has been annealed, contains only one twin, e.g. OR-Ia. The as-deposited crystalline structure of the Cu layer which leads to this epitaxial Cu crystal upon annealing was, at the beginning of this work, not yet known.

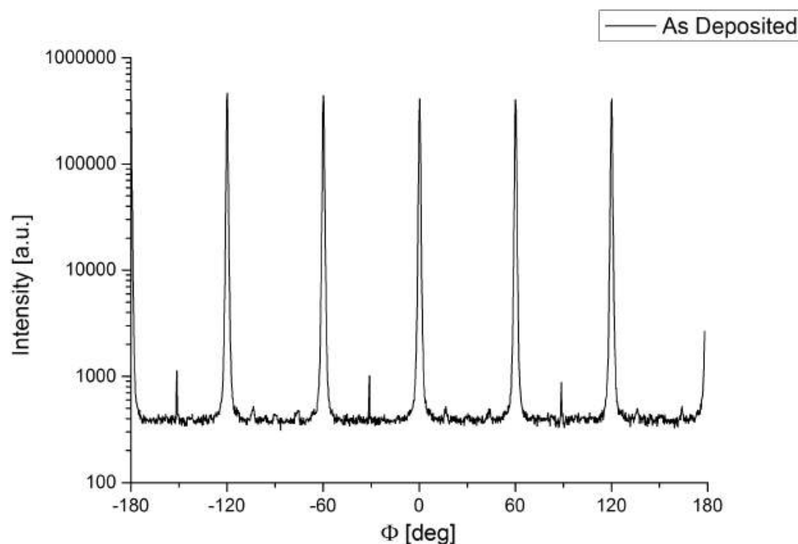

Figure 4.2: XRD Line scan for an as-deposited sample that, upon annealing, adopts untwinned epitaxial $Cu\,(111)$ grains.

Empirical results show that this is possible, despite this never having been reported in literature. The crystalline structure that would, upon thermal treatment, yield a wafer-scale Cu single crystal is shown in Figure 4.2. The reference orientation for the Φ axis is chosen to be the same as in Figure 4.1, therefore the Cu shown here is exclusively OR-I. The small peaks at positions ($-150°$, $-30°$, $90°$) originate from the Sapphire background signal (see Appendix B).

The crystalline structure of the Cu presented in Figure 4.2 displays exclusively OR-I, where the Sapphire background is also clearly visible. In Section 4.3, this is the target structure that will be pursued.

4.2 Towards the State-of-the-Art

In this section, an account is given of the work aimed at reproducing the results of Miller et al. (mix of both ORs in as stated in Section 4.1.1). The reader should keep in mind the conclusion of the previous chapter. The surface of Sapphire samples shows significant contamination, after annealing in Oxygen. Additionally, the Al content of the surface is not stable in cases of Oxygen treatments. The influence of this contamination, and of the stability of the chemical termination on the crystalline quality of sputtered Cu samples is explored here.

Two major sources of variability are identified in these trials. The first one, the issues with the Oxygen termination, has already been partially treated in Chapter 3. There, XPS is used to probe the surface of Sapphire samples after Oxygen treatments (LTA, HTA, and Oxygen plasma). These systematically result in a heavily contaminated surface, and in some cases induce variations in the Al and hydroxyl-Oxygen content. A solution to this problem is nevertheless proposed. The second issue is related to the substrate temperature sensitivity of the sputtered Cu layer. Miller et al. [1] advocate a sputtering step with a substrate temperature of $80°C$. In the present work, it becomes clear that the slightest temperature variation can have an important impact on the crystalline structure of Cu, for Oxygen terminated substrates.

4.2.1 Stability of the Oxygen termination

The lack of stability of the Oxygen termination has already been discussed in detail. Its effect on the quality of the as-deposited Cu layer can be seen in Figure 4.3. Despite both samples having undergone exactly the same procedure, the results are significantly different from one another. The first curve presents a relative content of OR-I : OR-II equal to 37% : 63%, which is equivalent to the ratio in the publication of Miller et al.[1]. The second sample presents a relative content of OR-I : OR-II equal to 84% : 16%. These ratio's are calculated as the integral underneath the curve (between $-15°$ and $15°$ for OR-I and between $15°$ and $45°$ for OR-II), and are corrected for the noise level of the characterisation tool.

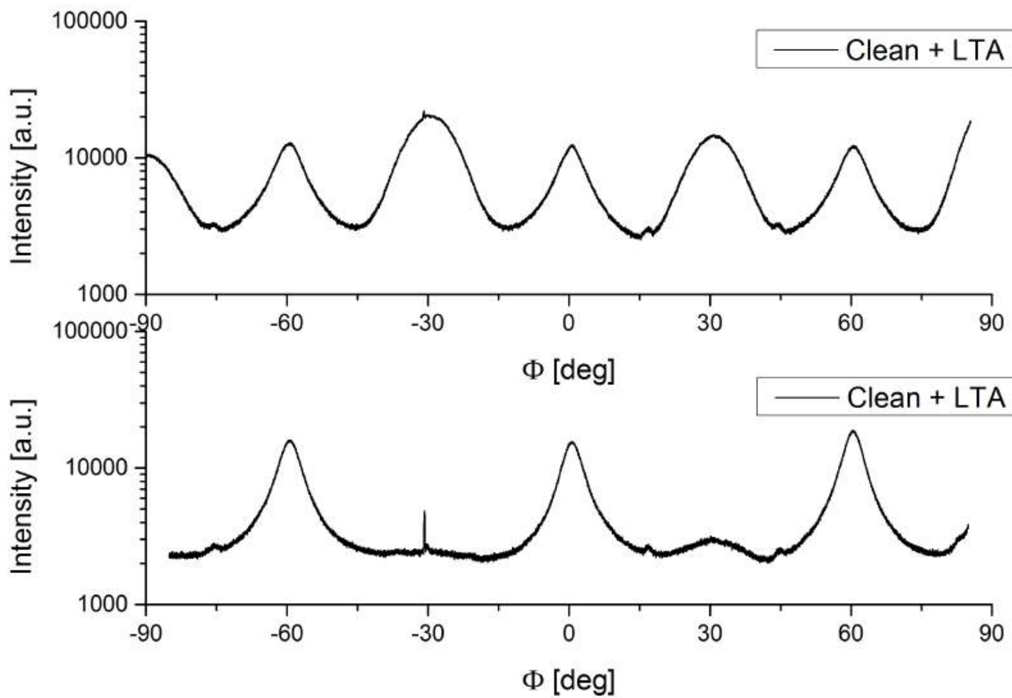

Figure 4.3: Line scan of the as-deposited Cu structure, for two samples deposited after a LTA. (procedure in Appendix A.3.2).

In an attempt to implement a reliable Oxygen termination, different surface preparation techniques are used in the previous chapter (being: LTA, HTA, Oxygen plasma, and Ion Milling). The effect of these four procedures on the quality of as-deposited Cu layers is shown in Figure 4.4.

As can be seen in Figure 4.4, the as-deposited crystalline structure for Cu is entirely compromised in the case of HTA, Oxygen plasma, or Ion milling treatments. The curve for LTA is shown as well, but again these results are not reproducible. In order to restore the reproducibility, and still keep the Oxygen termination of Sapphire, an Oxygen anneal step should be executed *in situ*, right before the Cu deposition. This would cause a few problems. First, the Cu target used for sputtering should better not come into contact with Oxygen, hence the anneal should be executed in a separate chamber. Second, the Oxygen termination is not the most stable one in vacuum (see Section 2.1.2), so it is no sure that even an *in situ* Oxygen anneal would result in a stable and homogeneous Oxygen termination.

Figure C.8 gives additionnal information concerning the respective stability of the two different (Oxygen and Aluminum) terminations of Sapphire wafers.

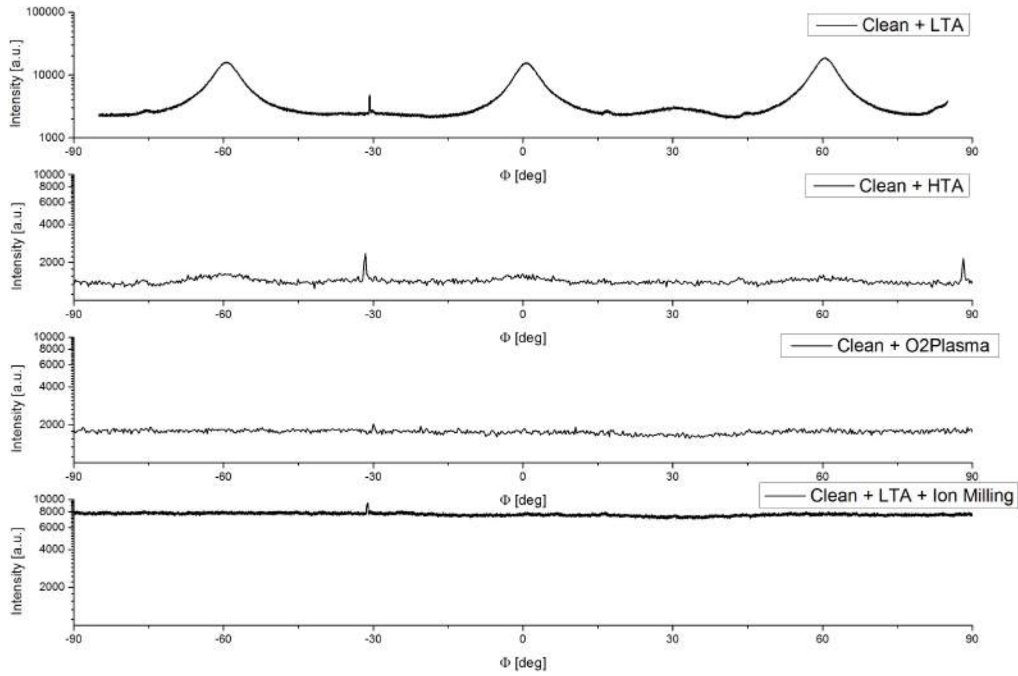

Figure 4.4: Line scan of the as-deposited Cu structure, for the different surface treatment procedures described in Chapter 3.

4.2.2 *In situ* vacuum anneal

To decrease the surface contamination originating from the Oxygen treatments, an *in situ* vacuum anneal is used. The samples are annealed in vacuum at $200°C$ and Cu is deposited at $70°C$, close to the $80°C$ prescribed by Miller et al. [1]. The results, unfortunately, bring to the light a new issue, the very sensitive dependence on the substrate temperature during sputtering.

4.2.3 Temperature Window

In an attempt to replicate the results of Milller et al. with the highest accuracy, the samples are annealed in vacuum and the deposition temperature is increased to $70°C$. The XRD characteristics of three samples deposited very close to this temperature are shown in Figure 4.5. The OR-II content decreases from 14% in the $68°C$ sample to below the noise level in the $72°C$ sample.

The temperature is shown to have a very important influence. The reason for choosing $70°C$ instead of $80°C$ for the substrate temperature also becomes apparent from these curves. The Cu deposited at the lowest temperature has a characteristic which is closest to the results of Miller et al. [1]. The significant influence of a small variation

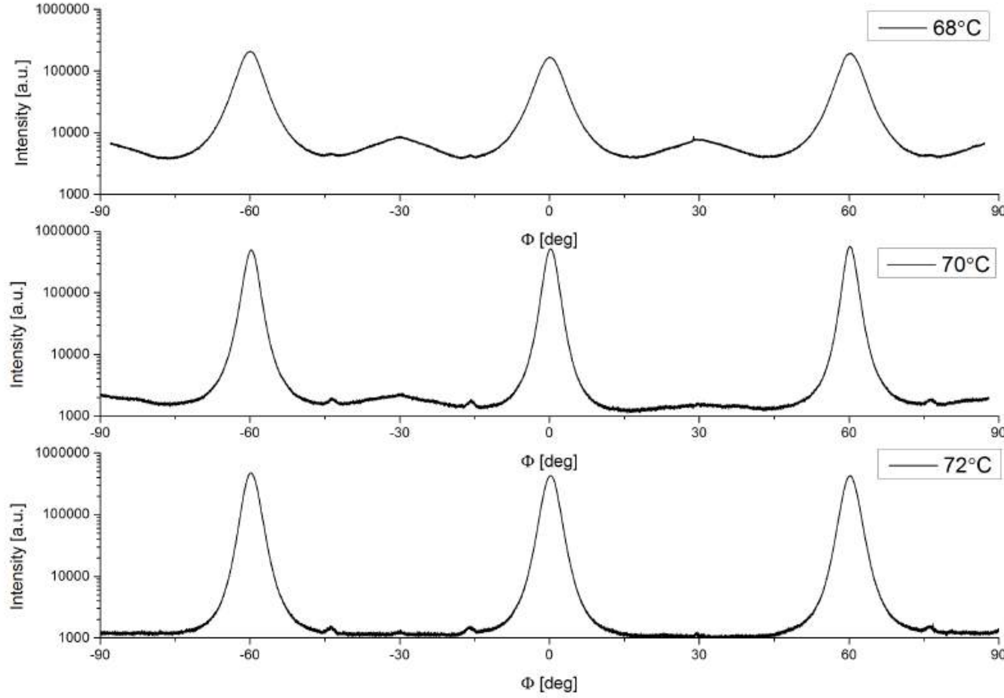

Figure 4.5: XRD Line scan of the as-deposited Cu structure, for three samples deposited at slightly different substrate temperatures after an *in situ* vacuum anneal.

in the deposition temperature on the result makes this procedure impractical. The Oxygen treatments will be discarded in the following sections.

4.3 Towards the thesis objective

In an attempt to improve upon the unreliable results reported in the previous section, the process flow is modified to exclude steps intended to yield an Oxygen termination. This proves to be a fruitful technique, with results (after thermal treatment of Cu) far exceeding the expectations. The modified process flow used in this section is detailed in Appendix A.3.3. Note that the deposition parameters vary very strongly (up to an order of magnitude), depending on the setup used for the deposition. Nevertheless, the deposition yields in all cases pure $Cu\,(111)$ with twinning present, as can be seen in Figure 4.6.

All four samples are cleaned and immediately Cu sputtered. The parameters at which these results are obtained can be found in Appendix A.3.3. At first sight, the result for the Microscience sample deposited at room temperature seems different from the three others (higher FWHM). The annealed structure does show significant similarities however (see Section 5.5.2), hence the mention here.

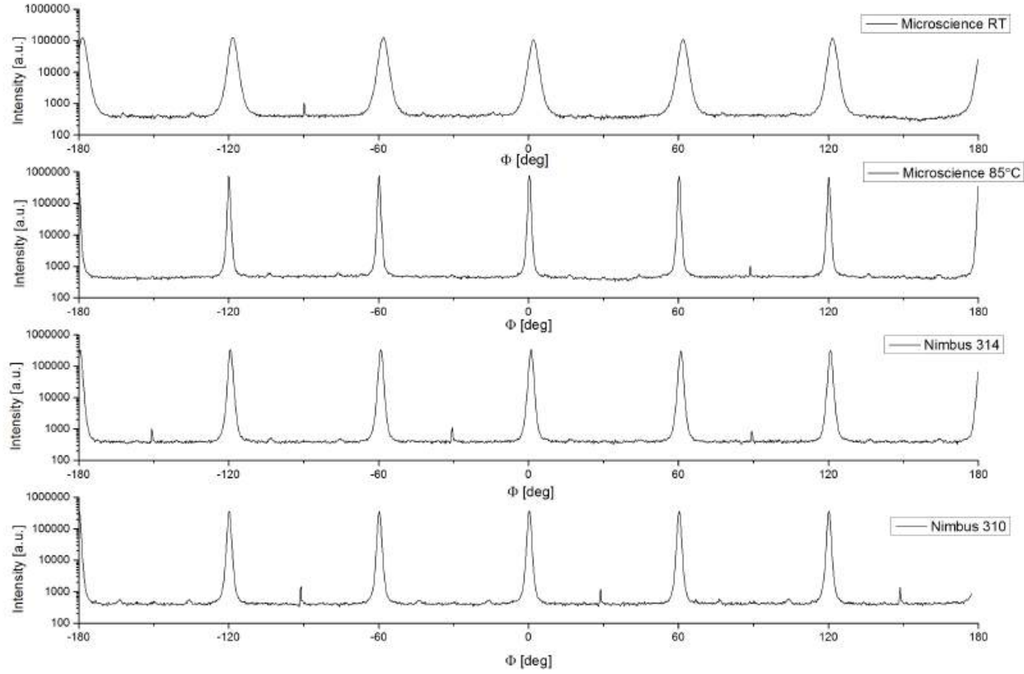

Figure 4.6: XRD Line scan of the as-deposited Cu structure, for four samples deposited under different conditions.

4.4 Influence of intrinsic parameters

The obvious question that arises, when faced with the different sputtering parameters used in the different setups, is "why change them?". The answer is very simple. These three tools have slightly different specifications, which are most obvious in the sputtering power. Both the Nimbus tools have a standard sputtering power of 3000 W, whereas for the Microscience tool the standard (used in this thesis) power rating is 100 W. It could have been ramped up, but nowhere close to the power level of the Nimbus tools. Note that, even though the power ratings are significantly different, the voltages are similar (around 460 V), it is the current ratings that strongly differ. This can be related to the size of the tool, the Nimbus tools have much larger Cu targets. The current may be significantly higher, the current density impacting the target actually is in the same order. Since the voltages are the same, the impact power per unit area (power density) is comparable as well.

The important conclusion that can be drawn from the aforementioned results is the following: despite having changed several deposition parameters, it was possible to reach a highly reproducible quality of Cu (shown in Figure 4.2), regardless of the setup being used.

The different sputtering parameters are shown in Table 4.1. The two Nimbus tools differ in base and working pressures. The crystalline structure and thickness of the Cu layers deposited with the Nimbus tools is nevertheless identical. This is counterintuitive, the sputtering pressure should influence the resulting Cu layer, and the difference is too significant to ignore.

Table 4.1: Comparison of the different Cu sputtering setups.

Parameter	Microscience	Nimbus 310	Nimbus 314
Base Pressure $[mbar]$	$1.0 * 10^{-7}$	$4.0 * 10^{-6}$	$8.0 * 10^{-7}$
Sputtering Pressure $[mbar]$	$1.7 * 10^{-3}$	$6.0 * 10^{-3}$	$4.0 * 10^{-3}$
Temperature $[°C]$	RT...85$°C$	RT	RT
Time $[sec]$	900	173	173
Voltage $[V]$	452 ± 10	460	460
Current$[mA]$	223 ± 4	6500	6500
Power$[W]$	100	3000	3000
TSD $[mm]$	$60..80 \pm 10$	50	50

In the previous sections, the decisive effect of the temperature on Oxygen treated substrates was reported. Here, the TSD and temperature were changed. When the temperature decreases, a similar structure is deposited at a lower TSD. Consider the influence of temperature and TSD on the adatom mobility of the surface (μ). The latter increases with increasing temperature but decreases with increasing TSD. The effects of the TSD and temperature can therefore cancel each ofther out (from the point of view of μ).

The different parameters yet similar results of the three tools can also somewhat be justified. The power density is assumed constant, which is a reasonable assumption. The temperature, pressure and TSD influence the adatom mobility (μ) on the substrate surface. Again, the mobility increases with temperature, and decreases with the pressure and TSD. Compared to the Microscience tool, the Nimbus parameters are: higher pressure ($\mu \downarrow$), lower or equal temperature ($\mu \downarrow$ or $\mu \rightarrow$) and lower TSD ($\mu \uparrow$). These effects may cancel each other out, which allows to qualitatively justify the identical crystalline structures.

4.5 Influence of extrinsic parameters

The decisive factor, regardless of the sputtering tool or parameters, is determined to be the substrate preparation. The present section will go more into detail into the

importance and effect of the procedures preceding the Cu deposition. It cannot be stressed enough that the stability of the chemical termination of the surface has a decisive (and in the work reported there, negative) effect on the crystalline properties of the as-deposited layer. It should not be surprising that, in the present case as well, the most important factor is -again- the substrate preparation.

The case for the importance of substrate preparation, for depositions being performed in the microscience lab, has already been made in Section 4.2. Here, instead of pointing out the variability of results when a LTA is used, a comparison will be made between samples having undergone different treatments prior to deposition.

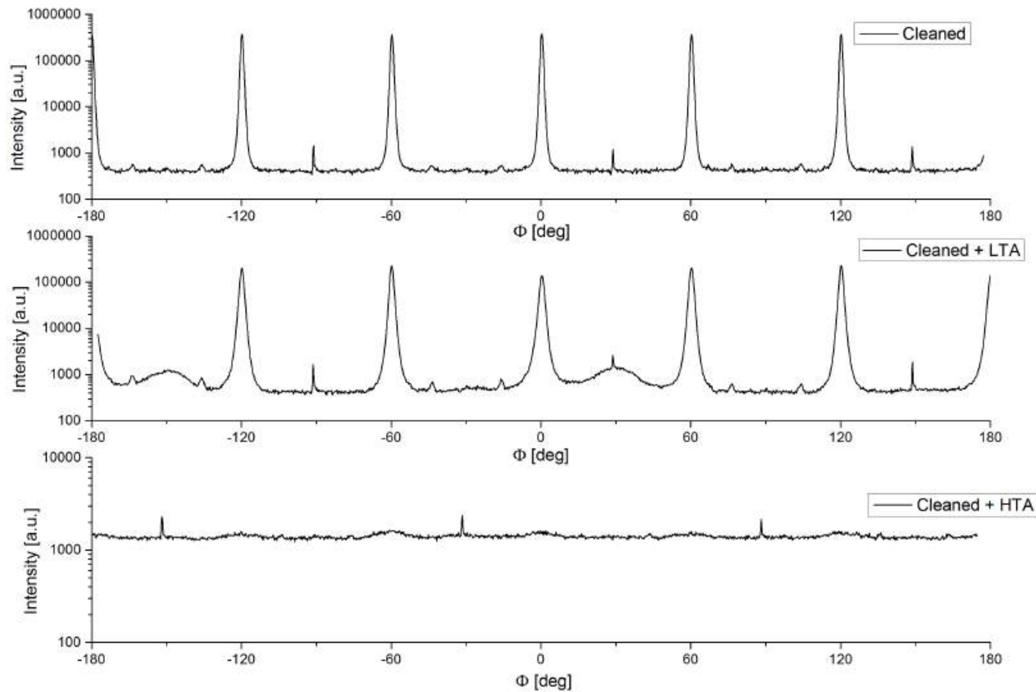

Figure 4.7: XRD Line scans of three samples with different substrate preparations.

The results of the same deposition run, for three samples with different pre-deposition treatments can be seen in Figure 4.7. The influence of annealing the Sapphire wafers in an Oxygen environment is obvious. This effect seems to be more pronounced for a higher temperature anneal. The distinction between the OR-I peaks and the minor OR-II peaks can be made in the case of the LTA. When the samples undergo a HTA, this distinction disappears, the (very small) $Cu\,(111)$ grains are randomly oriented on the sample, with an approximately even distribution.

4.6 Conclusion

In the present chapter, the experimental results for the as-deposited Cu layers are discussed. The target crystalline structure for the as-deposited Cu grains, as well as the influence of the two decisive factors, the substrate preparation and the deposition parameters, are summarized in this section.

4.6.1 Objective

The feasibility of both the State-of-the-Art and thesis objectives has been investigated. The results show that the procedures (Oxygen treatments and ion milling of the surface) advocated in literature do not yield reproducible results. On the other hand, limiting the pre-deposition processing to a chemical clean shows promising and reproducible results. The main factor influencing reproducibility in our experiments is likely the surface termination and contamination.

4.6.2 Influence of the substrate preparation

The substrate preparation is the main factor in depositing a Cu film that, upon annealing at Graphene growth temperatures, will form a wafer-scale epitaxial grain. The intermediate result, which is described in the previous section, has been shown to depend mostly on the substrate preparation. This factor strongly influences the crystalline structure of as-deposited Cu layers. Additionally, the stability of the subsequent surface properties has been shown to be a decisive element in the reproducibility of results.

4.6.3 Influence of the deposition parameters

The influence of the deposition parameters has not been investigated in as much details as the influence of the substrate preparation. Indeed, it seems that the same crystalline quality of Cu can be obtained at different sputtering parameters. For clarity, the four parameters that can be changed here are: the sputtering pressure, temperature, power and target-to-substrate distance (TSD).

The results of this chapter indicate that an empirical relationship might exist which, in the parametric space of Cu sputtering, gives all the sets of parameters for which the result is a metallic layer with exactly the desired properties.

Chapter 5

Graphene Chemical Vapor Deposition

In this final chapter, the procedure used for growing Graphene and its effect on the quality of an epitaxial Cu layer are discussed. Despite the name of this chapter, the focus does not lie on the properties of Graphene. Instead, the behaviour of Cu at high temperatures is analyzed.

The previous chapters have focused on the quality of Cu films, and the procedures that influence it. The present chapter follows the same line of conduct. It is likely that solving the problem of the substrate quality will largely enhance the quality of CVD Graphene. Tuning Graphene growth parameters is outside of the scope of this work.

In the first section of this chapter, the final target of this thesis is discussed. The measurable quality of this target is the crystalline structure of Cu. The many factors on which this crystalline structure depends have, in a large part, already been discussed in the previous chapters. In this chapter, the story is concluded, and a second section discusses the effects of all these factors on the final target.

Furthermore, one section is dedicated to the Graphene that was, in some cases, grown on the Cu layers. The properties of these Graphene layers are discussed.

Additionally, the issues and (yet) unsolved problems related to growing Graphene on Cu are listed. The problem of polycrystalline substrates negatively influencing the properties of Graphene can be considered solved. Nevertheless, this only highlights the many issues that still remain, some of which could prove much more critical than the one tackled in this work.

Finally, a short conclusion discusses the relevance of the results collected concerning the Cu quality, and possible paths for building further upon this research.

5.1 Thesis objective

The objective of this thesis is *to investigate the production of a template suitable for the growth of a large crystal of Graphene*. In this chapter, the procedure to reach this objective is finalized. The present section describes the two criteria used to determine whether the objective of this thesis is realised.

5.1.1 Cu quality

The *Cu* substrate resulting from the Graphene growth procedure should be perfectly monocrystalline. This means that its surface should consist exclusively of one giant grain of *Cu* (111). Whether this requirement is met can be easily measured with an XRD Line scan. If the curve consists of three very sharp peaks with a 120° periodicity, this condition can be considered fulfilled. An example of such an XRD spectrum is given in Figure 5.1.

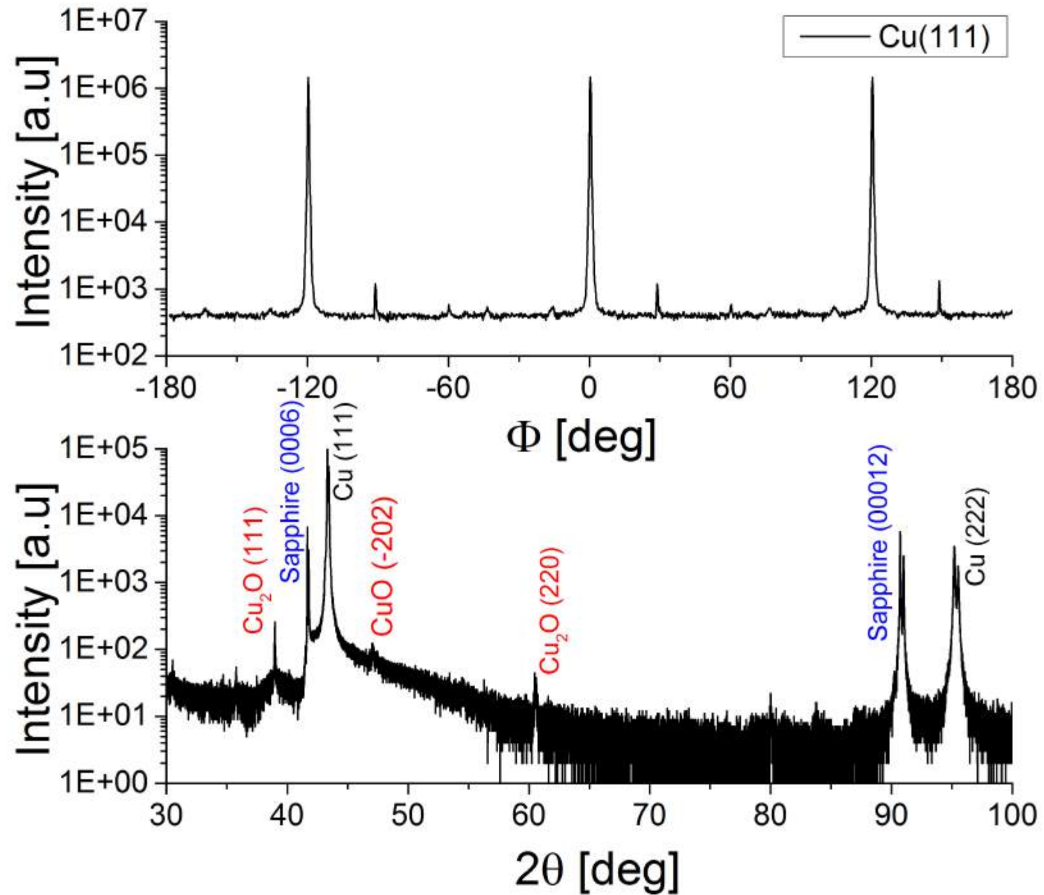

Figure 5.1: XRD Line scan and 2θ-scan of an untwinned epitaxial *Cu* layer, after Graphene growth.

The 2θ-scan indicates a large amount of $Cu\,(111)$ and $Al_2O_3\,(0006)$. The higher-order diffractions, $Cu\,(222)$ and $Al_2O_3\,(00012)$ are visible as well. Three small peaks ascribed to $Cu_2O\,(111)$, $CuO\left(\bar{2}02\right)$, and $Cu_2O\,(220)$ are also present. These have a low intensity, and are likely due to a thin layer of surface oxide.

5.1.2 Stability

The requirement for stability originates from Graphene growth research. Indeed, the resulting crystalline structure should be independent of the exact Graphene growth parameters. The optimal set of parameters is still being researched, therefore the quality of the epitaxial Cu layer should be reliable under varying temperature, pressure, and gas flow conditions.

5.2 Towards the State-of-the-Art: Oxygen treatments

In the previous chapter, Section 4.2 shows the results of different procedures intended to leave a Sapphire substrate Oxygen terminated. It is concluded that this termination is unstable, so a new objective is chosen, where the substrate would be Aluminum terminated (with hydroxylation). For the sake of completeness, the Cu crystalline structures, after annealing, of the four samples presented in Figure 4.4 are shown in Figure 5.2. Besides being irreproducible, these results are also significantly different from the monocrystalline structure that is the objective of this work. The remainder of this chapter will treat the thesis objective more in detail.

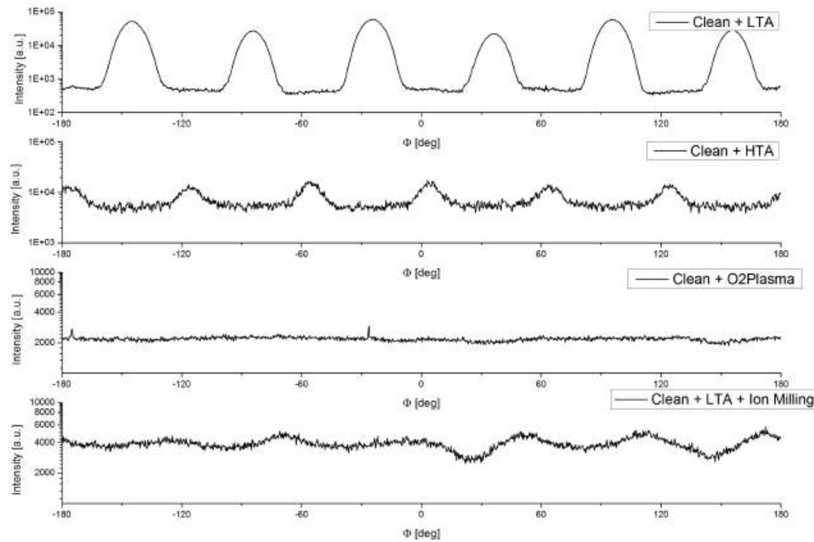

Figure 5.2: XRD Line scan of an epitaxial Cu layer, after Graphene growth, for different surface treatment procedures described in Chapter 3. The curves for the as-deposited structures are given in Figure 4.4.

5.3 Towards the thesis objective

The lack of reproducibility of the results produced on Oxygen treated substrates is problematic. To tackle this, different results are presented in Section 4.3 where the hydroxyl-Aluminum termination is used. These show encouraging reproducibility, and therefore, the present section deals with the structure these samples adopt when they are annealed. Figure 5.3 shows the crystalline structure, after anneal, of the different samples discussed in Section 4.3. The structure for samples that undergo Cu sputtering in a Nimbus tool (no twinning, exclusively OR-Ia or b) look significantly better than the ones where Cu is deposited in the Microscience tool (these show a significant degree of twinning). In both cases, the annealed $Cu(111)$ is epitaxial. Section 5.5.2 goes more in the detail of these differences. The lesson here is that a single OR-I as-deposited structure and an hydroxyl-Aluminum terminated Sapphire wafer are the keys to epitaxial Cu growth.

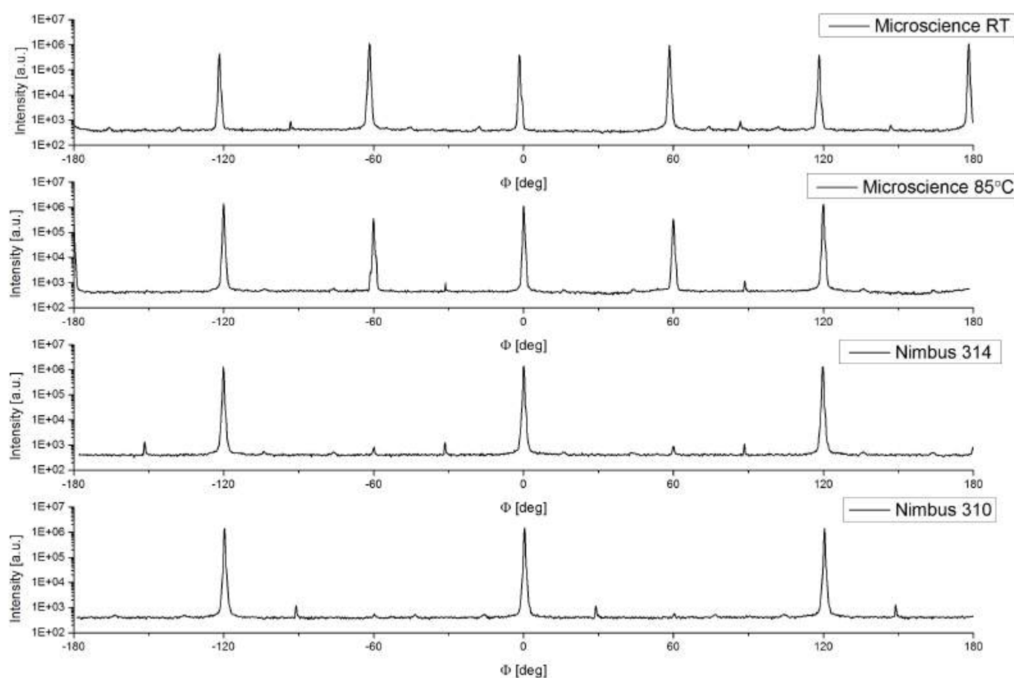

Figure 5.3: XRD Line scans of annealed samples that underwent Cu deposition in different systems under different conditions.

The relative OR content for the two Microscience samples can be calculated. In both cases, the ratio is 75% : 25% OR-Ia:OR-Ib. The following sections explore the effects of the parameters, intrinsic and extrinsic to the Graphene growth procedure, on the quality of epitaxial Cu.

5.4 Influence of intrinsic parameters

The three parameters that could have an influence on the quality of the Cu layer are the temperature, pressure and duration of the anneal step. The pressure is kept constant (90 $mbar$) and is not considered in the present discussion.

The temperature of the chamber during Graphene growth is measured with two thermocouples, positionned at the heating elements, and an InfraRed (IR) sensor aimed at the Cu/Al_2O_3 samples. The output values of these three sensors varies significantly. Only the readout from the IR sensor will be given here, it is considered to be the most reproducible. Nevertheless, the temperature information should be considered with care. Due to the doubts concerning the reliability of temperature information, the results presented in the following section is for constant growth temperature (between $1000°C$ and $1005°C$).

Other experiments were conducted, at different (measured) temperatures. The results do not indicate a correlation between the growth temperature and the crystalline structure of the epitaxial Cu layers.

5.4.1 Growth time

In order to investigate a possible influence of the growth duration, three identical samples undergo a growth cycle of respectively 10, 15, and 30 min. The crystallographic data of the resulting crystalline structures is presented in Figure 5.4. At first sight, these curves may look significantly different. It will be made clear, in the following discussion, that these results are, in fact, identical. For this, the reader may need to refer to Appendix B, where the crystallographic background of Sapphire is discussed.

The minor peaks in Figure 5.4 are due to this crystallographic background, and should, therefore, be identical. In the curves for 15 and 30 min growth time, these peaks can be perfectly superimposed, but for the 10 min curve, a 60° shift can be observed. This can be attributed to the position of the Primary Flat Location (PFL) on the Sapphire wafers. This is discussed in Appendix B, but does not represent an issue. The Sapphire peaks can be used to determine the exact OR for each sample (in this case, the 30 min curve consists of OR-Ia, the 10 and 15 min curves of OR-Ib). These two versions of OR-I are thermodynamically equivalent, and should therefore appear randomly in different experiments. These results indicate that this is the case.

The crystalline quality of the epitaxial Cu layer does not seem to be significantly affected by the growth time. This can be seen in the FWHM of the Cu peaks, in all three cases this is approximately 1°.

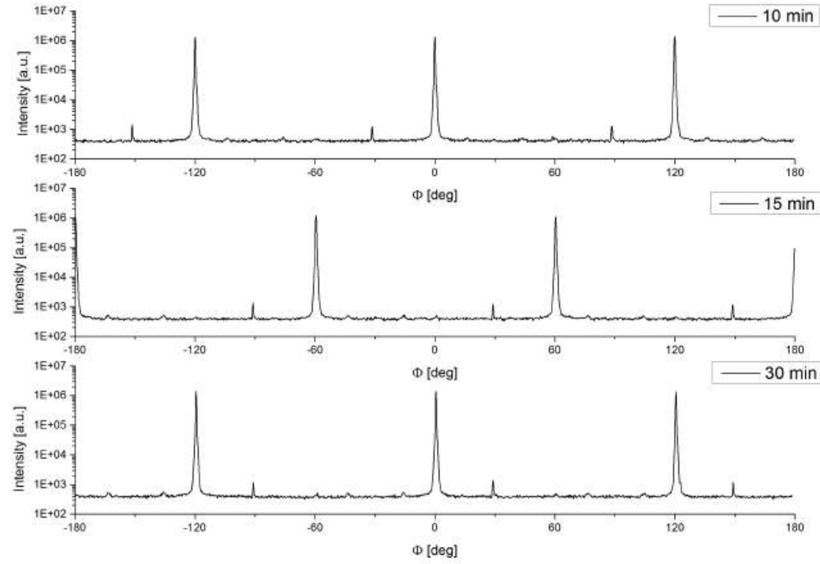

Figure 5.4: XRD Line scan of annealed epitaxial Cu layers for different Graphene growth durations.

5.4.2 Conclusion

In this section on the influence of the intrinsic (i.e. growth) parameters, the effect of the growth duration is investigated, and the possible effects of the temperature are shortly discussed. Concerning the latter, it is not possible to have a reliable figure for the exact growth temperature. Therefore it is not investigated.

The influence of the growth time is investigated, and it can be concluded that no significant correlation between the Graphene growth time and the crystalline structure can be found. This is an important parameter in the research for Graphene growth, and the fact that it does not influence the crystalline structure of the underlying template is good news.

These results hint at a possible grain growth mechanism[1]. When the sample is heated up, it will at some point reach an activation temperature for grain growth. As this temperature is exceeded, the Cu layer quickly adopts the most stable (either OR-Ia or OR-Ib) structure, and stays there. This would explain the lack of correlation between crystalline structure and growth time, and might explain why no correlation was found between the growth temperature and the crystalline structure.

This section further confirmed that the exact OR resulting from a Graphene growth procedure cannot be controlled. Since OR-Ia and OR-Ib are thermodynamically equivalent, this was expected from the beginning.

[1] Assuming that the phenomenon observed here is indeed grain growth, which is not certain.

5.5 Influence of extrinsic parameters

The parameters extrinsic to the Graphene growth procedure itself have an influence (on the Cu crystallinity) far exceeding that of the intrinsic parameters. These parameters are not treated individually. In the previous chapters, it is concluded that different sets of parameters can yield the same as-deposited Cu crystalline structure. In this chapter, this work is expanded, to include the results after growing Graphene on the templates.

This section treats two different aspects of the problem, being the preparation of the Sapphire substrates, and the conditions under which the Cu is deposited on the substrates.

5.5.1 Sapphire substrate preparation

In the previous chapters, the importance of the Sapphire substrate preparation is stressed on multiple occasions. This section follows the same trend. Three different procedures are investigated here, being: no substrate preparation at all, cleaning, and cleaning + LTA. The results, before growing Graphene on the Cu layer, are given in Figure 5.5.

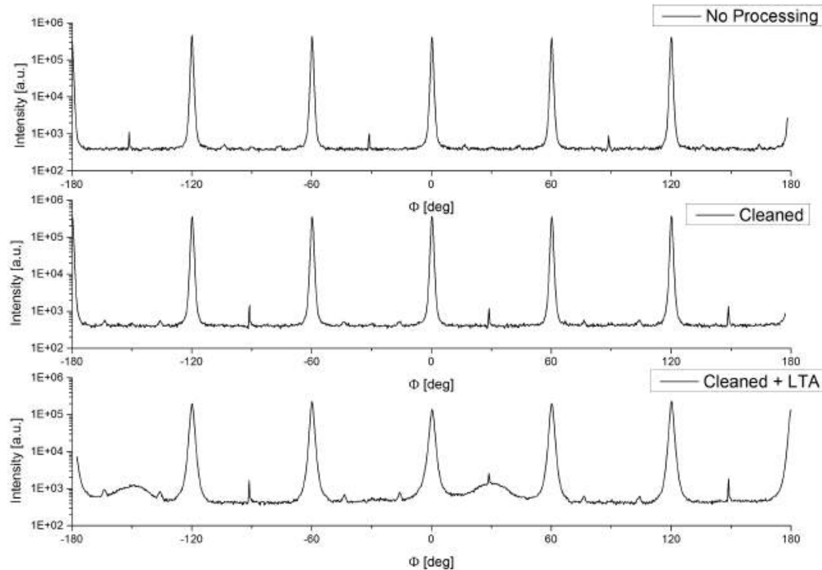

Figure 5.5: XRD Line scan of as-deposited Cu layers for different surface treatments.

Note that this section does not discuss the effect of a HTA. As seen in Figure 5.2, the HTA treatment has a disastrous effect on the crystalline quality of Cu layers.The crystalline structures for the sample that underwent no processing and the one that

was just cleaned appear to be identical. This should not be a surprise, the chemical termination of the Sapphire wafers is not thought to be influenced by the chemical clean, it is only used for removing the unwanted surface contamination. The results for the samples that underwent a LTA are not reproducible, and only one of these is shown in the Figure.

The results of the same samples after growing Graphene are shown in Figure 5.6. The sample that underwent no clean and the sample that was cleaned before the Cu deposition are identical. In fact the only difference is the OR, OR-Ia for the cleaned sample, and OR-Ib for the substrate that underwent no clean. The FWHM of the $Cu\,(111)$ peaks is again in the order of 1° for both curves. In both cases also, the dominant OR-peak is at least three orders of magnitude higher than all the other features of the curve.

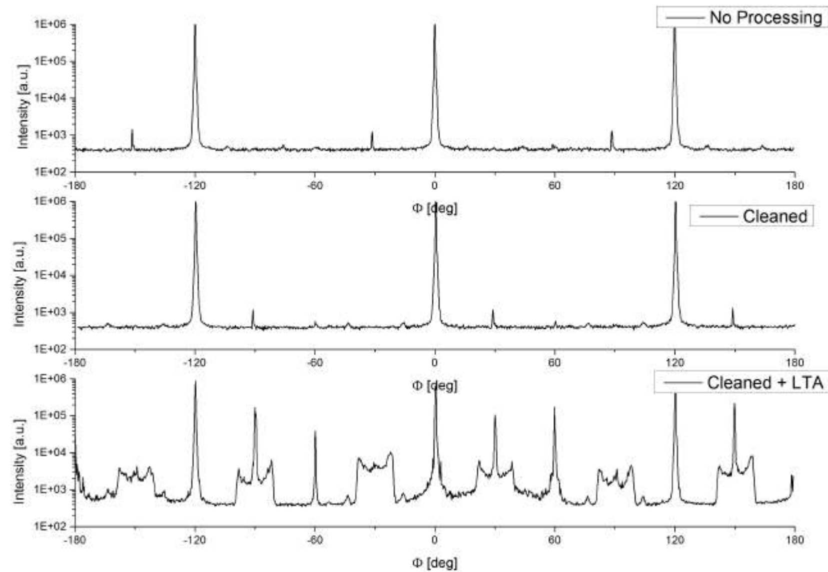

Figure 5.6: XRD Line scan of annealed epitaxial Cu layers for different surface treatments.

The result for the sample that received a clean and a LTA is significantly different. First, it does contain OR-I peaks, though the OR-Ia and OR-Ib peaks differ less than an order of magnitude. Second, there are features at the OR-II positions that cannot be explained. Such "triple-peak" structures correspond to a polycrystalline surface with many small grains with different in-plane orientations. These "triple-peak" structures are present in most samples where the LTA is applied. Additionally, the ratio between the external and the middle peaks varies to a very large extent, as well as the ratio between the different ORs.

Finally, something can be said about the position of the small Sapphire peaks in these crystallographic curves. Again, no correlation can be found between the processing steps and the specific form of OR-I that appears (i.e. the position of the Sapphire peak with respect tot the $Cu\,(111)$ peak).

Why cleaning?

In the results discussed above, the crystalline structure for cleaned and non-cleaned substrates is identical. The following question could be raised: why even clean the substrate? In an attempt to answer it, Figure 5.7 shows optical microscopy images of the two cases (both samples underwent exactly the same treatment apart from cleaning).

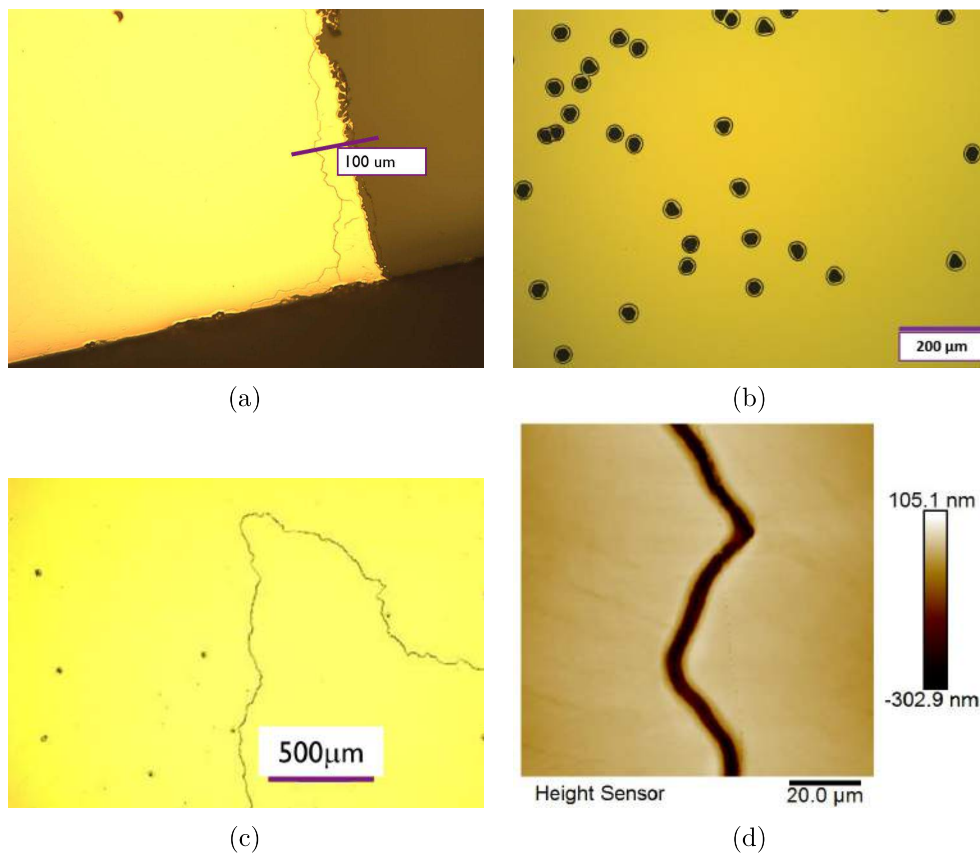

Figure 5.7: (a) Optical microscopy image of an annealed Cu layer, where the substrate was cleaned prior to Cu deposition. (b) Optical microscopy image of an annealed Cu layer, where the substrate was not cleaned prior to Cu deposition. (c) Giant grain. (d) AFM image of a grain boundary (Phase image in Fig. C.9).

On the cleaned substrates, see Figure 5.7a, the grain boundaries and defects are concentrated in an area close to the edge. On the right, next to the area where the

sticky tape (for fixation during Cu deposition) was applied, a sharp grain boundary can be seen. On the non-cleaned substrates, see Figure 5.7b, the black dots represent dewetting holes where the Cu layer does not cover its substrate. They are likely due to contaminants or defects at the interface.

The sharp contrast between the two pictures shown in Figure 5.7 makes a strong case for the necessity of cleaning a substrate. Every contaminant still present on the Sapphire surface can (and probably will) cause a defect of some sort. Some of these defects might not even be visible in an optical image.

Additionally, some results point out that samples that undergo no clean more often display twinning of the OR's after Graphene growth. This undesirable effect can be significantly decreased by the cleaning step, which is, again, a strong argument in favor of cleaning.

Figure 5.7c shows an optical microscopy image of a Grain boundary, on a cleaned sample. The grains shown there are very large. The image also contains black spots, characteristic of dewetting holes. This is an indication that the sample still contained a certain amount of surface contaminants or defects. This will then influence the giant grain growth behaviour of Cu, limiting the size of grains.

An AFM image of such a grain boundary is shown in Figure 5.7d. The depth of this GB (above 400 nm, i.e. the thickness of the Cu layer) indicates that it is due to the substrate itself, it shows dewetting between the grains. directly around the grain boundaries, the Cu nevertheless is flat in comparison. A very discrete feature of this image is the diagonal line (it is visible as a slight linear perturbation of the image), that coincides with a Graphene grain boundary. This is clearly visible in the AFM tapping phase image of the same area, given in Figure C.9.

The conclusion of this section on the necessity of cleaning is the following. While the epitaxial deposition of $Cu\,(111)$ on Sapphire is certainly possible on Sapphire when the substrate is not cleaned, the long-range order is compromised. The Cu grains will locally be epitaxial, but cannot grow together, which is translated in grain boundaries and twinning. Cleaning the substrate before Cu deposition removes most of the contaminants from the surface, which greatly improves the size of the grains. The increase in C and F contamination reported on Sapphire samples after cleaning is not found do negatively influence the crystalline quality of the Cu.

5.5.2 Cu deposition

Different Cu deposition (sputtering) setups are used, and different sets of sputtering parameters are investigated. The same crystalline structures for as-deposited Cu can be reached using the three different sputtering tools, given that the parameters are optimized. This may sound like a drawback, the need to optimize a procedure for the deposition setup could hint that not all aspects are understood yet. The three tools

impose different boundary conditions on the sputtering parameters (the Nimbus tools have no heatable wafer chuck, but the Microscience tool cannot sputter at high power; note that, as is stressed in Section 4.4, the power density is comparable), meaning that using the same deposition parameters is impossible anyway.

If it is possible to deposit Cu with the same crystalline structure using different tools, these samples should all adopt the same crystalline structure after a Graphene growth cycle. Figure 5.3 shows crystallography characteristics of Cu layers that are sputtered in the three deposition setups, corresponding to the samples discussed in Figure 4.6. The results, after Graphene growth, for the two Nimbus setups are identical, even though a slightly different pressure is used. The result for the Microscience tool looks worse at first sight, but is promising nevertheless. The OR ratio is 75% : 25% OR-Ia:OR-Ib. This is an indication of epitaxy, even though this is not yet satisfying. It should therefore be possible to optimize this result to yield wafer-sized single crystalline Cu layers. Additionally, since the Cu is deposited at $85°C$ or room temperature in this Microscience tool, and at room temperature in the Nimbus tools, this provides encouraging indications that there may be a lot of freedom in the exact parameters that one uses.

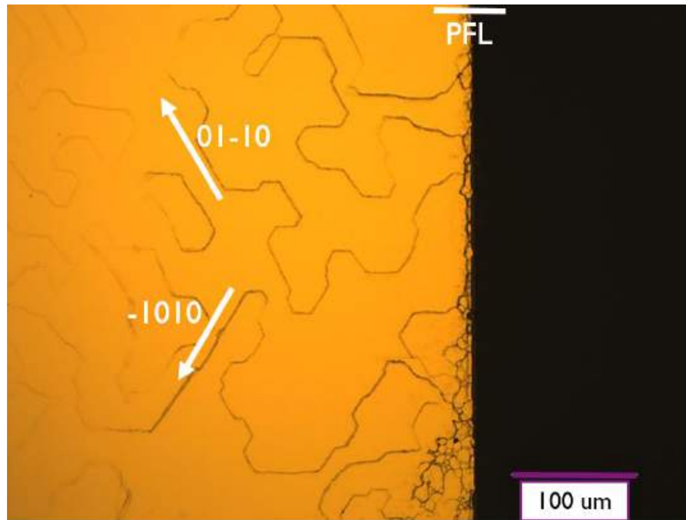

Figure 5.8: Optical microscopy image of an (annealed) Cu layer that is sputtered in the Microscience tool at $85°C$. The position of the PFL, and orientation of the grain boundaries of Cu in Sapphire coordinates are given in white.

An optical image of a sample sputtered in the Microscience tool at $85°C$ is shown in Figure 5.8. The surface shows grain boundaries which are visible mostly at the edge of the wafer. It can clearly be seen the the grain boundaries of the Cu grains strictly form 60° angles with eachother. Additionally, these GB are at the intersection of the buried $Cu\,(111)$ planes with the surface $Cu\,(111)$ plane. These GB are shallow, in the order of 30 nm. An AFM image of one of these is given in Figure C.10. The

orientation of the GB coincides with what would be expected from OR-Ia and OR-Ib grains where the grain boundaries consist of $Cu\,(111)$ planes.

5.5.3 Conclusion

The results reported in this section allow one to make two important conclusions. First of all, final and undeniable evidence is given that, unlike what is claimed in the majority of literature, an Oxygen treatment is not the way towards Cu epitaxy. All the data presented here (and in previous chapters of this thesis) indicate that a hydroxyl-Aluminum terminated surface is desirable. The proper pre-deposition treatment is cleaning in acid, to remove surface contaminants and particles.

Secondly, once the pre-deposition procedure has been optimized (i.e. the acid clean), there are several equivalent ways in which an epitaxial Cu layer can be created. The exact parameters of the sputtering deposition are setup-dependent. They have been shown to be easily customized to meet the requirements of the Nimbus tools (this is not true for the Microscience tool, a possible reason is the surface contamination due to exposure to non-cleanroom air before loading the samples). Furthermore, once a suitable as-deposited layer is produced, it can easily be annealed into an epitaxial Cu layer, at a broad range of Graphene growth parameters (see Section 5.4).

5.6 Graphene quality

The quality of Graphene grown on a Cu template is a complicated property to measure. Indeed, the proximity of Cu dopes the Graphene layer, which will significantly distort a Raman spectrum. If a reliable Raman spectrum has to be obtained, the Graphene should be transferred to a suitable substrate, e.g. SiO_2. Unfortunately, the adhesion between Cu and Graphene is relatively strong, making it difficult to transfer Graphene without introducing a lot of defects and contamination.

Additionally, transferring Graphene is outside of the scope of this thesis. Nevertheless, a few Graphene samples are characterized on a SiO_2 substrate, after transfer. On a Cu template, it is not possible to draw significant conclusions concerning the quality of Graphene.

5.6.1 STM

For assessing the quality of a Graphene layer with a high precision and a low spatial range, STM is used. Figure 5.9 shows the results of these STM investigations. In Figure 5.9a, a three dimensional image of a graphene layer, with corresponding Moiré patterns is shown. This Moiré pattern is due to a lattice mismatch between Graphene and the underlying template. The hexagonal symmetry of the features in that image shows Graphene on the surface.

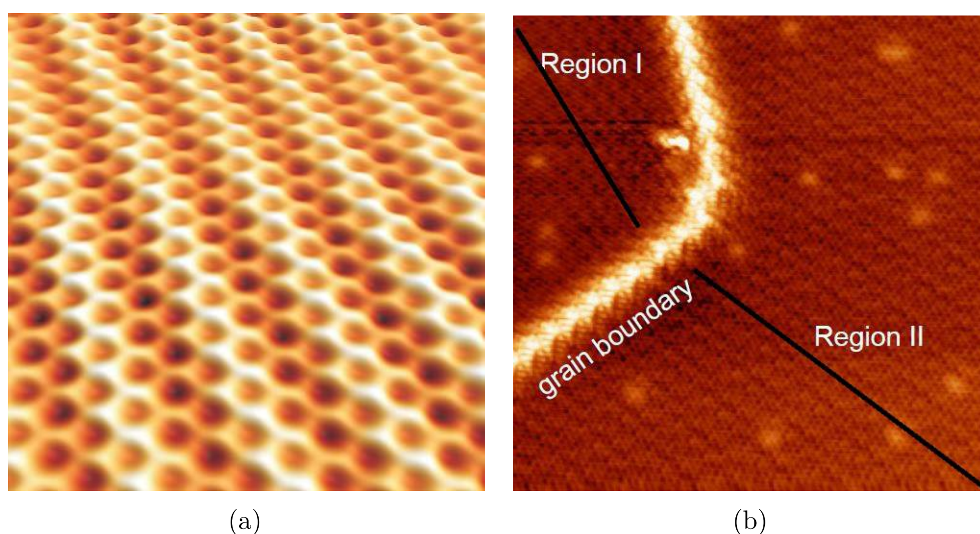

(a) (b)

Figure 5.9: (a) Three-Dimensional view of a Graphene layer grown on an epitaxial $Cu\,(111)$ template. (b) STM image of a grain boundary (bright line) between two Graphene crystals.

Figure 5.9b shows a slightly larger scale two dimensional image. In this case, the focus lies on the grain boundary (appears as a bright line), and the relationship between the two grains. The brighter dots are atomic defects in Graphene. The Moiré patterns are easily visible, and highlighted with the black lines. One can see that these black lines are not parallel, indicating the two Graphene grains do not have the same orientation.

If these Moiré patterns are not oriented in the same direction on both sides of a grain boundary, this means that the respective Graphene grains themselves are not oriented in the same direction. This is problematic. The need for monocrystalline substrates (such as, in this case, $Cu\,(111)$), is fuelled by the belief that Graphene grows along the orientation of a Cu grain. If two graphene grains on a monocrystalline Cu template grow with different orientations, this can only mean that the orientation of Graphene on Cu can hardly be controlled.

Two grains with a different orientation can never grow together, and the fact that two different orientations are present on a monocrystalline template is problematic. If it is not possible to control the orientation of Graphene flakes by using the template, it may be impossible to control this orientation at all.

5.6.2 Raman

Raman spectroscopy can be used to gather useful information on thin films such as Graphene. Specifically, it is possible to probe for defect densities, the amount of layers, doping, etc. by analyzing the electronic states of Graphene. It is therefore a very powerful tool.

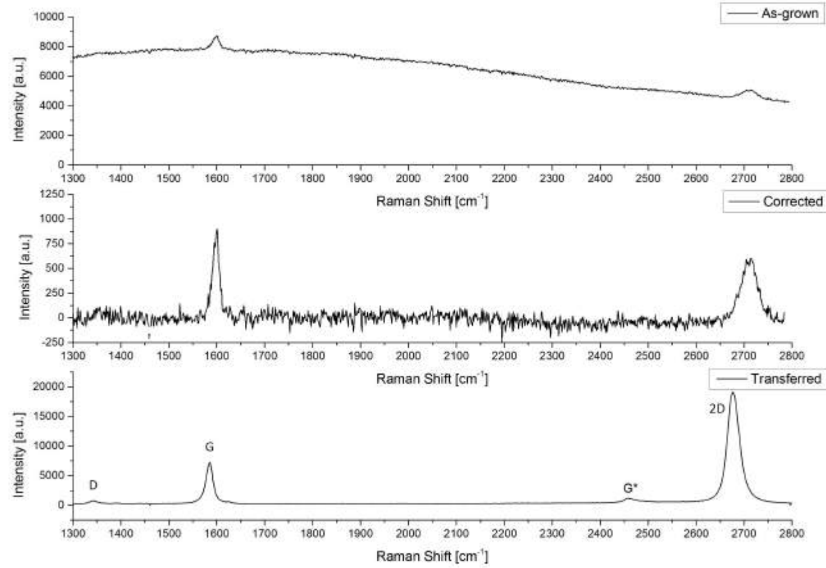

Figure 5.10: Raman Spectra of graphene, with and without a Cu background and transferred onto SiO_2.

On a Raman spectrum such as in Figure 5.10, Cu has a relatively dominating background, as compared to Graphene. It is therefore necessary to remove it by using numerical methods. A more reliable method is to simply transfer Graphene to SiO_2. One can now apply the concepts explained in Section A.7 on the curve of the transferred sample. The presence of the three features which are characteristic of Graphene (the D, G, G* and 2D peaks) indicates without doubt that there is Graphene on the sample.

The spectrum of the transferred sample shows a very small D peak, this indicates that the Graphene has few defects. Indeed, in the STM image of Figure 5.9b, a small quantity of defects are visible. The 2D/G ratio can be used to determine the amount of layers, if it is between 2...3 (in this case: 2.6), this corresponds to monolayer Graphene. The 2D peak additionally has $FWHM = 30\ cm^{-1}$, further confirming the presence of only one layer of Graphene. Finally, it can be seen that the 2D peak has shifted to the left (from 2700 cm^{-1} to 2680 cm^{-1}), which is a sign that Graphene is slightly p-doped. This is attributed to the PMMA used for transferring Graphene to its SiO_2 substrate.

When a Raman spectrum of different points on a sample is taken, it is possible to assess the uniformity of this sample. If all these Raman spectra look the same, one can conclude that the Graphene on Cu has the same properties at all these points, and is therefore uniform.

5.7 Issues

The results of this chapter show that it is possible to produce a wafer-scale epitaxial Cu grain, under a wide variety of conditions. Once this grain has been formed, it retains its crystalline structure regardless of the harsh Graphene growth steps it is subsequently exposed to. The problem of polycrystalline substrates potentially influencing the quality of Graphene can be considered solved. This only highlights the additionnal issues related to industrial production of Graphene. The present section gives a short, and in no way exhaustive, list of those problems.

5.7.1 Yield

Being able to produce a wafer-scale epitaxial Cu grain is one thing, designing a process that systematically results in the best possible crystalline quality is another. The acid cleaning procedure applied on the Sapphire wafers before the Cu deposition is an effective way to increase yield, but it is not infallible. Even in a cleanroom environment, the risks that a small particle would be adsorbed on the surface of the Al_2O_3 wafers is real. Even a very small particle can ruin the quality of a 500 nm thick layer of Cu.

The cleaning and Cu deposition procedure should be given extensive care. Also, the time spent between cleaning and Cu deposition should be short enough to minimize the risks of contamination of the surface. Ideally, the substrates should be loaded into the Cu deposition tool without being transported in a Teflon container. The tools used should be of the highest cleanliness class, as should the chemicals. The quality of the Sapphire surface is indeed of paramount importance for the success of this procedure.

5.7.2 Necessity of epitaxy

The STM image in Figure 5.9b shows the Moiré patterns of Graphene flakes on the Cu surface. Curiously, these patterns are not aligned in different flakes, meaning that they are not oriented in the same direction. The Cu template onto which this Graphene was grown was of the highest quality, yet two Graphene flakes with different orientations were grown.

In the literature study, the results of Rasool and Yu [67, 68] indicate that monocrystalline Graphene can grow on polycrystalline templates. If this is true, it may mean that Cu does not transfer its crystalline information to Graphene, and that the reverse could be true as well. This raises relevant questions on whether it is indeed necessary to use a monocrystalline template for Graphene growth.

5.7.3 Transfer

Even if the two previous issues (in the specific case of Cu) are solved, the issue of transfer remains. Growing Graphene is one thing, but in order to use it, it has to

be transferred to a dielectric substrate (like SiO_2). Unfortunately, Graphene has a fairly good adhesion to Cu, which makes it very hard to remove from its template without introducing defects and contamination.

To solve this issue, the best way would be to simply use another template material, which combines the advantages of Cu with a lower adhesion to Graphene. The combination of these properties is a rare thing. Platinum, for example, is seen as a worthy opponent for Cu when it comes to transfer of Graphene. A possible reason for this is that it is easy to saturate with Hydrogen at high temperatures. As the latter drops, the Hydrogen will diffuse towards the surface of Pt and create a "cushion" onto which the Graphene layer would be floating. This makes it easier to transfer. On the other hand, Pt is more expensive, has a higher C solubility (harder to make Graphene monolayers), and a higher melting point (harder to anneal into a wafer-scale crystal).

5.8 Conclusion

In this final chapter, the experimental results concerning the behaviour of Cu exposed to Graphene growth temperatures are given and analyzed. The first and most important lesson to be learned here is the following: given the right substrate preparation and Cu deposition parameters, a Cu layer forms a wafer-scale epitaxial grain when exposed to Graphene growth temperatures.

This is a significant improvement when compared to the state of the art. The results here clearly indicate a single OR, without twinning. Furthermore, the reason why the state of the art failed to get rid of twinning can be extrapolated: whereas everyone kept on trying to stabilize an Oxygen termination of Sapphire, the thermodynamically most stable hydroxylated Aluminum termination turned out to be the desired one.

Finally, the presence and quality of Graphene layers are investigated. STM and Raman experiments are conducted to prove that it is indeed Graphene on the templates. The quality of the latter is unfortunately not a guarantee for good Graphene. Additionally, the need for transferring Graphene to a dielectric substrate further compromises the quality of Graphene.

Notwithstanding the issues related to the Graphene itself, the goal of this thesis can be considered fulfilled. A significant improvement in the quality of $Cu\,(111)$ layers is made. Even if the path to Graphene growth on Cu templates turn out to be a dead end, the results of this thesis can be used on other materials. In that case, considering the importance of the chemical termination of the substrate may be an excellent starting point.

Chapter 6

Conclusion

$Cu\,(111)$ is an interesting template for Graphene growth, and can be deposited on Sapphire (0001). Until recently, it was unclear if the crystalline structure of the Cu template could be optimized to reach the desired quality. The template should consist of a single large grain of $Cu\,(111)$ with a flat surface.

Considerable research has been conducted to create this single crystalline template. A recurring and decisive element is the quality of the Sapphire substrate. There was no consensus on the optimal chemical termination, or concerning acceptable contamination levels. Both the Oxygen termination and the hydroxylated Aluminum termination of Sapphire have been proposed for Cu epitaxy, but until now no conclusive answer had been formulated.

The methods advocated in literature were thoroughly investigated. The professedly ideal Oxygen termination of Sapphire turned out to be highly unstable and sensitive to contamination. In fact, the breakthrough came from a procedure that was not intended to yield optimal results. Surprisingly, the hydroxyl-Aluminum termination of Sapphire proved to pave the way towards a suitable template.

In this conclusion, the objective of this work and the degree to which it is fulfilled will be discussed. The issues related to unsuccessful experiments will be summarized, and the procedure leading to an appropriate template will be examined.

6.1 Objective

The objective of this thesis was, as given in the introduction:

> to investigate the production of a template suitable for the growth of a large crystal of Graphene.

In terms of specifications, this objective involves epitaxial $Cu\,(111)$ deposition on monocrystalline $\alpha - Al_2O_3\,(0001)$, with wafer-scale single crystalline dimensions.

Two different pathways to Cu epitaxy were explored. The first one, Oxygen terminated Sapphire as a substrate, will be treated under the "State-of-the-Art". The second pathway, hydroxyl-Aluminum terminated Sapphire as a substrate, will be treated under the "Thesis objective".

6.1.1 State-of-the-Art

Of the many accounts in literature in favor of the Oxygen termination, the publication of Miller et al. [1] was the most promising. The authors propose a procedure yielding giant $Cu\,(111)$ grain growth on an Oxygen terminated Sapphire surface. The results reported here, unfortunately, were neither satisfactory nor reproducible in the case of the Oxygen termination. Several methods were applied to improve upon these poor results, like:

- Annealing in Oxygen at higher temperature, for longer periods
- Exposing the Sapphire substrate to Oxygen plasma
- Annealing in vacuum, *in situ* right before Cu deposition
- Ar ion milling, *in situ* right before Cu deposition
- Tuning Cu deposition parameters

Issues

While some of these procedures surely show promising results, they share a poignant feature in the shape of an unreliable outcome. This issue is ascribed to the stability of the Oxygen termination. Thermodynamically, even at high Oxygen partial pressures, the hydroxyl-Aluminum termination is favored over the Oxygen termination and its sensitivity to contamination. Here a major issue comes to light. The outcome of an industrial process cannot be left to chance. If the chemical termination of the Sapphire wafer has a decisive impact on the crystalline quality of Cu layers, it must be perfectly stable. Additionally, even when giant grains are present on O-terminated samples, it has not been possible to produce single crystalline Cu.

6.1.2 Thesis objective

The Aluminum termination of Sapphire is perfectly stable. When it is exposed to water (e.g. the humidity in ambient air), it will quickly become hydroxylated, and stay in this state under standard conditions. This is a significant advantage compared to the Oxygen termination. Additionally, experimental results indicate that giant epitaxial grain growth is strongly favored on Aluminum terminated Sapphire. Note that, upon exposure to air and Teflon containers, a significant degree of C and F contamination deposits on the surface. These have not been found to negatively influence the result.

Based on this stable Sapphire surface, the Cu deposition procedure could be optimized. The again surprising conclusion is the following: there exists a wide range of deposition parameter sets which allow the deposition of exactly the right crystalline quality of Cu. When it is annealed, this layer forms an epitaxial Cu structure consisting of wafer sized grains.

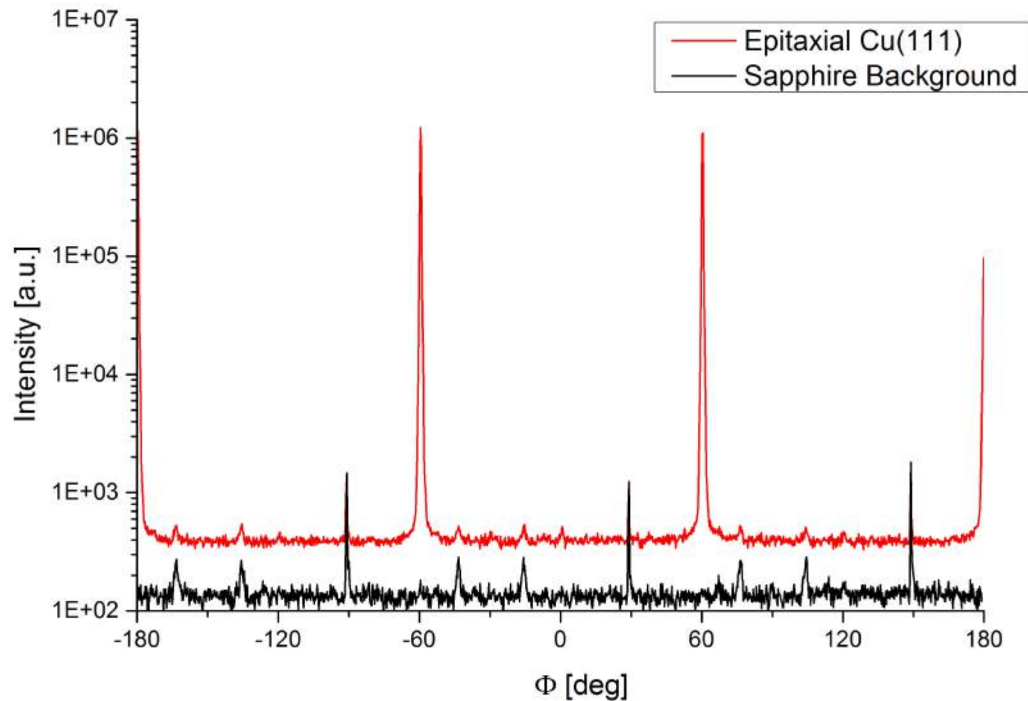

Figure 6.1: XRD Line scan of epitaxial Cu: OR-Ia.

Figure 6.1 shows an XRD Line scan of an annealed $Cu\,(111)$ layer. The Sapphire background is indicated. All the features not corresponding to OR-Ia in the Cu characteristic can be ascribed to Sapphire. This Cu film is perfectly single crystalline, and epitaxial. Figure 6.2 shows an optical microscopy image of an epitaxial Cu layer, at the edge of the substrate wafer. All the grain boundaries are concentrated near the edges of the substrate. This is a well-known phenomenon in the semiconductor industry.

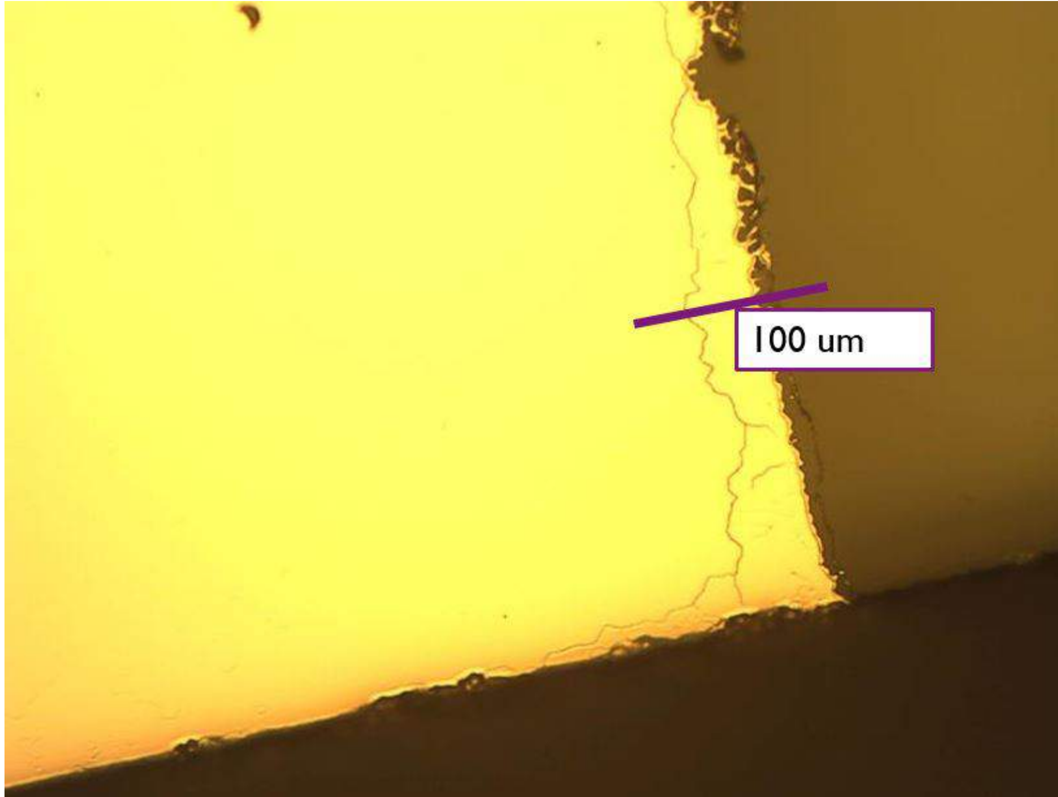

Figure 6.2: Optical microscopy image of the edge of an epitaxial Cu layer

Process flow

The full procedure resulting in giant $Cu\,(111)$ grain growth is given here:

1. **Clean** the Sapphire wafer in $3 * H_2SO_4 + 1 * H_3PO_4$[1] at $300°C$ for 20 min.
2. **Rinse** the cleaned wafer in UPW at room temperature for 3 min and blow-dry it in N_2.
3. **Sputter** Cu at room temperature for 173 sec in $4.5 * 10^{-3}$ $mbar$ of Ar with a power of 3000 W $(460\ V * 6.5\ A)$[2].
4. **Grow Graphene** under typical CVD conditions.

[1] 96% H_2SO_4 and H_3PO_4 is in *Honeywell Phosphoric Acid Etching Mixture* containing 73% H_3PO_4, 3.3% CH_3COOH, 20.6% H_2O, 3.1% HNO_3.

[2] These parameters can be modified to comply with the possibilities and limitations of different Cu deposition tools. Different possible deposition parameters are given in Appendix A.3.3.

6.2 Outlook

With the issue of polycrystalline substrates potentially influencing the crystalline quality of Graphene solved, the next problems in line can be tackled. The obvious next step is optimizing the Graphene growth parameters, so that a closed monolayer of Graphene with any desired dimensions can be grown. If there exists such a set of growth parameters, finding it will only be a matter of time.

When this Graphene layer is produced, it needs to be transferred to a dielectric substrate. Indeed, Cu metal is an excellent conductor, and would short circuit the electronic devices made out of Graphene. Optimizing Graphene transfer may be less straightforward than optimizing the growth parameters. Graphene tends to "stick" to the Cu template, making it tricky to peel it off without compromising the Graphene properties.

Another path for future research may be the growth of Graphene on different materials. Other metals show great promise as catalytic templates for Graphene growth. The knowledge concerning the epitaxial deposition of Cu collected in this thesis may be used to promote epitaxy in other metals. Platinum is an interesting contender for Cu. Graphene grown on Pt is much easier to transfer; however, there is not yet a clear pathway to Platinum epitaxy.

Ultimately, other sets of template materials and process parameters may provide the answer to the problem of Graphene growth. The possibilities are numerous, and only very few of those have already been explored.

Chapter 7

Publishable Summary

Epitaxial Metal Template Development for Graphene Growth

Bart Vermeulen[1], Steven Brems, Koen Schouteden, Stefan De Gendt, Chris Van Haesendonck, Marc Heyns
imec, Kapeldreef 75, 3001, Leuven, Belgium; KU Leuven, 3001, Leuven, Belgium

***Abstract*—The properties of Graphene make it a very promising material for future electronics applications. However, the production techniques still represent a major issue. Chemical Vapor Deposition using $Cu\,(111)\,/\alpha - Al_2O_3\,(0001)$ templates is seen as one of the best options for industrial scale Graphene growth. Here, the crystalline quality of the Cu templates is optimized by investigating the effect of chemically cleaning the Sapphire substrate. We report that Cu sputter-deposited on OH-Al-terminated Sapphire substrates and annealed at typical Graphene growth temperatures adopts a single crystalline structure. The resulting Cu layers are investigated using XRD and optical microscopy. They consist of twinning-free OR-I and the defects are concentrated in a small area close to the edge of the substrate.**

***Index Terms*—Graphene, Epitaxial $Cu\,(111)$, Sapphire, X-Ray Diffraction, Sputtering, Chemical Vapor Deposition.**

I. Introduction

GRAPHENE was discovered in 2004 by Geim and Novoselov [1] and has since then been the subject of intensive research. Specifically, the production methods for high-quality Graphene are of decisive importance for further scientific and industrial applications. Chemical Vapor Deposition is thought to fulfill many of the requirements related to both fields, and several groups have investigated the CVD growth of Graphene on catalytic templates made of Ni [2], Pt [3], Cu [4], Ge[5], and many more.

Cu is a particularly interesting CVD template. It has a low C solubility, which allows to limit the growth to a monolayer. The $Cu\,(111)$ plane has the same symmetry as Graphene, with only a small lattice mismatch. Furthermore, the low melting point and high atomic mobility of Cu promote recrystallisation and grain growth during typical Graphene CVD procedures. Miller et al. [6] report that "*polycrystalline as-deposited Cu on $\alpha - Al_2O_3\,(0001)$ can be transformed into $Cu\,(111)$ with cm sized grains*".

Due to the respective crystalline symmetries of the $Cu\,(111)$ and $\alpha - Al_2O_3\,(0001)$ surfaces, the Cu grains can have two different thermodynamically stable sets of Orientation Relationships (Eqs. 1 and 2, definitions from Refs. [6], [7], [8]):

$$OR-I \equiv (111)_{Cu} \parallel (0001)_{\alpha} \wedge [\bar{1}10]_{Cu} \parallel [10\bar{1}0]_{\alpha} \quad (1)$$

$$OR-II \equiv (111)_{Cu} \parallel (0001)_{\alpha} \wedge [\bar{1}10]_{Cu} \parallel [2\bar{1}\bar{1}0]_{\alpha} \quad (2)$$

The ORs described in these equations have a 60° rotational symmetry, whereas the $Cu\,(111)$ layer has a 120° rotational symmetry. Two different Cu grains can therefore have the same OR, and yet have a different orientation, resulting in a so-called twinned Cu crystal. The degree of twinning is an important measure of the quality of a Cu template for Graphene growth. The grain boundaries between twins can act as nucleation sites for Graphene [9], [10]. Additionally, Orofeo et al. [11] report a significant correlation between the crystalline structure of Cu templates and the domain structure of monolayer Graphene.

Besides the orientaion, the chemical termination of the Sapphire surface also is a major factor influencing the quality of $Cu\,(111)$ and Graphene. Three possibilities can be considered: The stoichiometric single Al termination is the most stable in vacuum [12], [13] but will quickly become hydroxylated even under low H_2O partial pressures [14], [15]. The single O termination, which is, according to literature, the most adequate for Cu deposition [7], likely due to Cu atoms having a predilection for threefold O sites [16]. Finally, there is the double Al termination.

Different surface treatments allow to try and influence the chemical termination of the Sapphire substrates. Chemical cleaning in solvents (Tetrachlorethylene, Acetone, Methanol) will reduce surface contamination, and leave it with the hydroxylated Al surface termination [17]. Acid based cleaning procedures may be more interesting, due to higher process temperatures and a broader selectivity. The dipping step in H_2O (to remove acid contamination), will ensure that the surface termination is the hydroxylated Al one [14], [15]. However, cleaning Sapphire in acid for too long may result in a damaged surface, Dwikusuma et al. [18] found that cleaning Sapphire in a $(3:1)$ H_2SO_4 : H_3PO_4 mixture at $300°C$ induces the formation of surface pits.

The chemical termination may, after cleaning, be modified by annealing the substrates in a specific atmosphere. Scheu et al. [17] found that an anneal in vacuum will result in an Al terminated surface, while annealing in O_2 will leave the Sapphire (temporarily) O terminated.

In this paper, we report the effect of a single chemical cleaning step resulting in a stable surface termination of the Sapphire substrate. Next, the quality of subsequently sputtered $Cu\,(111)$ films is investigated. Finally, the Graphene growth template is annealed under typical Graphene growth conditions to measure the effect on the sputtered Cu films.

[1]Corresponding author; E-mail: bart.vermeulen.310@gmail.com

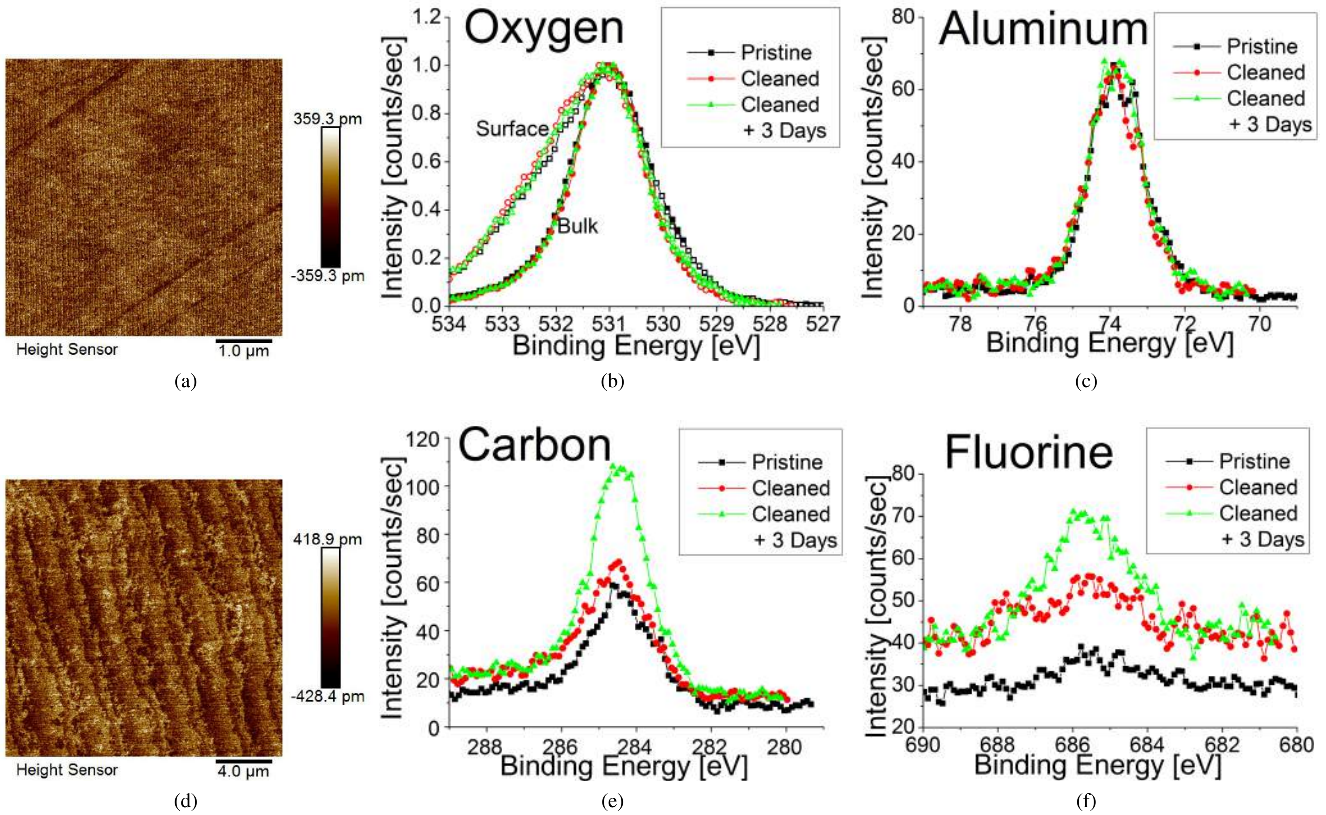

Fig. 1. (a), (d) AFM characterisation of the pristine (a) and cleaned (d) Sapphire surface. (b) Normalized Oxygen XPS bulk and surface spectra for pristine, cleaned and 3 days stored Sapphire wafers. (c) Aluminum, (e) Carbon, (f) Fluorine XPS surface spectra for pristine, cleaned and 3 days stored Sapphire wafers.

II. EXPERIMENTAL

Prior to Cu deposition, some Sapphire substrates are cleaned in three parts of 96% H_2SO_4 and one part of phosphoric acid etching mixture (*Honeywell*; 73% H_3PO_4; 3.3% CH_3COOH; 20.6% H_2O; 3.1% HNO_3) for 20 min at 300°C to remove all surface contaminants. They are rinsed in DIW at room temperature for 3 min and blow-dried in N_2.

The Cu layers (with a nominal thickness of 500 nm) are deposited in a Nimbus 310 sputtering setup with a base pressure of $3 * 10^{-3} mTorr$. The substrates are mounted on a Si carrier wafer and sputtered for 173 sec (21 passes under the target) at 4.5 $mTorr$ Ar-pressure and at room temperature, with a sputtering power of 3000 W (i.e. 460 V and 6.5 A) and a target-to-substrate distance of 50 mm.

The Cu/Al_2O_3 templates are then annealed in an Aixtron Black Magic 6 CVD system in 960 : 40 : 10 $sccm$ of $Ar : H_2 : CH_4$ at 90 $mbar$ and 1000°C, for 10 min.

The Sapphire substrates are investigated with AFM (Bruker AFM Dimension Edge in tapping mode) and XPS (ThermoInstruments Theta300, in angle resolved mode with the Al Kα wavelength). The Cu layers are investigated with optical microscopy and XRD (PANalytical X'pert MRD, Cu Kα wavelength for Bragg-Brentano measurements). The latter technique will prove very useful in determining the degree of twinning of different epitaxial Cu layers. Graphene monolayers are characterised as-grown by STM (Omicron STM at liquid N_2 and He temperatures in UHV) and after transfer by Raman (Horiba Labram HR with $\lambda = 532$ nm) spectroscopy.

III. RESULTS AND DISCUSSION

A. Pristine Sapphire

The original state of $\alpha - Al_2O_3\,(0001)$ is taken as the reference for assessing the effect of the chemical cleaning procedure. The substrate wafers have an atomic purity above 99.995% and are highly monocrystalline. The miscut angle of the c-plane surface is below 0.3°. The RMS roughness is measured with AFM to be 0.11 nm. Figure 1a shows flat terraces with straight atomic steps (height < 0.25 nm) and diagonal stripes ascribed to polishing.

The surface composition is probed with XPS. Low levels of C and F contamination are detected, likely due to exposure to air, and containers made of Teflon. The Oxygen signal is analyzed in more detail. Figure 1b shows the normalized spectrum at two different exit angles. The bulk signal exhibits a peak at $E_B = 531$ eV, typical for $Al - O$ bonds [15]. The surface signal shows an additional feature at $E_B = 532$ eV, attributed to $O-H$ bonds. This indicates the presence of hydroxyl groups on the surface. The pristine $Al_2O_3\,(0001)$ surface termination is determined to be the hydroxylated Al-termination.

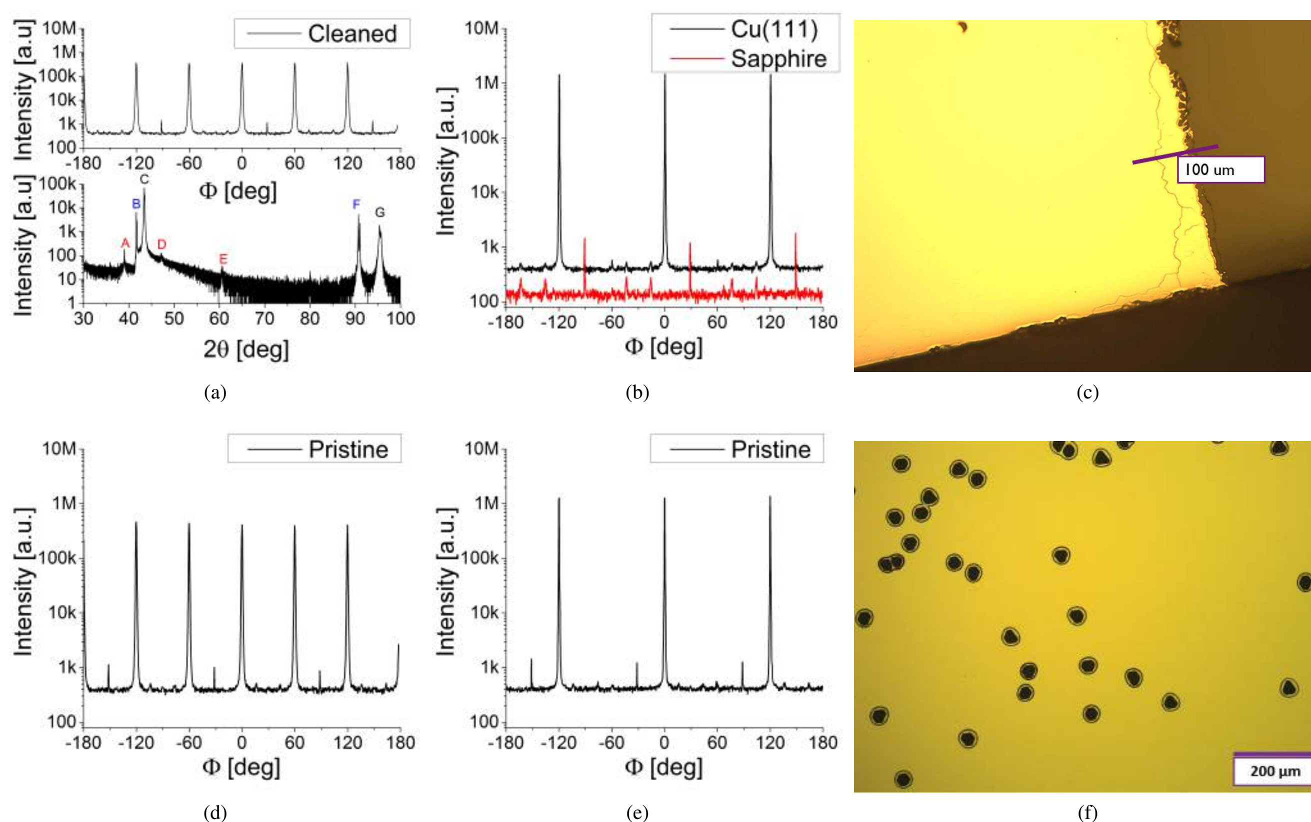

(a) (b) (c)

(d) (e) (f)

Fig. 2. (a) XRD Line scan of as-deposited $Cu\,(111)$ on cleaned Sapphire, (b) After Graphene growth, (c) Optical microscopy after Graphene growth, (d), XRD Line scan of as-deposited $Cu\,(111)$ on pristine Sapphire, (e) After Graphene growth, (f) Optical microscopy after Graphene growth.

B. Cleaned Sapphire

The chemical clean increases the RMS surface roughness of Sapphire to $0.12\ nm$. As can be seen in Figure 1d, the terrace-and-step structure at the surface is mildly damaged.
The chemical termination of cleaned Sapphire is similar to the termination of pristine Sapphire. Figure 1b shows the comparison of normalized bulk and surface signals for a pristine surface, a cleaned surface, and after 72 hrs of ageing in a Teflon container. The bulk and surface signals in all three cases are respectively identical to within 1%. The hydroxylation of the surface is not influenced by the chemical cleaning procedure. This is likely due to the DIW rinsing step which re-hydroxylates the surface.
The absolute Aluminum spectra for pristine, cleaned and 72 hrs aged Sapphire are shown in Figure 1c. No significant variation of the Al content of the surface can be detected after the chemical clean, nor after 72 hrs of ageing. The hydroxylated Al-termination is not compromised by the cleaning procedure.
The absolute Carbon and Fluorine spectra are shown in Figures 1e and 1f respectively. The C contamination after cleaning increases with $22\% \pm 1\%$, and again by $55\% \pm 1\%$ (with respect to the cleaned state) after 72 hrs of storage. The F figures are respectively $48\% \pm 1\%$ after cleaning, and $19\% \pm 1\%$ after storage. In both cases, the F contamination stays close to the measurement threshold.
The fact that the C and F levels increase during the storage period is to be expected. The substrates are in contact with air, and the Teflon containers, which makes these contaminants inevitable. The contamination can be minimized by depositing Cu layers right after the cleaning step, without storing the substrates in Teflon in between these procedures.

C. As-deposited Cu

The as-deposited Cu layers on cleaned Sapphire show a large $Cu\,(111)$ content in the $\theta - 2\theta$ scan, see Figure 2a ($Cu\,(111)$ is indicated with C and $Cu\,(222)$ is indicated with G). Additional features in the characteristic are attributed to the Sapphire substrate ($Al_2O_3\,(0006)$: B and $Al_2O_3\,(00012)$: F) and a thin layer of Cu oxides at the surface ($Cu_2O\,(111)$: A, $CuO\,(\bar{2}02)$: D, and $Cu_2O\,(220)$: E). Oxidation of the Cu surface is inevitable under ambient conditions. A line scan at $2\theta = 43.4°$ and at a tilt angle of $\Psi = 70.5°$ (to probe buried $Cu\{111\}$ planes) reveals OR-I with evenly distributed twinning.
The OR content of the Cu layers deposited on pristine Sapphire is also shown in Figure 2d. The $\theta - 2\theta$ scan is identical to the cleaned Sapphire case (see Figure 2a) and reveals a $Cu\,(111)$ structure with a thin film of surface Cu oxides. The line scan shows evenly twinned OR-I, like on the cleaned substrates.

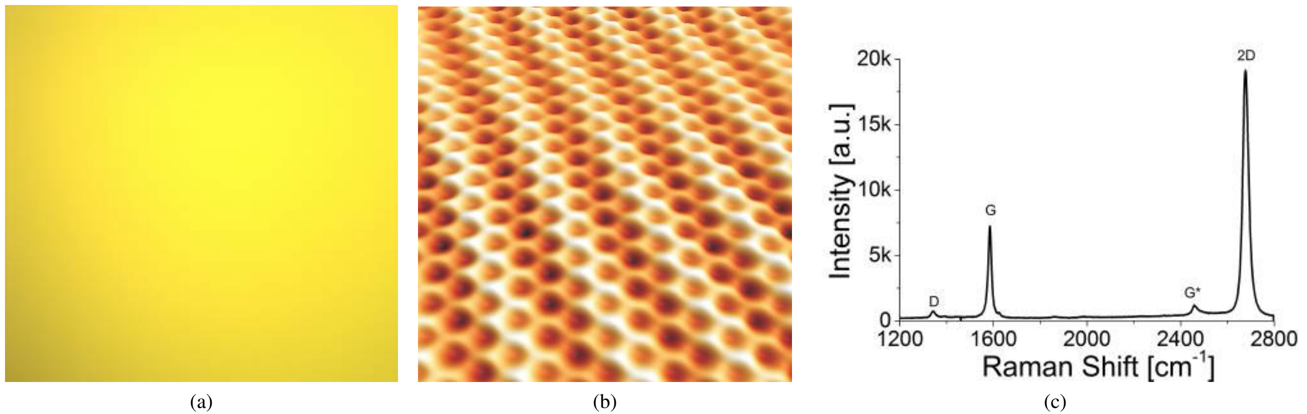

(a) (b) (c)

Fig. 3. (a) Optical microscopy of an annealed Cu layer on a cleaned Sapphire substrate. (b) STM image of Graphene grown on $Cu\,(111)$. (c) Raman spectrum of Graphene grown on $Cu\,(111)$, after transfer onto SiO_2.

D. Annealed Cu

After anneal, the Cu layers on cleaned substrates form perfectly epitaxial $Cu\,(111)$ films. The $\theta - 2\theta$ scan is identical to the as-deposited Cu case (see Figure 2a) and is therefore not shown. It shows the same large $Cu\,(111)$ content, along with the expected substrate- and oxide-signals ($Al_2O_3\,(0006)$, $Al_2O_3\,(00012)$, $Cu_2O\,(111)$, $CuO\,(\bar{2}02)$, and $Cu_2O\,(220)$). The line scan of the annealed Cu crystal shows three sharp ($FWHM \simeq 1°$) peaks with 120° periodicity, corresponding to single crystalline untwinned OR-I $Cu\,(111)$. The minor peaks visible in the line scan correspond to the Sapphire background, displayed under the Cu characteristic in the figure.

Optical microscopy investigation of an annealed Cu layer deposited on cleaned samples is shown in Figure 2c. The image allows to determine that all the grain boundaries are concentrated near the edges of the Cu layer. A single dewetting hole is visible at the top of the image, due to a defect, a particle or contamination. Microscopy images of the bulk show no visible contrast, see Figure 3a. Combined with the data from XRD this is an indication of an untwinned $Cu\,(111)$ layer at the surface, with grain-boundary-free dimensions limited only by the size of the substrate wafer.

The crystallographic characteristics of an annealed Cu layer deposited on a pristine Sapphire wafer are shown in Figure 2e. The line scan shows perfectly epitaxial $Cu\,(111)$ without twinning of the OR. The XRD peaks are sharp ($FWHM \simeq 1°$), and the minor peaks due to the substrate are visible as well.

The necessity of cleaning is illustrated with Figure 2f. The surface is covered in dewetting holes with hexagonal edges. These edges are parallel two by two with angles of 120°, corresponding to the symmetry of the $Cu\,(111)$ surface.

The epitaxial relationship between the Sapphire substrate and the annealed $Cu\,(111)$ layer is not influenced by the cleaning procedure. The OR content is not modified. The main difference is the large amount of contaminants present on the surface when no clean is applied, causing dewetting holes in the Cu layer.

E. Graphene growth

Graphene flakes are grown on the Cu templates after the annealing ramp-up. Figure 3b shows a three dimensional image of the Graphene surface. The Moiré patterns are due to the lattice mismatch between $Cu\,(111)$ and Graphene. Figure 3c shows the Raman spectrum of a Graphene flake after transfer. The D peak is low, indicating a low defect density and low doping levels. The I_{2D}/I_G ratio is 2.6 and indicative of monolayer Graphene. The 2D peak has shifted to lower values of the Raman shift (from 2700 cm^{-1} to 2680 cm^{-1}), corresponding to slightly p-doped Graphene. Additionally, the 2D $FWHM = 30\ cm^{-1}$, indicating monolayer Graphene. The doping is caused by polymer residues from the transfer procedure and from the interaction with the dielectric SiO_2 substrate.

IV. Conclusion

We report a process flow for producing perfectly epitaxial untwinned $Cu\,(111)\,/Al_2O_3\,(0001)$ templates for Graphene growth:

1) **Clean** the Sapphire wafer in $3 * H_2SO_4 + 1 * H_3PO_4$[1]at $300°C$ for 20 min.
2) **Rinse** the cleaned wafer in UPW at room temperature for 3 min and blow-dry it in N_2.
3) **Sputter** Cu at room temperature for 173 sec in $4.5 * 10^{-3}$ $mbar$ of Ar with a power of 3000 W (460 $V *$ 6.5 A).
4) **Grow Graphene** under typical CVD conditions.

The chemical cleaning procedure is used to remove unwanted surface contaminants without modifying the chemical termination of the surface. The cleaning procedure reduces surface contamination, that would otherwise induce defects in the deposited Cu layers. C and F contamination on the Sapphire surface is not found to negatively influence the crystalline quality of subsequently deposited Cu layers. The annealed $Cu\,(111)$ is single crystalline and free of twinning. The only

[1]96% H_2SO_4 and H_3PO_4 is in *Honeywell Phosphoric Acid Etching Mixture* containing 73% H_3PO_4, 3.3% CH_3COOH, 20.6% H_2O, 3.1% HNO_3.

detectable grain boundaries are localized near the Cu edges. Graphene grown on these epitaxial Cu templates is of high quality. It consists of monolayers with very few defects, and is p-doped after transfer due to PMMA.

REFERENCES

[1] K.S. Novoselov, A.K. Geim, S.V. Morozov, D. Jiang, Y. Zhang, S.V. Dubonos, I.V. Grigorieva, and A.A. Firsov. Electric field effect in atomically thin Carbon films. *Science*, 306(5696):666–669, 2004.

[2] J. Lahiri, T. Miller, L. Adamska, I.I. Oleynik, and M. Batzill. Graphene growth on Ni(111) by transformation of a surface carbide. *Nano Letters*, 11(2):518–522, 2010.

[3] P. Sutter, J.T. Sadowski, and E. Sutter. Graphene on Pt(111): Growth and substrate interaction. *Physical Review B*, 80(24):245411, 2009.

[4] L. Gao, J.R. Guest, and N.P. Guisinger. Epitaxial Graphene on Cu(111). *Nano Letters*, 10(9):3512–3516, 2010.

[5] J.H. Lee, E.K. Lee, W.J. Joo, Y. Jang, B.S. Kim, J.Y. Lim, S.H. Choi, S.J. Ahn, J.R. Ahn, M.H. Park, et al. Wafer-scale growth of single-crystal monolayer Graphene on reusable Hydrogen-terminated Germanium. *Science*, 344(6181):286–289, 2014.

[6] D.L. Miller, M.W. Keller, J.M. Shaw, K.P. Rice, R.R. Keller, and K.M. Diederichsen. Giant secondary grain growth in Cu films on Sapphire. *AIP Advances*, 3(8), 2013.

[7] S.H. Oh, C. Scheu, T. Wagner, E. Tchernychova, and M. Rühle. Epitaxy and bonding of Cu films on Oxygen-terminated α-Al_2O_3(0001) surfaces. *Acta Materialia*, 54(10):2685–2696, 2006.

[8] S. Curiotto, H. Chien, H. Meltzman, P. Wynblatt, G.S. Rohrer, W.D. Kaplan, and D. Chatain. Orientation relationships of Copper crystals on c-plane Sapphire. *Acta Materialia*, 59(13):5320–5331, 2011.

[9] B. Hu, H. Ago, Y. Ito, K. Kawahara, M. Tsuji, E. Magome, K. Sumitani, N. Mizuta, K. Ikeda, and S. Mizuno. Epitaxial growth of large-area single-layer Graphene over Cu(111)/Sapphire by atmospheric pressure CVD. *Carbon*, 50(1):57–65, 2012.

[10] W. Liu, H. Li, C. Xu, Y. Khatami, and K. Banerjee. Synthesis of high-quality monolayer and bilayer Graphene on Copper using Chemical Vapor Deposition. *Carbon*, 49(13):4122–4130, 2011.

[11] C.M. Orofeo, H. Hibino, K. Kawahara, Y. Ogawa, M. Tsuji, K. Ikeda, S. Mizuno, and H. Ago. Influence of Cu metal on the domain structure and carrier mobility in single-layer Graphene. *Carbon*, 50(6):2189–2196, 2012.

[12] E.A. Soares, M.A. Van Hove, C.F. Walters, and K.F. McCarty. Structure of the α-Al_2O_3(0001) surface from low-energy electron diffraction: Al termination and evidence for anomalously large thermal vibrations. *Physical Review B*, 65(19):195405, 2002.

[13] I. Batyrev, A. Alavi, and M.W. Finnis. Ab initio calculations on the Al_2O_3(0001) surface. *Faraday Discussions*, 114:33–43, 1999.

[14] X.G. Wang, A. Chaka, and M. Scheffler. Effect of the environment on α-Al_2O_3(0001) surface structures. *Physical Review Letters*, 84(16):3650, 2000.

[15] J.A. Kelber, C. Niu, K. Shepherd, D.R. Jennison, and A. Bogicevic. Copper wetting of α-Al_2O_3(0001): Theory and experiment. *Surface Science*, 446(1):76–88, 2000.

[16] A. Hashibon, C. Elsässer, and M. Rühle. Structure at abrupt Copper–Alumina interfaces: An ab initio study. *Acta Materialia*, 53(20):5323–5332, 2005.

[17] C. Scheu, M. Gao, S.H. Oh, G. Dehm, S. Klein, A.P. Tomsia, and M. Rühle. Bonding at Copper–Alumina interfaces established by different surface treatments: a critical review. *Journal of Materials Science*, 41(16):5161–5168, 2006.

[18] F. Dwikusuma, D. Saulys, and T.F. Kuech. Study on Sapphire surface preparation for III-nitride heteroepitaxial growth by chemical treatments. *Journal of The Electrochemical Society*, 149(11):G603–G608, 2002.

Appendices

Appendix A

Methods and Materials

In this appendix, the relevant properties of Sapphire, Cu and Graphene are first discussed. In a next section, a short overview of the most important process techniques used in this thesis is given. Additionally, the ways in which these steps are combined in a process flow is also discussed. Finally, in the main part of this appendix, the different characterisation techniques that are used throughout this thesis are described. The effect of every step of the procedures undertaken in the deposition of epitaxial Cu has to be thoroughly analyzed, and so one can note that the techniques discussed in this chapter can be classified into three categories.

The first one concerns the characterisation of the Sapphire surface. Atomic Force Microscopy is used to provide information about the topography of this surface. Depending on the mode of operation, additional information can be derived, concerning its composition as well (it can be used to probe for Graphene layers). This may be used in a later step for analyzing the integrity of Graphene layers. X-Ray Photoelectron Spectroscopy provides information about chemical bonds at the surface and inside a material. The chemical composition of this material can be derived from this information.

The second category is introduced for the purpose of probing the crystalline structure of the different materials involved. X-Ray Diffraction is used for this purpose and allows to both verify the crystalline orientation of the top surface of Sapphire and Cu, as well as analyze the in-plane orientation of the different Cu grains that were deposited. As appears throughout this thesis, this turns out to be a critical parameter for the quality of the template, and therefore XRD is by far the most used characterisation technique.

Lastly, since the purpose of this template is to provide wafer scale monocrystalline Graphene, the quality of this layer has to be probed as well. For that purpose, two additional techniques are used. Raman Spectroscopy provides information on the integrity of the Graphene layers, as well as the amount of layers, and possible doping effects. Finally Scanning Tunneling Microscopy can be used for the same purpose, with the difference here that a small surface can be imaged with atomic resolution.

A.1 Materials

In this section, the properties of the important materials used in this thesis are discussed. The focus lies on the crystalline properties, as these are the most relevant to a discussion on epitaxy.

A.1.1 Sapphire

The starting point of all experimental work conducted in this thesis is a two inch monocrystalline Sapphire wafer. The properties discussed here are valid for the α phase of Sapphire. Crystalline materials can, depending on external conditions such as temperature, adopt different spacial distributions of the atoms. A discussion of the different phases of Sapphire falls outside of the scope of this thesis.

General properties

The main properties of Sapphire as a macroscopic material are given in Table A.1. Macroscopically, Sapphire is a relatively hard, transparant dielectric material. Note that the properties which can be anisotropic indeed show a significant spread.

Table A.1: Physical properties of Sapphire [12].

Property	Value
Density	3.97..3.99 g/cm^3
Mohs Hardness	9
Tensile Strength	275..400 MPa
Young's Modulus	322..494 MPa
Melting Point	2323 K
Coefficient of Thermal Expansion (Room Temperature)	5.0..6.6 $*10^{-6}K^{-1}$
Thermal Conductivity (RT)	30.3..32.5 W/mK
Resistivity (RT)	5..29 $*10^{18}\Omega cm$
Relative Dielectric Constant (RT)	9.35..11.53
Dielectric Strength	48 $*10^6V/m$

Unit Cell

The crystalline structure of Sapphire can be described as a Hexagonal Close Packed (HCP) stacking of Oxygen anions, where two thirds of the octahedral interstices are occupied by an Aluminum cation (see Fig. A.1a). The corners of the unit cell are defined by the empty sites of the cation sublattice (See Fig. A.1b).

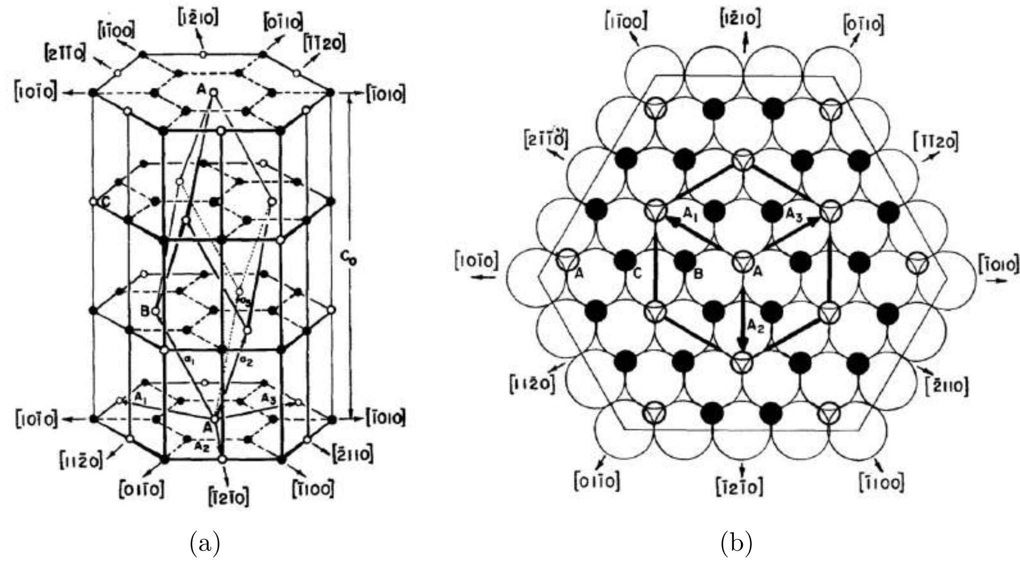

(a) (b)

Figure A.1: (a) Spacial distribution of the Aluminum ions in the rhombohedral Unit Cell. (b) Representation of the Sapphire basal plane (c-plane). Large circles are Oxygen ions, small filled circles Aluminum, and small empty circles the empty sites used to define the Unit cell. From Kronberg et al. [7].

The lattice parameters of Sapphire are $a_0 = 0.47589 * 10^{-9}m$ (indicated as $A_{1,2,3}$ in Fig. A.1b) and $c_0 = 1.2991 * 10^{-9}m$.

The (0001) surface

The (0001) crystalline plane of Sapphire (also called basal plane or c-plane) is used as a substrate for the epitaxy of $Cu\,(111)$. It has twofold symmetry, unlike what Fig. A.1b suggests. That figure shows only one layer of Aluminum cations, when the second layer is taken into account, the symmetry is twofold. As was explained in Section 2.1.2, a (0001)-surface can have three different terminations.

A.1.2 *Cu*

Cu is the metal that was chosen as a template for the growth of Graphene. There are three reasons for this choice. First, it is a reasonable Graphene growth catalyst. Second, its (111)-surface has the right (threefold) symmetry and lattice parameter for exchanging crystalline information with both graphene and $\alpha - Al_2O_3\,(0001)$. Finally, the Carbon solubility is exceptionally low, which makes it a good candidate for controlled monolayer growth.

General properties

Cu is a Face Centered Cubic (FCC) metal with a very good electrical and thermal conductivity. These two properties make it especially interesting for (micro-)

electronics applications, where it is widely used. Its main properties are listed in Table A.2.

Table A.2: Physical properties of Cu [13].

Density	8.93 g/cm^3
Mohs Hardness	3
Tensile Strength	209..344 MPa
Young's Modulus	110..128 GPa
Melting Point	1356 K (1083°C)
Coefficient of Thermal Expansion (Room Temperature)	5.0..6.6 $*10^{-6}K^{-1}$
Thermal Conductivity (RT)	401 W/mK
Resistivity (RT)	16.73 $*10^{-9}\Omega m$

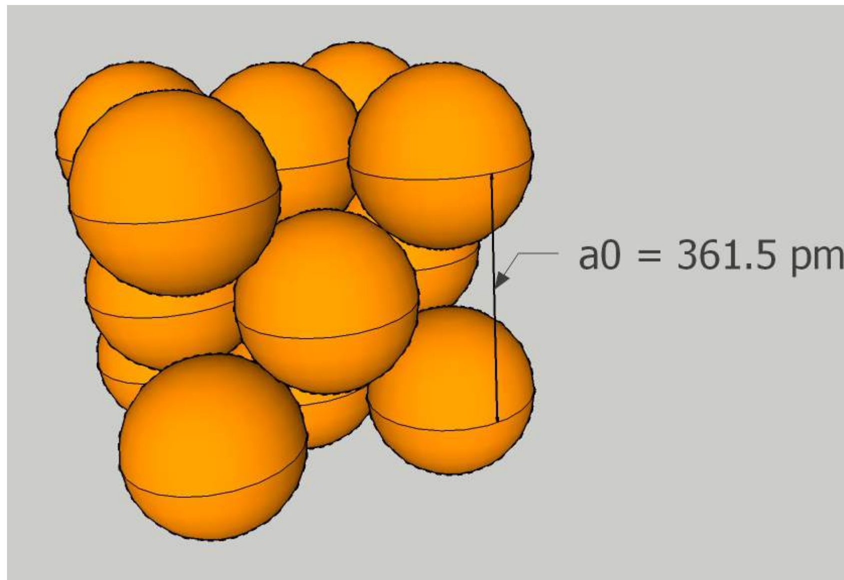

Figure A.2: The Unit Cell of an FCC metal, in this case Cu. The lattice constant $a_0 = 361.5\ pm$ is indicated.

Unit Cell

The Unit Cell of an FCC metal is shown in Figure A.2. The lattice constant of Cu is equal to: $a_0 = 0.3615nm$.

The (111) plane

The crystalline plane chosen as a template for the growth of Graphene must fulfill the three requirements cited in the beginning of this section. The (111)-plane does just that. As shown in Figure A.3, the first layer of Cu atoms has sixfold symmetry, but when the second layer is taken into account, the symmetry is threefold, just like Graphene.

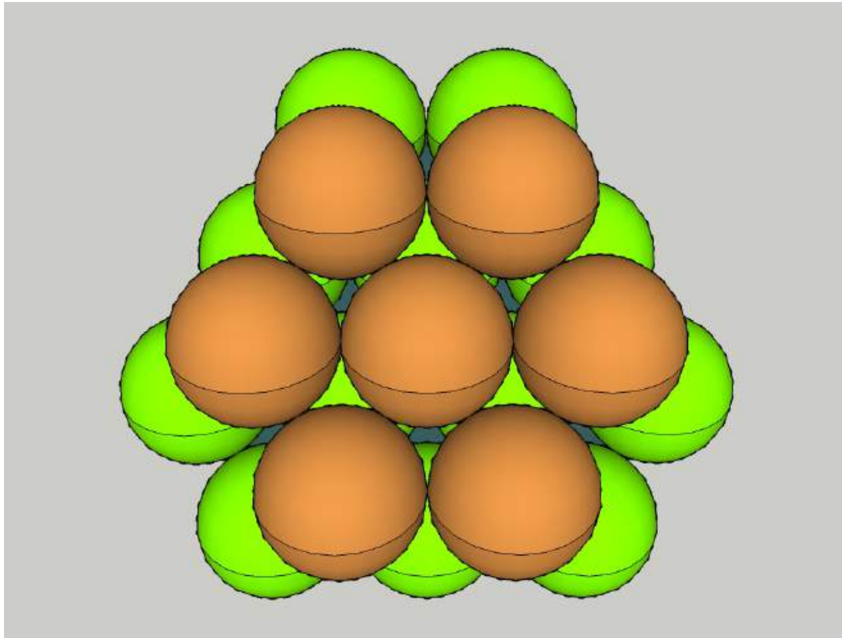

Figure A.3: The (111)-plane of Cu is shown. The different layers of Cu atoms are displayed in different colors.

A.1.3 Graphene

In this section, a short overview of the properties of Graphene is given. The reader should keep in mind that the properties listed here are the best theoretically achievable properties. In reality, defects and anisotropy may severely limit these values.

General properties

In Table A.3, the relevant physical properties are given. When looking at those, one can easily understand the interest in Graphene as an electronic material (electron and heat transport are much higher than for conventional metals and semiconductors). Its physical properties are also worth the attention Graphene receives.

Table A.3: Physical properties of Graphene [2].

Property	Value
Carrier Mobility	200.000 cm^2/Vs
Tensile Strength	130 GPa
Young's Modulus	1000 GPa
Coefficient of Thermal Expansion (Room Temperature)	-6 $*10^{-6}K^{-1}$
Thermal Conductivity (RT)	5000 W/mK
Bandgap (Tunable)	0.3 eV

Unit Cell

The unit cell of Graphene is shown in Figure A.4. It consists of two Carbon atoms. The crystalline structure of Graphene has threefold symmetry, as can be seen if the centre of a Carbon atom is taken as the frame of reference.

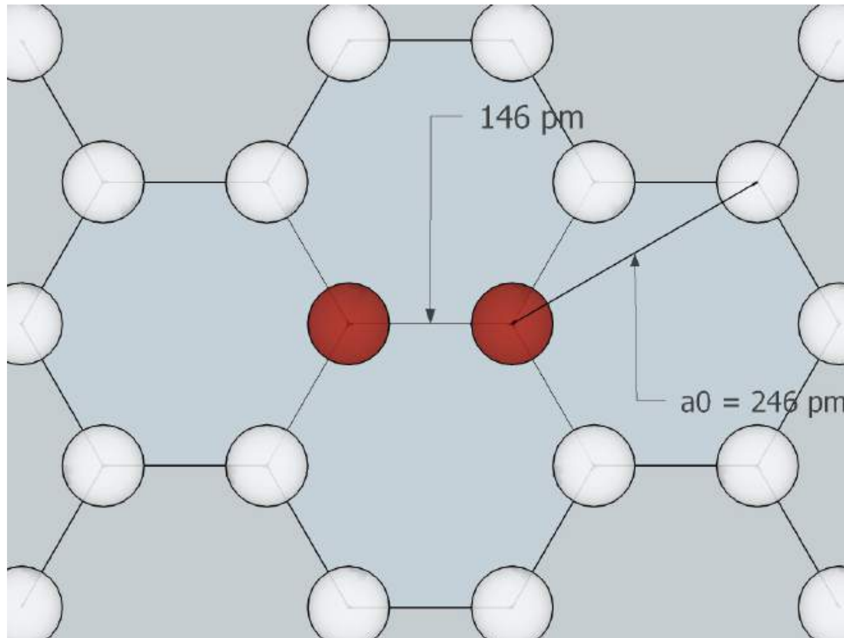

Figure A.4: The Unit Cell of Graphene is indicated in dark red. The distance between two Carbon atoms is 146 pm and the lattice parameter $a_0 = 246pm$.

A.2 Processing steps

In this section, a discussion of the experimental procedures followed in this thesis is given. These are subdivided into five categories: Cleaning, Annealing, other

Sapphire surface treatments, Sputtering, and Graphene growth. For a discussion on the theoretical aspects of these procedures and their intended effects, the reader is referred to Chapter 2.

A.2.1 Acid Clean

The Cleaning procedure applied during this thesis is a standard *imec* clean for Sapphire substrates. A clean beaker (only used for this procedure) is filled with a mixture of $H_2SO_4 + H_3PO_4$ and heated up to $300°C$. The Sapphire wafers are cleaned in this solution for 20 minutes, and then washed in Ultra Pure Water (UPW) for 3 minutes. The wafers are then blow-dried in pure N_2 and stored in Teflon containers.

Sulphuric Acid

In this procedure, 96% concentrated Sulphuric Acid (H_2SO_4) is used.

Phosphoric Acid

In this procedure, Phosphoric Acid (H_3PO_4) -based etchant is used :*Honeywell Phosphoric Acid Etching Mixture* containing 73% H_3PO_4, 3.3% CH_3COOH, 20.6% H_2O, 3.1% HNO_3.

A.2.2 Anneal

Different types of annealing procedures are used during this thesis. One can distinguish two classes of anneals: the ones performed on the pure sapphire substrate, and the ones performed on the sputtered Cu layers.

Sapphire substrate

Three types of anneals were performed on the Sapphire substrates: *ex situ* Low-Temperature Anneal (LTA), *ex situ* High-Temperature Anneal (HTA), and *in situ* vacuum anneal.

LTA The LTA is performed in 2000 standard cubic centimeters per minute (sccm) Oxygen for 30 minutes at $850°C$ in the Annealsys Oven AS-One, in the $III - V$-area of the *imec* 1 cleanroom.

HTA The HTA is performed in 600 l/h Oxygen for 12 hours at $1100°C$ in the Nabertherm Oven, in the nanolab, in the extension of the *imec* 1 cleanroom.

Vacuum Some wafers undergo an *in situ* vacuum anneal, right before Cu deposition. This anneal is performed for 30 minutes at $200°C$ below $1 * 10^{-3} mbar$ of Ar.

Deposited Cu layer

The anneal of the deposited Cu layer is done in the Aixtron Black-Magic CVD tool in the nanolab, in the extension of the *imec* 1 cleanroom. Two potentially important parameters for the crystallinity of the Cu layer are the temperature and the anneal time, and are not fixed. These are given wherever necessary. The pressure is kept constant at 90 $mbar$

A.2.3 Other

The two following procedures are also applied on some samples, but cannot be added to the classification discussed above.

Oxygen Plasma

Samples are annealed in Oxygen Plasma with 100 W RF power at room temperature for 30 min.

Ion Milling

The Ion Milling procedure is performed *in situ*, right before the Cu deposition. The chamber is brought to an Argon pressure of $1.9 * 10^{-4} mbar$, and the samples are either sputtered for 30 min at an energy of 200 eV or for 3 min at a beam energy of 150 eV

A.2.4 Sputtering

The Cu layer is sputtered onto its Sapphire substrate in two different Sputtering setups.

Microscience Lab

The sputtering tool located in the Microscience Lab of the KULeuven (in the department of Physics, 200D) is used to deposit Cu on some samples. The deposition parameters (pressure, power, TSD, time) may vary. They are given wherever relevant.

Nimbus tools

Two Sputtering tools located in the cleanroom of *imec* 1 are used to deposit Cu layers. The Nimbus 310 is located $III - V$-area of the *imec* 1 cleanroom and the Nimbus 314 is located in the pilot line. In both cases a standard recipe for deposition is used: Cu is sputtered at 3000 W for 173 seconds (21 passes under the target), at RT under $4.5 * 10^{-3} Torr$ (for Nimbus 310) or $3 * 10^{-3} Torr$ (for Nimbus 314), in both cases with TSD $= \ 80\ mm$. The results do not vary significantly depending on which Nimbus tool is used. Typically, the Nimbus 310 is used for deposition, whenever the Nimbus 314 is used, it is mentioned explicitely.

A.2.5 Graphene growth

Graphene growth is performed in an Aixtron Black Magic Graphene CVD oven. Graphene is grown under constant pressure, 90 $mbar$, at varying temperatures (typically around 1000°C) for various amounts of time (typically 10..30 min). The concentration of gases in the chamber (Ar, CH_4 and H_2) is also varied.

A.3 Process Flows

In this Section, the succesion of process steps involved in the different applied process flows relevant to this thesis ise detailed.

A.3.1 From Miller et al.[1]

Sapphire wafers are annealed at 1100°C in O_2 for 24 hrs at atmospheric presssure and mounted in the deposition chamber without further treatment. The samples are sputtered in 0.17 Pa of Ar, at a TSD of 8 cm and with a power of 100 W, for 8 min at the specified temperature.

A.3.2 Towards the State-of-the-Art

In this section, the process flow of Miller et al.[1] is slightly modified in order to be useable with the available materials. The samples are first cleaned according to the acid cleaning procedure.

The samples undergo an LTA and are then mounted into the Cu sputtering chamber of the Microscience lab.

Immediate deposition

The samples are sputtered immediately after the LTA in the Microscience lab for 15 min at room temperature, in an Argon atmosphere at $1.7 * 10^{-3}$ $mbar$, at a TSD of 80 mm, with a sputtering power of 100 W (450 V, 225 mA).

Vacuum Anneal

Immediately after the LTA, the samples are annealed in vacuum (Ar pressure $1.7 * 10^{-3}$ $mbar$) at 200°C for 30 min, and sputtered for 15 min close to 70°C, in an Argon atmosphere at $1.7 * 10^{-3}$ $mbar$, at a TSD of 80 mm, with a sputtering power of 100 W (450 V, 225 mA).

A.3.3 Epitaxial Cu

All the samples first undergo a chemical clean.

Microscience Lab

Two different procedures are used, at Room Temperature and at $85°C$.

Room Temperature The samples are inserted in the deposition chamber in the Microscience lab immediately after the clean, and sputtered for 8 min at a TSD of 60 mm, in $1.7 * 10^{-3}$ $mbar$ of Ar at Room Temperature, with a sputtering power of 100 W (480 V, 220 mA).

High Temperature The samples are inserted in the deposition chamber in the Microscience lab immediately after the clean, and sputtered for 15 min at a TSD of 80 mm, in $1.7 * 10^{-3}$ $mbar$ of Ar at $85°C$, with a sputtering power of 100 W (440 V, 230 mA).

Nimbus tools

The procedures followed in the two different Nimbus sputtering systems are slightly different.

Nimbus 310 The samples are mounted on a Si carrier wafer with vacuum-resistant tape. They are sputtered at Room Temperature for 173 sec at $4.5 * 10^{-3}$ $Torr$ of Ar, with a sputttering power of 3000 W (460 V, 6500 mA). The TSD (= 50 mm) could not be modified.

Nimbus 314 The samples are mounted on a Si carrier wafer with vacuum-resistant tape. They are sputtered at Room Temperature for 173 sec at $3 * 10^{-3}$ $Torr$ of Ar, with a sputttering power of 3000 W (460 V, 6500 mA). The TSD (= 50 mm) could not be modified.

A.3.4 Graphene growth

All samples finally undergo an anneal/Graphene growth step in the Aixtron Black Magic. The parameters of this procedure are given whenever necessary.

A.4 Atomic Force Microscopy

The importance of the topography of the crystalline substrate whereon the epitaxial Cu layer will be deposited has been pointed out in the literature review (see Chapter 2). To provide an image of this surface, a Scanning Probe Micrsocopy (SPM) method called Atomic Force Microscopy (AFM) is used. In AFM, an atomically sharp tip (typically made out of Silicon, Borosilicate glass, or Silicon Nitride) translates over a small area of the sample to be imaged (in the order of μm), at a distance sufficiently small to feel the influence of the nearby substrate. As the name AFM indicates, the physical quantity being measured here is a force. Depending on the measurement parameters, this can be either an electrostatic force, a capillary force,

a van der Waals force, a contact force, a chemical bond, etc.

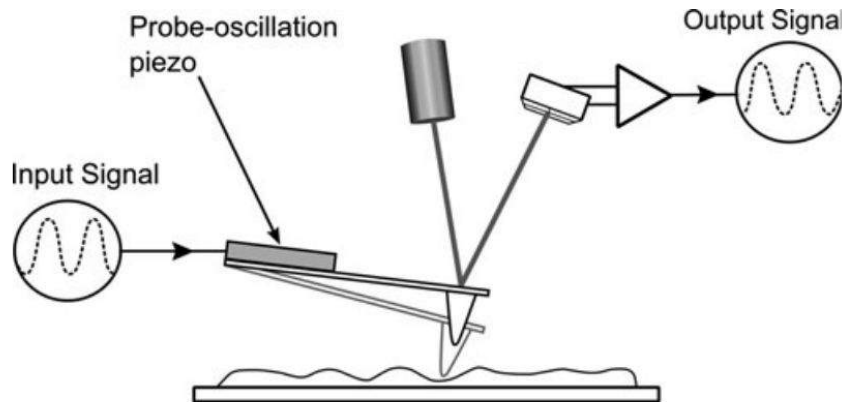

Figure A.5: Schematic of a typical AFM setup. From P. Eaton [8]

The atomically sharp tip translating over the substrate is attached to a cantilever beam, see Figure A.5. The force applied on the tip causes a deflection of this cantilever, according to Hooke's law, which is linear in the force, see Eq. A.1. By measuring the deflection of the cantilever, the force onto the tip and the position of the tip (and therefore the surface) can be derived.

$$F = -kx \tag{A.1}$$

Finally, besides its analytic use, an AFM can be used for processing purposes. The interaction between the tip and the surface can be used to manipulate single atoms [73]. This application was not used in this work, and so it will not be discussed in further details.

A.4.1 Modes of operation

AFM operation can usually be classified into one of the three following modes: Contact or static mode (as opposed to the two others classified as dynamic), tapping mode, and non-contact mode. The following sections go into further detail on these three modes.

Contact Mode

In contact mode AFM, the tip is dragged accross the surface of interest, at distances of typically less than a few Angströms. The measured signal (the deflection of the cantilever) is used in a closed feedback loop to move the cantilever up and down, so that the tip stays at the same height with respect to the local substrate surface. This allows to keep the deflection of the cantilever in the linear region.

Due to the short distance between the tip and the surface, the interaction force between the two can be quite strong. It is therefore not the method of choice when loosely bound structures need to be imaged, like adsorbed proteins or, in this case, Graphene. They might move under the effect of this force, or the surface might get damaged. Additionally, under normal conditions a sample is covered in a thin film of adsorbed water, which might cause stiction of the tip upon retracting. Finally, the static nature of the measured signal makes it more sensitive to drift and noise, which is undesirable when the structures of interest have characteristic heights in the order of a fraction of a nanometer.

Tapping Mode

In tapping mode AFM, the cantilever-tip are driven to oscillate near the resonance frequency of the structure, see Eq. A.2 where the the first natural frequency is given. In this expression, a rectangular section of the cantilever is assumed, where $\alpha_0 = 1.875$, E is the Young's Modulus of the cantilever material, I is the moment of inertia of the cantilever, ρ is the density of the material, A the rectangular section, and L the length of the cantilever:

$$\omega_0 = \alpha_0^2 \sqrt{\frac{EI}{\rho A L^4}} \tag{A.2}$$

The amplitude of this oscillation is measured, and decreases under the effect of attractive forces from the surface. The amplitude of the oscillation is kept constant by a closed feedback loop, which adjusts the average height of the cantilever with respect to the surface. Because the tip does not come into direct contact with the surface, this mode of operation typically induces less damage onto the surface and adsorbed molecules which may be imaged.

Additional information about the chemical nature of the surface can be derived from the phase of the oscillation. When different molecules are adsorbed, they do not only change the topography of the surface, the chemical bonds holding their atoms together interact differently with the AFM tip. This influences the tapping phase (an easy way to think of it is stickyness; if a molecule is adsorbed onto the surface which has a different attractive or repulsive behaviour with respect to the tip, it influences the tapping phase) of the oscillation. This can be used as a method for locating adsorbed molecules. An application in this work is locating cracks in Graphene. Cu and Graphene influence the tapping phase differently, which means that small areas where the Graphene is defective can be easily detected on a phase image, whereas it is much more difficult to derive this information from an amplitude measurement, due to the surface roughness.

Non-Contact Mode

In non-contact mode, the AFM tip never comes into direct contact with the surface. Instead, the cantilever is brought to vibrate at either its oscillation frequency or just

above, depending on the nature of the measurement. The interaction of the tip with the surface of the sample influences the oscillation frequency and amplitude of the cantilever. A closed feedback loop system is used to maintain a constant oscillation frequency or amplitude (non-contact mode can be used either in frequency modulation or amplitude modulation), by moving the cantilever up and down with respect to the surface. This actuation then provides the required information concerning the topography of the sample.

Because the AFM tip never comes into mechanical contact with the surface, non-contact mode can be used to image very soft samples. In general AFM tips and the sample surface undergo the least damage in non-contact mode. Additionally, if the sample is covered in a few monolayers of adsorbed liquid, non-contact mode allows to both probe the surface of the sample, and the liquid layer.

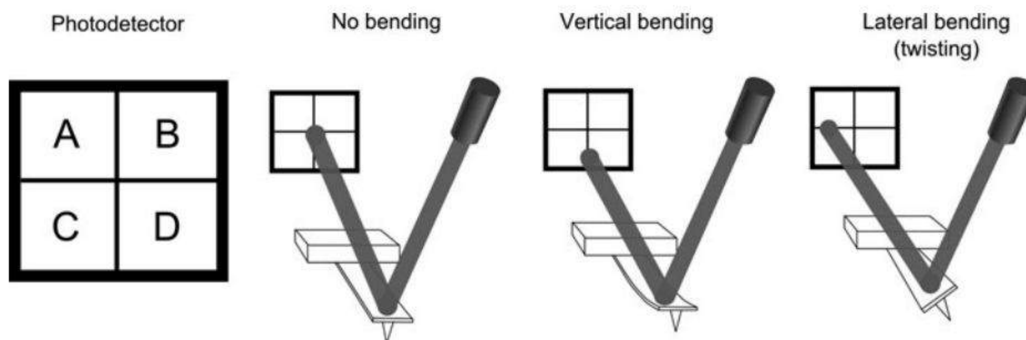

Figure A.6: The photodetector, consisting of four separate photodiodes A, B, C, and D, can detect both vertical and lateral bending. From P. Eaton [8]

A.4.2 Beam deflection measurement

The most commonly applied method for measuring the deflection of the cantilever uses reflection of laser light, as illustrated in Figure A.5. A solid state laser diode shines light directly onto the cantilever, which is coated with a reflective material. The reflected light moves as a function of the beam angle, and the position of the reflection light spot can be analyzed by a Position Sensitive Detector. This device consists of four adjacent photodiodes arranged in a square pattern. The intensity of the laser light modulates the conductivity of each diode separately, which allows to precisely locate the reflected spot, see Figure A.6. Since the position of this spot is proportional to the deflection of the cantilever itself, this provides a direct and accurate method for determining its position.

A.4.3 Tool technical aspects

The AFM pictures are collected in an Bruker AFM Dimension Edge in Tapping Mode. The micrsocope is supported by an air-table and protected by an isolation

chamber. The Olympus OMCL-AC160TS-R3 cantilevers have a resonance frequency of 300 kHz and operate in air.

A.5 X-Ray Photoelectron Spectroscopy

An AFM analysis provides very little information concerning the chemical composition of the surface of a sample. For this purpose, XPS is an interesting method. It provides information about the ratio of elements present in roughly the first 10nm of the surface, as well as chemical bonds, electronic states, possible contamination etc.

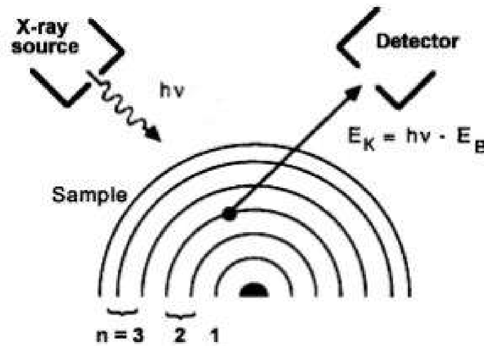

Figure A.7: The basic principle of XPS. An electron can be ripped off its atom by an incoming photon and detected. From H. Bender [9].

The working principle of XPS is as follows: a beam of high energy photons, in this case X-Rays, contains a sufficient amount of energy to rip off electrons from the surface atoms, thereby ionizing them (this is an expression of the Photoelectric Effect, a schematical representation of the phenomenon is given in Figure A.7). Note that the correction factor ψ for the detector work function is not taken into account in Figure A.7. These electrons are propelled away from the surface, and have a kinetic energy that can be related to the energy of the chemical bond in which this electron was previously involved through Eq. A.3. There, $\hbar\omega$ refers to the energy of the X-Ray, and ψ is a correction factor due to the detection system (it can be seen as a work funcion). By counting the amount of electrons that are emitted as a function of their energy, the chemical and electronic structure of the surface of the sample can be derived.

$$E_{bond} = \hbar\omega - E_{kin} - \psi \tag{A.3}$$

A.5.1 Experimental system

A typical XPS system consists of mainly the following three components: an X-Ray source, a vacuum chamber containing the sample, and an energy-resolved electron detection system.

The X-Ray source provides radiation with a well defined wavelength (which is a requirement for being able to relate the energy of the electrons to the bond energy through Eq. A.3). Due to their high energy nature, however, X-Rays cannot be focused (at least not with a lens), and the spot size which is analyzed is at best in the order of a few tens of μm, often much larger. The lateral resolution of XPS is thus very low.

The electrons emitted upon absorption of an X-Ray photon by an atom need to travel undisturbed until the detector. This means, first of all, that only the few top layers of the surface of a material can be imaged (electrons can be emitted from deeper inside the material, but are very likely to be reabsorbed before leaving the material). Additionally, this requires that the measurement should take place in a high vacuum environment (typically below $10^{-8} mbar$).

Finally, the emitted electrons need to be detected, and the detection mechanism must be able to differentiate electrons with different kinetic energies. A straightforward method for doing this is applying a magnetic field $\vec{B}$ perpendicularly to the motion of the electrons (note that very few of the emitted photoelectrons are actually detected, most of them do not fly towards the detector). This magnetic field filters the electrons based on their kinetic energy (which can be derived from their speed), because of the different path they travel on. These paths are described by the Larmor Radiusr_L:

$$r_L = \frac{v_e m_e}{(-e)\, B} \tag{A.4}$$

Equation A.4 shows that electrons with a different speed travel along a different path in the detector. Since the charge e, the modulus of the magnetic field B and the mass of the electrons m_e are constants, the Larmor Radius depends solely on the speed of the electrons.

A.5.2 Modes of operation

Three measurement modes are available for XPS systems. They are called line profiling, depth profiling and angle resolved (XPS).

In line profiling XPS, the X-Ray spot is moved accross the surface, thereby providing information about the uniformity of the surface composition over large areas. In advanced systems, full wafers can be analyzed.

In depth profiling, the composition of a sample is measured as a function of depth. Data from underneath the surface is made accessible by ion beam etching, therefore *de facto* replacing the surface by an atomic layer a few nanometers deeper. This etching step destroys the sample, but it allows, theoretically, to measure the concentration profile over the entire thickness of a material.

In angle resolved XPS, the electrons emitted by the surface after X-Ray irradiation are collected as function of the exit angle. Electrons traveling at a high exit

angle can only originate from the few top atomic layers. The pathlength inside the surface of the sample would otherwise be too long, and the electron would have a high probability of being reabsorbed. The electrons emitted in a direction almost perpendicular to the surface originate on average from deeper inside the sample. They reflect the "bulk" (10 nm depth) structure of the material. This method allows to create a depth profile (although limited to a few nm) without damaging the sample.

A.5.3 Tool technical aspects

The XPS measurements are carried out in Angle Resolved mode in a Theta300 system from ThermoInstruments. The measurements are performed using a monochromatized Al Kα X-Ray source and a spot size of 400 μm. Standard sensitivity factors are used to calculate atomic concentrations. Therefore, they may deviate from reality in the absolute sense (20% relative). Long term repeatability of composition analysis is much better: 1%.

A.6 X-Ray Diffraction

When a thin Cu layer has been deposited, it is necessary to analyze its crystallinity, which can excellently be done using X-Ray Diffraction. This method (also called Crystallography), relies on the scattering of single X-Rays by electrons inside a (crystalline) material. The pattern that the X-Rays form after interaction with a crystal is due to the interference of all scattered X-Rays. This can mathematically be represented as the Fourier Transform of the electron density inside of the crystal which causes the diffraction pattern.

X-Ray Diffraction is a versatile characterisation method, that can be used for several different purposes. The best example comes from physical biochemistry, where XRD allows to determine the position of every atom inside a protein, given that a crystal can be made out of it. Additionally, XRD characteristics of gases, liquids and amorphous solids sometimes contain interesting information as well. Liquid crystals are an example of a material that does not as such belong to any of these classes, where crystallographic data is nevertheless very interesting. Finally, for materials scientists, XRD is useful when it comes to determining the crystalline quality of a material. This last example is the one that is relevant to this dissertation, and which will be discussed in further detail.

Due to the importance of characterisation through XRD in this work, the section will be slightly longer, with a more pronounced accent on the physics of scattering and diffraction.

A.6.1 Diffraction

In this first section, the physics behind the phenomenon of diffraction is discussed. First, the mechanism that causes X-Rays to virtually bend under the effect of a material is explained. In further sections, two ways of using knowledge of this mechanism to describe diffraction are derived.

Scattering and interference

The electric field of any electromagnetic wave interacts with the charges that are present in its path. If the example of a single free electron is considered, the image is easy to understand. The electric field of the X-Ray causes the electron to oscillate with the same frequency as the incident photon. This oscillation causes the electron to emit a spherical electromagnetic wave (accelerating charges emit electromagnetic waves). The intensity of the interference of the emitted and the incident wave, as seen by an observer, can be computed from classical electrodynamics [74], and is:

$$I_S = I_0 \left(\frac{\mu_0}{4\pi}\right)^2 \frac{e^4}{m^2 \left\|\vec{R}\right\|^2} sin^2\phi_z \tag{A.5}$$

In Eq A.5, I_0 is the intensity of the incoming X-Ray, $\vec{R}$ is the position of the observer with respect to the equilibrium position of the electron, ϕ_z is the angle that vector $\vec{R}$ makes with the electrical field of the X-Ray, and m is the mass of the oscillating charge. This expression shows that X-Rays are propagated in all directions by the oscillating electron (this is called a spherical wave). It also shows that scattering by other charged particles (such as much heavier protons), is a mostly neglectible effect due to the inverse square dependence of the emitted intensity on the mass of the oscillating particle.

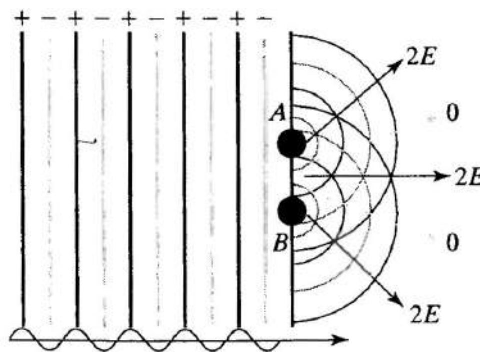

Figure A.8: When planar waves encounter objects (here slits in a screen) in the order or smaller than their wavelength, they act as sources for new spherical wavefronts. These wavefronts will interfere, in case there is more than one. From Van Holde [10].

Of course, this idealized situation is of no practical interest. In the real world, X-Rays travel in a beam, and scatter from clouds of electrons. These different rays will undergo scattering by different electrons. Each of these electrons oscillates, and behave as an individual source of spherical wavefronts. In the limit of many electrons, the interaction of these wavefronts causes complex spatial distributions of the X-Rays. This is due to superposition of the fields of every wave, a phenomenon called interference. It is easiest to understand when looking at two spherical sources emitting at the same frequency and in phase (in fact this is no different from a double slit experiment, see Figure A.8). At some points in space, the electric fields of the individual waves reinforce each other, resulting in an increased amplitude, which is called constructive interference. At other points, these fields may cancel each other out, thereby resulting in a localized suppression of the wave, which is called destructive interference.

When the waves scattered by all the electrons inside a material interfere, the resulting waves contain information about the position of all these electrons. This allows to compute these positions, thereby resolving the structure of the material. This is equivalent to performing an inverse Fourier Transform on the diffracted beam. This is beyond the scope of this thesis, and will only be mentioned in very little detail in the last paragraph of this section.

Bragg Condition

Working with single X-Rays diffracted by single electrons is not feasible for macroscopic samples. Therefore, simplifications need to be introduced, in order to model the behaviour of X-Rays interacting with a material. The two main models for diffraction which are of interest to us are the so called Bragg and Von Laue laws of diffraction. The first one, proposed by W. L. Bragg, is a simplification of the system, which considers the crystal being characterized as a stack of perfectly reflecting planes.

When a beam is incident on this stack of planes with an angle of θ, individual rays reflected by a different crystalline plane travel a different distance, thereby undergoing phase shifts. This situation is illustrated in Figure A.9. The difference in travelled path, the path difference PD, of two rays reflected from neighbouring crystalline planes is dependent on both the distance d between these planes, and the angle of incidence θ:

$$PD = 2dsin\theta \tag{A.6}$$

If these reflected waves are in phase with each other, they constructively interfere with each other, and an observer is able to measure them. In order for these waves to undergo constructive interference, the PD has to be equal to an integer amount of wavelengths: $PD = n\lambda$. This requirement can be inserted into the formula for the path difference, which gives Bragg's law of diffraction:

$$2sin\theta = \frac{n\lambda}{d} \tag{A.7}$$

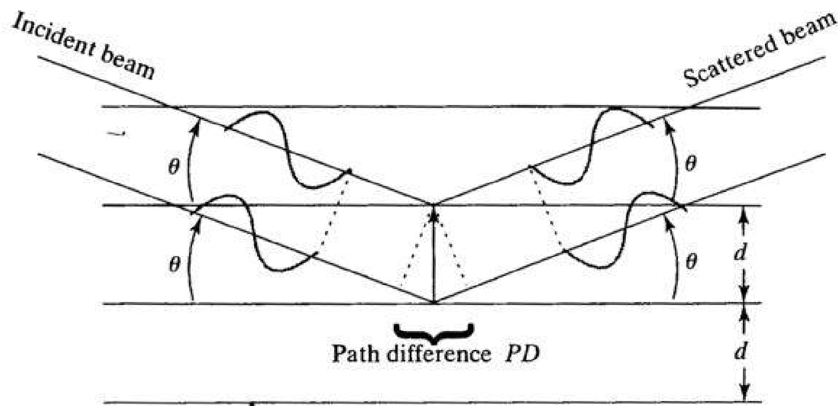

Figure A.9: Two waves reflecting on Bragg planes. The angle of incidence (and of "reflection") is θ, so two waves will travel along paths of different lengths. From Van Holde [10].

This Bragg condition was derived for two reflective planes, but can without adaptation be extended to an infinite stack of reflective planes. In that case, the only angles at which a diffracted wave appear are the angles which satisfy Bragg's law. Under all other conditions, the diffracted waves destructively interfere with each other, and no resulting wave can be measured.

Eq A.7 provides interesting information on the parameters influencing X-Ray Diffraction. First, if small inter-plane distances d need to be measured (for atomic layers this is in the order of a few Angström), the wavelength should be be in the same order of magnitude, ideally even smaller than the inter-plane distance. Secondly, if this wavelength is known, a diffraction measurement provides important information concerning the distance between the crystalline planes (though sometimes additional information may also be necessary).

The Bragg condition on its own, however, cannot always provide sufficient information. It is too much of a simplification to consider a three dimensional diffractive crystal as a one dimensional stack of reflective planes. In order to provide a more comprehensive explanation of XRD, the Von Laue theorem of diffraction needs to be mentioned.

Von Laue Condition

In the Von Laue theorem, diffraction is not modeled by reflection from stacked crystalline planes, but by scattering of X-Rays by the electron clouds of individual atoms. The simplest way to introduce this theorem is by looking at a one dimensional crystal, i.e. a row of atoms, onto which X-Rays are incident along a normal to the crystal. A schematic representation is given in Figure A.10. Each of the atoms in the 1D crystal acts as an individual source of spherical waves with the frequency

and phase of the incident rays, which interfere with each other. The concept of path difference can be applied here as well, to determine what waves interfere constructively. The condition here is again $PD = l\lambda$, with l an integer. Take γ the angle between the incoming wave and the scattered wave, then the condition for constructive interference is:

$$l\lambda = c * cos\gamma \tag{A.8}$$

Here, l is an integer and c is the distance between the different atoms in the 1D crystal. Again, if one considers an infinite row of atoms, the only measurable waves are scattered at angles γ which satisfy Eq A.8. Note that this condition can be compared to the Bragg condition by drawing a reflective plane through each atom, which makes an angle θ with the incoming and scattered waves, see Figure A.10. The dotted lines indicate the "reflective planes", as they are used in the Bragg condition.

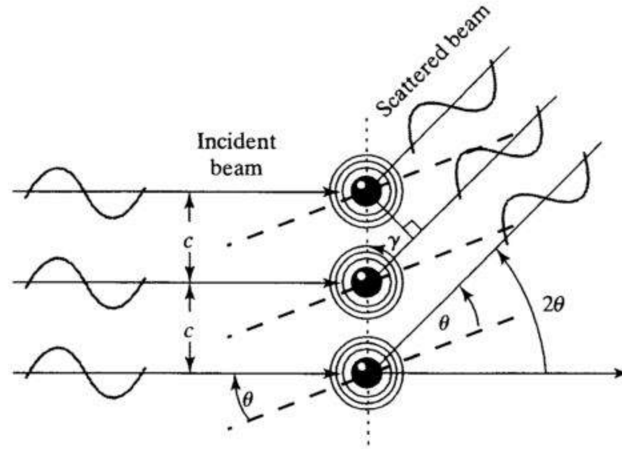

Figure A.10: Diffraction of light waves due to the electron clouds of a one dimensional crystal of atoms. From Van Holde [10].

Allowed reflections

In crystallography, the symmetry of a unit cell can influence which crystalline planes can provide a diffraction signal and which ones cannot. The diffraction pattern from certain crystalline planes is extinct, these (absent) signals are called forbidden reflections. The only signals that are visible are called allowed reflections, and for Sapphire (consider it a HCP-like crystal), the coordinates of these planes can be found in the *International Tables for X-ray Crystallography, Volume I, 1972*:

$$\begin{aligned} -h+k+l=3n \quad & for \quad general\,(hkil) \\ l=3n \quad & for \quad \left(hh2\bar{h}l\right) \\ h+l=3n \vee l=2n \quad & for \quad \left(h\bar{h}0l\right) \\ l=6n \quad & for \quad (000l) \end{aligned} \tag{A.9}$$

In Eqs. A.9, $(hkil)$ are the Miller-Bravais indices of the crystalline plane, and n is an integer. Note that double diffraction can allow seemingly forbidden reflections to appear in the measured signal. E.g. in the $\left[1\bar{1}00\right]$ zone, the (0003)-plane can virtually cause a diffraction signal [75]:

$$11\bar{2}3 + \bar{1}\bar{1}20 = 0003 \tag{A.10}$$

Diffraction as a Fourier Transform

Without deriving it, Eq A.11 shows that the wave scattered by an arbitrary spatial distribution of electrons $\rho(\vec{r})$ can be represented as the Fourier Transform of this distribution of electrons [74]:

$$\begin{aligned} F\left(\vec{Q}\right) &= A_0\sqrt{p}\frac{\mu_0 e^2}{4\pi m_e R}\int_{\vec{r}}\rho(\vec{r})\, e^{i\vec{r}\cdot\vec{Q}}d\vec{r} \\ with\,\vec{Q} &= \frac{2\pi}{\lambda}\Delta\vec{k} \end{aligned} \tag{A.11}$$

From Eq A.11, one can theoretically derive the spatial distribution of electrons in any material, given that the scattered wave is entirely known. This is impossible in practice, as phase information is necessary as well when an (inverse) Fourier Transform must be performed, while X-Ray detectors can only measure the absolute value of a wave. Nevertheless, algorithms can be developped that use the diffraction pattern of a crystalline material to, in combination with other measurement techniques, determine the structure of this material.

A.6.2 Modes of operation

The information that can be derived from XRD measurements differs depending on the way the sample rotates with respect to the incoming beam of X-Rays. If the surface crystalline plane of a sample needs to be probed, a typical method (which can be understood using the Bragg law of diffraction) is to vary the angle of incidence θ, and measure for which θ the diffracted wave undergoes constructive interference. This method is discussed under the 2θ scan section.

Another method of importance for this work is called a *Phi* scan. When it is necessary to probe the relative in-plane orientation of different grains, a 2θ measurement does not suffice. According to Bragg's law, it only gives information about the stacking of crystalline planes. In order to get information on the orientation, the diffraction pattern (in fact, the presence or absence of a diffraction peak) of planes not parallel to the surface is imaged, and therefrom the angle between those planes.

2θ scan

As was already said in the previous paragraphs, the principle behind a 2θ scan can be easily understood using the Bragg law. As can be seen in Figure A.10, the angle between the incident and the scattered beam is indeed 2θ (the complementary angle

of γ). A quick look at Eq A.7 gives the angles for which a diffracted signal can be expected. Because the crystal is given (in our case, a stack of Cu/Al_2O_3), we can use the Miller indices to determine the interplanar spacing (for planes with indices $(hkil)$ and lattice constants a and c, corresponding to the sapphire substrate) [75]:

$$d_{hkil} = \frac{1}{\sqrt{\frac{4*(h^2+k^2+hk)}{3a^2} + \frac{l^2}{c^2}}} \tag{A.12}$$

For an FCC metal like Cu, the interplanar distance can be calculated as follows (for planes with indices (hkl) and lattice constant a) [76]:

$$d_{hkl} = \frac{a}{\sqrt{h^2 + k^2 + l^2}} \tag{A.13}$$

With the interplanar distance known, the diffraction pattern of a crystal can be theoretically calculated using Bragg's law:

$$2sin\theta = \frac{n\lambda}{d} \tag{A.14}$$

The angle θ can be defined as the angle between the incoming beam and the surface of the sample (defined by the Miller indices). This way, by analysing the diffraction signal for a varying θ, one can determine whether the surface crystalline plane is indeed the expected one, and, in the case of Cu/Al_2O_3, the crystalline quality of the Cu(111) deposited onto the Sapphire. This only gives information on the different crystalline planes facing the surface, e.g. (111) or (200), not about presence of small or large grains, or the abundance of grain boundaries. This information is provided by the measurement method discussed in the next section.

When performing these calculations, one has to keep in mind the allowed and forbidden reflections of Sapphire. The c-plane of Sapphire has indices (0001), but this does not correspond to an allowed reflection. Instead, the following $(hkil)$-indices will be used: (0006). This corresponds to exactly the same crystalline plane in physical space, but the mathematics discussed in this section makes the distinction.

Φ scan

The analysis of the in-plane orientation of different Cu grains requires that planes not parallel to the surface of the sample be imaged. These still have to be the Cu(111) planes, since the angle at which these planes display a diffraction peak is known from the previous experiment. In Figure A.11, four relevant (111) planes of Cu are shown. It can easily be seen that these planes form a regular tetrahedron, and henceforth the angle between two planes can be derived from geometric principles, which yields a value of 70.5°. So by tilting a sample over exactly this angle of 70.5° (tilting the plane of both the incident and diffracted beams of the previous experiment, and making an angle θ with both these beams) allows to see the diffraction pattern of one of these "buried" (111) planes.

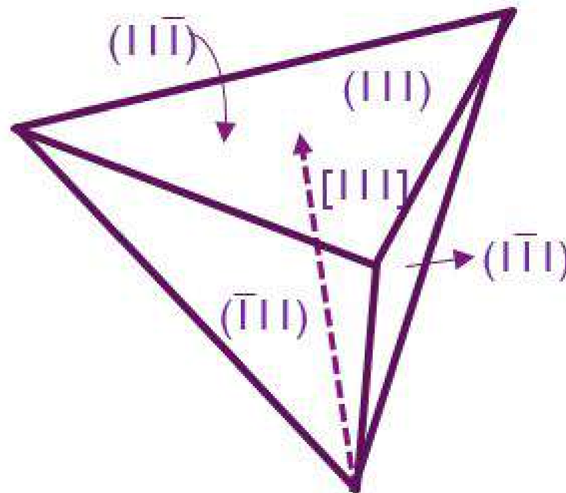

Figure A.11: Schematic representation of the four relevant $Cu(111)$ planes. The horizontal plane represents the sample surface. The three other planes are buried, and can be imaged by rotating the sample over an angle of 70.5°.

Upon rotating the sample around the axis perpendicular to its surface, represented by the arrow in Figure A.11 (the angle by which it is rotated is called Φ, hence the name), all these additional (111) planes can be imaged. Due to the preset from the 2θ experiment, the detector systematically finds itself in the position of a diffraction signal from one of these planes. Recording these signals as a function of angle Φ, allows to determine the in-plane orientation of the Cu(111) grains that are present in the sample.

Another look at Figure A.11 shows that the recorded signal can be expected to display diffraction peaks with a symmetry of 120°, since the equilateral triangle at the surface of the sample has the same symmetry. This can be related to the symmetry of the Cu(111) surface as shown in Figure 2.1. Note that the first atomic layer has a 60° symmetry. This can be deceiving, the second atomic layer needs to be taken into account as well. This indeed yields a 120° symmetry as expected.

The combination of the two measurement methods that were discussed in the previous paragraphs allows to completely characterize the crystallinity of a Cu(111) layer. Since this is the main topic of this work, XRD will be the most intensively employed technique.

A.6.3 Tool technical aspects

X-Ray Diffraction is performed with a PANalytical X'pert Materials Research Diffractometer. The Cu K-α wavelength (0.15418 nm) is used for Bragg-Brentano measure-

ments. The signal is measured in a PIXcel high-speed line detector with Ni filter and Anti-Scatter Slit.

A.7 Raman Spectroscopy

Raman Spectroscopy is a technique which can be used to assess the quality of a layer of graphene. The measurement setup is simple; a monochromatic light source (a laser) shines light onto a sample (in this case Graphene). The photons emitted by this light source are scattered by the atoms inside the sample, but in a way that is different from XRD, discussed in the previous section. The light used in Raman Spectroscopy is of lower energy, and can interact with atoms themselves. The scattered light may exchange some energy with the sample under test. This gives rise to a Raman Shift in the frequency (or wavelength) of the photons, which contains information about the chemical nature of the sample being probed.

The two first sections discuss the physics behind Raman Spectroscopy, while the third section treats the information contained in a Raman spectrum, specifically for the context of Graphene.

A.7.1 Scattering

In Section A.6, the scattering of X-Rays by single electrons and then electron clouds was discussed. Here, another approach to scattering is considered. Whereas X-Rays have a frequency that is too high to move atoms (they can break chemical bonds though, which is why X-Rays belong to the class of ionizing radiation), infrared and visible light and some part of the UV spectrum have this ability. Throughout the rest of this section, the focus will lay on visible light.

The incident visible light can excite low frequency rotational and vibrational modes in the crystalline lattice being irradiated. These are commonly called phonons. These phonons dynamically modulate the electric fields present in the lattice, which then scatters the light beams. Two scattering phenomena are important in Raman Spectroscopy: Rayleigh (elastic) scattering and Raman (inelastic).

In elastic scattering, the scattered photon does not undergo a frequency shift, its energy is conserved, hence the name "elastic". Elastic scattering typically happens much more often than inelastic scattering. It does not contain information about the material under test, so photons resulting from elastic scattering are filtered out of the signal.

In Raman scattering, the photons undergo a frequency shift, and can either loose or gain energy. This is called inelastic scattering. Depending on the initial state of the scattering centre before scattering occurs, the photon can undergo Stokes (looses energy) or anti-Stokes (gains energy) Raman scattering. These inelastically scattered photons contain information concerning allowed rotational and vibrational modes,

which in turn are influenced by the chemical properties (bonds and symmetry) of the material. A graphical representation of these processes is given in Figure A.12.

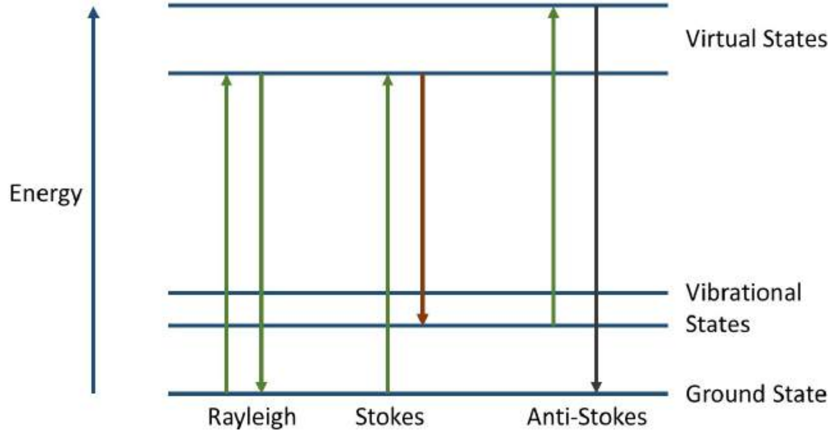

Figure A.12: Schematic representation of the processes undergone by an **atom** which scatters a visible photon.

A.7.2 Raman Shift

Each of the inelastically scattered photons from the previous section will be characterised by their Raman shift. This quantity, which is often given in terms of wavenumbers $\left[cm^{-1}\right]$, represents the change in wavelength (and therefore energy) with respect to the exciting light source:

$$\Delta w \left[cm^{-1}\right] = \left(\frac{1}{\lambda_0\,[cm]} - \frac{1}{\lambda_1\,[cm]}\right) \tag{A.15}$$

In Eq A.15, λ_0 represents the wavelentgh of the excitation laser, and λ_1 represents the wavelength of the Raman shifted photon.

A Raman spectrum consists of a distribution of the amount of scattered photons as a function of the Raman shift. For simple systems, where only a few rotational and vibrational modes can be excited, this Raman spectrum shows a set of peaks, each corresponding to a specific mode. For more complex systems (metals are a good example), the Raman spectrum consists of a continuous curve, due to the almost continuous range of modes that can exist in these systems.

A.7.3 Graphene

In this section, a typical Raman Spectrum for Graphene is analyzed, and the information it contains is pointed out. A typical Raman spectrum for Graphene can be

found in Figure A.13.

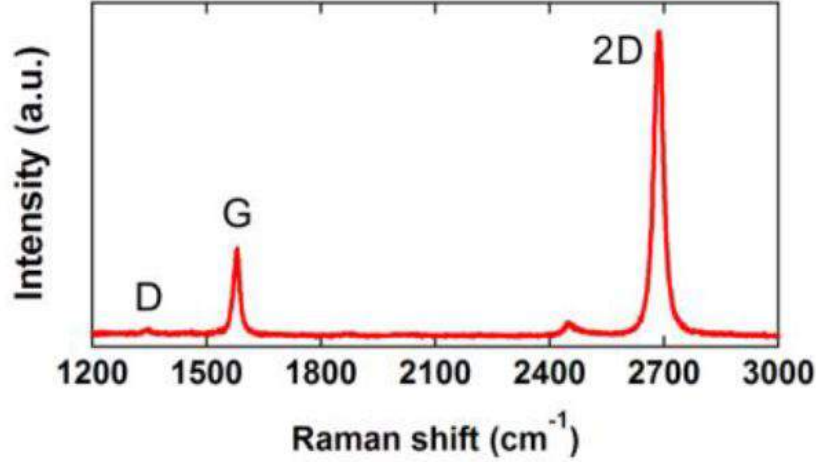

Figure A.13: Typical Raman spectrum of a Graphene flake. From Chung et al. [11].

The three most important features of a Raman spectrum in the case of Graphene are the D (Diamond) peak, at approximately $1350cm^{-1}$, the G (Graphite) peak at approximately $1620cm^{-1}$ and the 2D peak at approximately $2700cm^{-1}$. The D peak is an indication of the amount of defects (which scatter phonons) contained in the Graphene. It appears when the Graphene sample has poor crystallinity, when many grain boundaries, cracks, holes etc. are present. For ideal Graphene, the D peak is not present.

The position and the FWHM of the 2D peak is an indication of the amount of Graphene layers present. More layers widen the 2D peak and shift it to higher values of the Raman shift (typically to the right of the graph). The height of the 2D peak (with respect to the G peak) is also an indication of the amount of layers (for monolayer Graphene this ratio should be between 2 and 3). It is also influenced by doping of the Graphene, which can be due to the substrate underneath. Metals, including Cu, are known to dope Graphene. Therefore, the I_{2D}/I_G ratio for Graphene on Cu is significantly lower than 3.

With this in mind, the Raman spectrum in Figure A.13 can be analyzed. It shows good quality of Graphene, due to the almost inexistent D peak. Additionally, the I_{2D}/I_G ratio is in the order of three, which, in combination with the $FWHM$ of the 2D peak indicates that this represents monolayer undoped Graphene.

A.7.4 Tool technical aspects

Raman spectra were collected with a Horiba Labram HR, with a laser wavelength of $532nm$ and power of $2\ mW$. The spot size was $0.9\ \mu m$.

A.8 Scanning Tunneling Microscopy

In Scanning Tunneling Microscopy, an atomically sharp conductive tip is scanned under UHV conditions with atomic accuracy accross a conductive surface, without coming into contact with the latter. An electric field applied between the tip and the surface causes tunneling of charge carriers. The tunneling current, which can easily be measured, depends on the electric field, the density of states in the tip and the surface and most importantly, the distance between the tip and the surface. A schematic representation of an STM setup is given in Figure A.14.

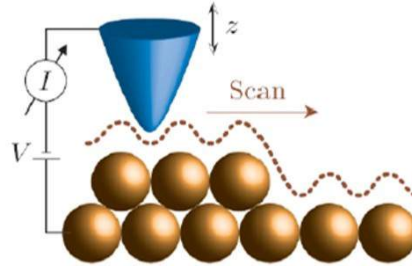

Figure A.14: Schematic representation of an STM setup. From W. Vandervorst [9].

The tunneling current depends exponetially on the thickness of the dielectric medium (note that in this case it is ultrahigh vacuum). This provides a very strong feedback signal: the tunneling current can change with up to an order of magnitude per 10 % (100 pm) change of the tip position. This is translated in a more than atomic resolution of STM images.

A.8.1 Tunneling and the principle of operation

Tunneling of charge carriers through a potential barrier is a quantum effect ascribed to the wave nature of charge carriers. Tunneling is used for metrology purposes in STM, but is also present in modern MOSFET devices, where it represents a significant challenge to scaling the gate thickness. In STM, the tunneling current is measured. An expression showing the main factors influencing the tunneling current is given below:

$$I_t \propto V \rho_s \, exp\left(-2 * \frac{\sqrt{2m\,(\Phi - E)}z}{\hbar}\right) \qquad \text{(A.16)}$$

In this formula, V represents the voltage applied accross the potential barrier, ρ_s is the density of electronic states at the surface of the sample, m is the effective mass of the charge carrier, Φ is the height of the potential barrier, E is the charge carrier energy, and z is the distance between the tip and the sample. The exponential dependance of the current onto this distance is the reason behind the depth resolution of STM. It also guarantees that only a very small area of the tip, being the area closest to the sample surface, is responsible for the tunneling current. This is in turn responsible for the lateral resolution of STM, which allows to probe for single atoms. Figure A.15 shows the tunneling current density distribution between an STM tip and a sample. The majority of this current originates from the single atom closest to the sample surface, hence the resolution. The combination of both depth and lateral

atomic resolution makes STM a valuable tool for probing the properties of Graphene adsorbed onto a $Cu\,(111)$ surface.

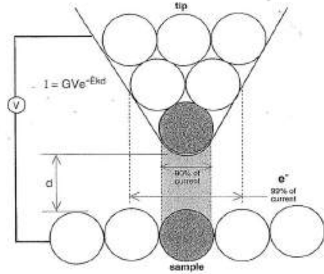

Figure A.15: Tunneling current density in STM. From W. Vandervorst [9].

The measurement mechanism allows to detect depth and lateral spacial variations in the order of a fraction of an atomic diameter. In a feedback loop system, this information is used to very accurately position the tip so that the tunneling current remains constant. This is done via piezoelectric actuation in the three dimensions. Piezoelectricity as an actuation (or measurement) mechanism is used in several nm precision mechanical systems, such as lithography machines, Atomic Force Microscopes, pressure sensors and many more.

The nm precision positioning mechanism sets a severe constraint on vibration isolation. The vibration insulating casing is the last (but not least) important element of any STM setup. Small amplitude vibrations make measurements impossible, and larger amplitudes (above 0.5 nm) induce the risk of damaging the tip, if it comes into contact with the sample.

A.8.2 Additional possibilities

STM experiments contain more information than just topological properties. In the formula for the STM current, Eq. A.16, the density of states and the potential barrier are shown to influence the tunneling current as well. This indicates that STM allows to probe the band structure of a material. In the case of Graphene onto a Cu surface, this allows to detect defects in the Graphene layers, grain boundaries, and information of doping of Graphene by the Cu surface.

A.8.3 Tool technical aspects

The STM measurements are obtained in an Omicron Scanning Tunneling Microscope at low temperatures (78 K and 4.5 K) under UHV conditions and with an open feedback loop.

A.9 Conclusion

The standard process steps applied on those materials were discussed. Most of these steps are discussed for completeness, and not all of them are used in the final process for depositing epitaxial $Cu\,(111)$. The combination of these process steps into process

flows is discussed as well.

The materials used in this thesis are discussed, with the focus on their relevant properties. These are mainly the crystalline properties of Cu and the surface properties of Sapphire. Graphene properties are discussed as well, though this is not the main scope of this thesis.

A non exhaustive list of relevant characterization techniques is given here. The shortcomings of every technique are compensated by advantages of other techniques, and vice-versa. When used together (and correctly) they allow to build up a comprehensive image of the quality of a Graphene-Cu-Sapphire stack.

Appendix B

Crystallography of Sapphire

Crystallography is, by far, the most used characterization technique in the present work. The principle behind XRD has been discussed in depth in Appendix A, and is not the subject of this appendix.

The coming discussion focusses on the XRD signature of Sapphire. This signature acts as a low intensity background in every measurement involving a Sapphire wafer. It is therefore interesting to dedicate an appendix to the information that can be derived from this background, and to the theoretical basis of this signal.

As a means of theoretical basis, a justification is sought for the presence and position of every feature observable in the diffraction pattern of Sapphire. Every such feature should be associated with a crystalline plane, with all corresponding position and diffraction angles.

Because every peak can (should) be associated with a specific crystalline plane, the XRD background of Sapphire makes it possible to determine the orientation of the Sapphire wafer. This knowledge can be associated with the knowledge of the position of the Primary Flat Location (see Section 3.1.1) to have absolute information.

Finally, if the orientation of the Sapphire wafer is known, it can be associated with the information provided by XRD patterns of a Cu/Al_2O_3 stack to determine the absolute OR. For this purpose, the definitions given in Eq. 2.2 are used.

Note that this appendix assumes a thorough understanding of the principles behind X-Ray Diffraction. These principles are discussed in detail in Section A.6.

In this appendix, most graphs and schematics make an extensive use of colours. The reader is therefore advised to use either a digital or a colour-printed version.

B.1 XRD background of pure $\alpha - Al_2O_3\,(0001)$

The background signal of the Sapphire substrate can often be seen in an Phi scan. A background signal that is recorded for a Sapphire substrate without Cu can be seen in Figure B.1. In the following section, a comprehensive discussion of these features is given, and an explanation is sought for every peak. The signal shows a 120° symmetry, with a major peak at $+30° + n * 120°$ and two minor peaks at $-15° + n * 120°$ and $-45° + n * 120°$, with n an arbitrary integer.

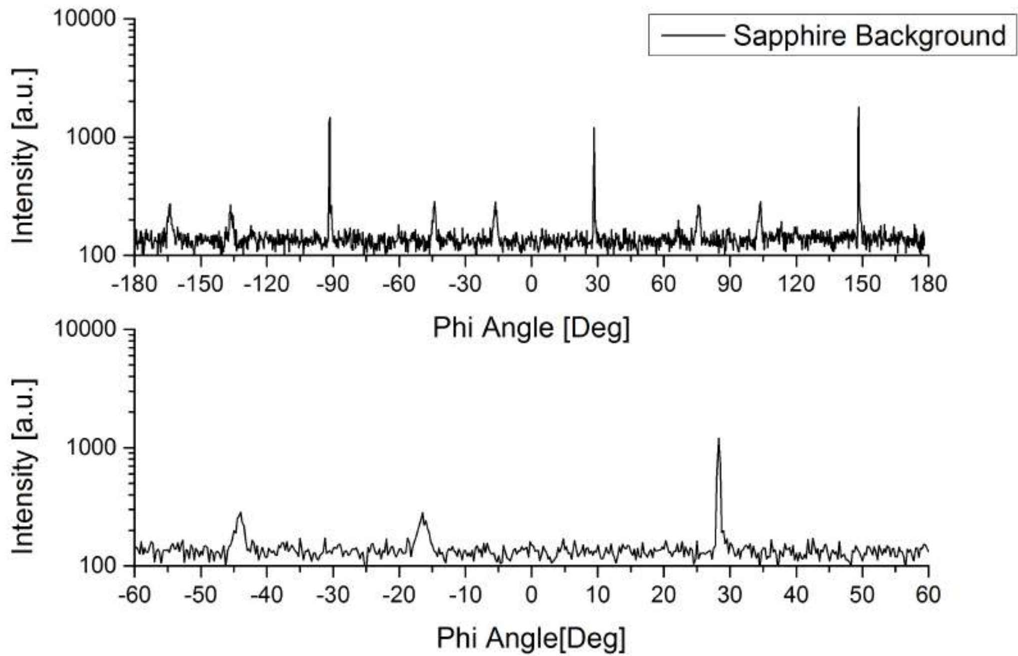

Figure B.1: Backgound signal from a Sapphire substrate. In the lower part of the figure, a zoomed characteristic in allows to identify the location of the repeated features.

B.2 Analysis of the features

To display the crystallographic information collected through XRD in an intuitive way, a stereographic projection of the different crystalline planes of Sapphire can be used. On this projection, all the measured features are indicated. In Figure B.2, such a projection is shown. On a stereographic projection of the crystalline planes of Sapphire, circles and straight lines can be used to represent respectively a Line (Φ) or tilt angle (Ψ) scan. A 2θ scan cannot be represented in a stereographic plot, it focuses on one crystalline plane and thus is equivalent to a dot in the stereographic plane.

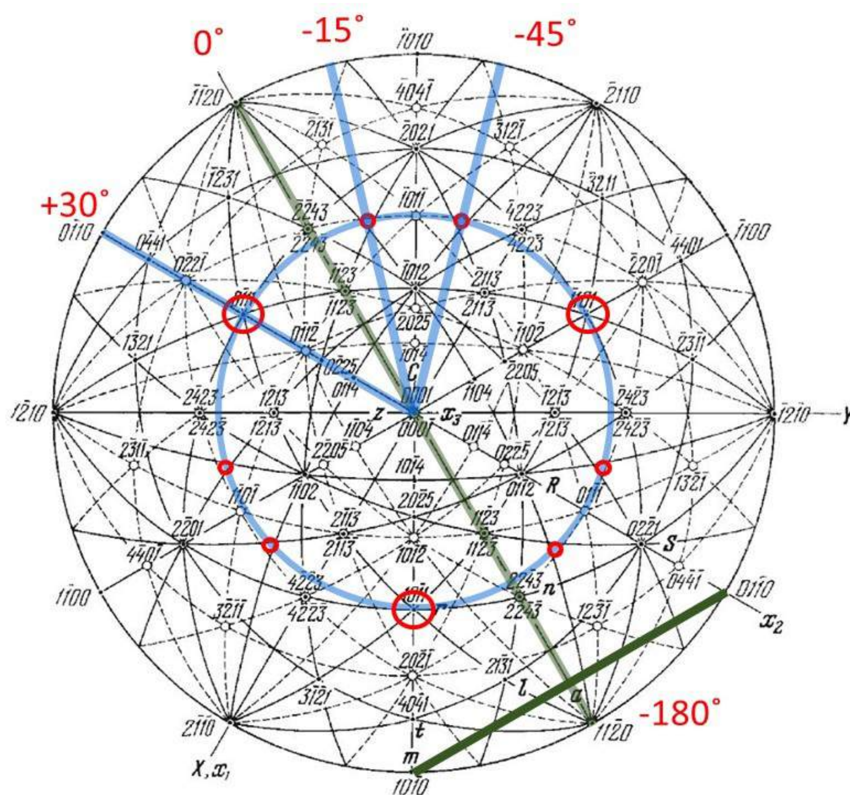

Figure B.2: Stereographic projection, with the c-plane taken as the reference plane (the centre). From Dobrovinska et al. [12].

In Figure B.2, the thick green line indicates one of the six possible positions for the Primary Flat Location, and is taken as the $-180°$ reference position for Phi scans. The blue circle represents the 360° Phi scan shown in Figure B.1. The red circles indicate the diffraction peaks, with their size giving the intensity of the peak. The straight blue lines represent tilt-angle scans (the Tilt angle varies when travelling on a radius of the stereographic projection), with their orientation in the Phi space given in red.

In the stereographic plane, the positions of the major crystalline planes is indicated with either a filled or an empty circle, with the coordinates of the concerned plane written next to it. Empty circles correspond to forbidden reflections (See Eqs. A.9), while filled circles should be visible in an XRD experiment. At some points, XRD signals are measured where no circle is drawn (the two minor peaks in the Phi scan). Drawing all the existing crystalline planes would overload the image, but not drawing them comes at the cost of completeness.

In the following discussion, an expression will be necessary for the angle between two

arbitrary planes of Sapphire $(h_1k_1i_1l_1)$ and $(h_2k_2i_2l_2)$. This Tilt angle between two crystalline planes $(h_1k_1i_1l_1)$ and $(h_2k_2i_2l_2)$, according to Lee et al. [75] is given by:

$$\Psi = cos^{-1}\left(\frac{h_1h_2 + k_1k_2 + \frac{1}{2} * (h_1k_2 + h_2k_1) + \frac{3}{4} * \frac{a^2}{c^2} * l_1l_2}{\sqrt{h_1^2 + k_1^2 + h_1k_1 + \frac{3}{4} * \frac{a^2}{c^2} * l_1^2}\sqrt{h_2^2 + k_2^2 + h_2k_2 + \frac{3}{4} * \frac{a^2}{c^2} * l_2^2}}\right) \quad \text{(B.1)}$$

The first feature of the Sapphire background signal which is investigated is the large peak at the Phi= +30° position. Notice that this peak is visible on the stereographic plot, and is due to the $\left(0\bar{1}11\right)$ plane of Sapphire. The two additional large peaks are attributed to $\left(\bar{1}101\right)$ and $\left(10\bar{1}1\right)$. These correspond to a allowed reflections, according to Eqs. A.9. The Tilt angle, i.e. the angle between this plane and the (0001) can be calculated with Eq B.1. The calculated value, 72.4°, is close to the measurement Tilt angle of 70.5°. In the Tilt angle scan of Figure B.3.a, this peak can indeed be seen at a value of 72.4°, and it is wide enough to be visible in a measurement. The 2θ angle can be calculated by using the interplanar distance for Sapphire (Eq A.12 yields a result $d_{(0\bar{1}11)} = 0.196\ nm$) and Bragg's law of diffraction (Eq A.7) yields a result $2\theta = 46.18°$ (the wavelength is the $Cu - K_\alpha$ wavelength and is equal to $\lambda = 0.1540598\ nm$). Note that this calculated value is not exactly equal to the measured value (In the 2θ scan, the peak is centered around 44°).

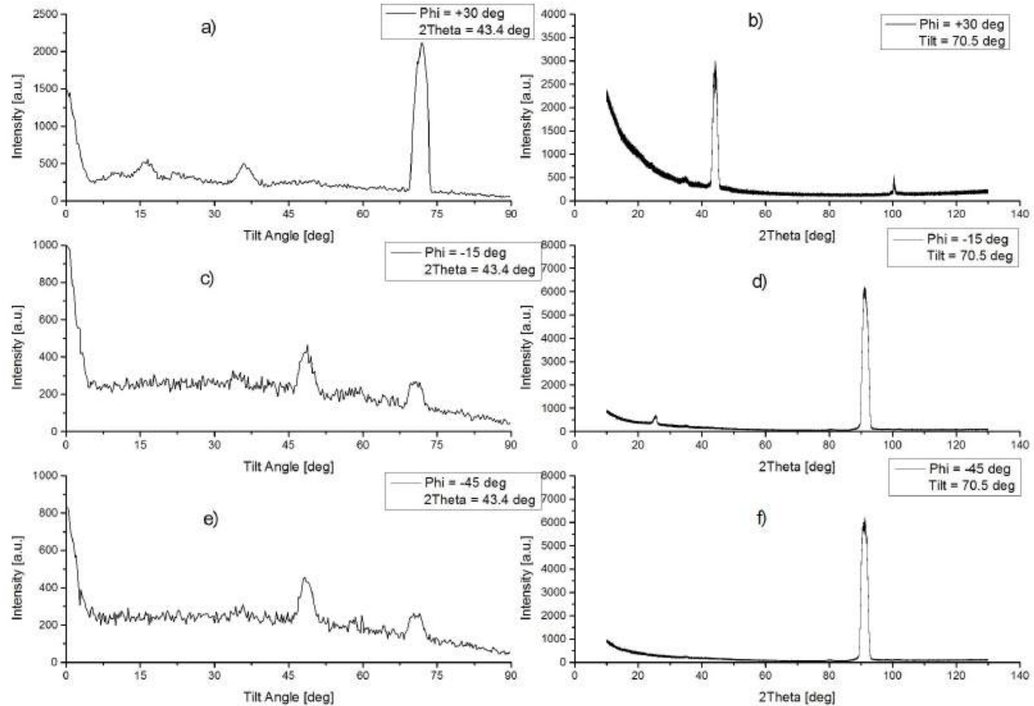

Figure B.3: Tilt angle and respective 2θ scans on a Sapphire substrate.

The two additional features (the smaller peaks at the $-15°$ and $-45°$ positions), are more problematic to explain. There are no indications in the stereographic plot of the crystalline plane that could be associated with those. The in-plane orientations corresponding to these two angles can be calculated using simple geometry: $\left(\bar{3}\bar{1}40\right)$ and $\left(\bar{4}130\right)$ (the 120° rotated versions of these two peaks are respectively $\left(\bar{1}4\bar{3}0\right)$ and $\left(4\bar{3}\bar{1}0\right)$; $\left(13\bar{4}0\right)$ and $\left(3\bar{4}10\right)$). If one calculates the exact Phi angle at which these planes should be visible, one finds $-16.1°$ instead of $-15°$ and $-43.9°$ instead of $-45°$. The attentive reader will have noticed this in the zoomed in characteristic in Figure B.1.

Now that the in-plane orientation of these two minor peaks has been determined, the elevation (given by the Tilt angle, or the l coordinate in the $hkil$ nomenclature of crystalline planes) can be calculated. The easiest way is to look for the allowed reflections that fit these directions. Choosing $l = 4$ yields such an allowed reflection. When the Tilt angle for $l = 4$ is calculated (take e.g. for $\left(\bar{3}\bar{1}44\right)$), equation B.1 yields a value of 70.61°. This value is close enough to the measurement Tilt angle: 70.5°. This calculation can be reproduced for all the in-plane orientations given in the previous paragraph, with $l = 4$.

Finally, the 2θ angle at which these planes should be visible can be calculated with the help of Bragg's Law, given the interplane distance is known. Before even calculating this value, one can say that, due to the high indices of the planes, the interplanar distance will be quite low. This will in turn be problematic for Bragg's law, which will yield a high 2θ angle. The calculated values indeed are: $d_{\left(\bar{3}\bar{1}40\right)} = 0.108\,nm$ and $2\theta = 91.2°$. Calculations for the other concerned planes yield the same results. According to Bragg's law of diffraction, the reflection of these planes should not be visible at a 2θ angle of 43.4°, where the measurement happens. The 2θ scans of Figure B.3 indeed show a large peak centered around $2\theta = 91.2°$, and, currently, no signal above the noise level for 2θ values close to the measurement value.

B.3 XRD characteristic of a $Cu\,(111)\,/\alpha - Al_2O_3\,(0001)$ stack

In this last section, the Phi characteristic of a $Cu\,(111)\,/\alpha - Al_2O_3\,(0001)$ stack will be analyzed, with as purpose the definition of the expected signals from the different ORs. As a reminder, this definition is given in Equation 2.2. Figure B.4 shows the expected signal, for OR-Ia.

In Figure B.4, the features for Cu are added in yellow. The yellow triangle represents the symmetry of the $Cu\,(111)$ unit cell. The orientation in this figure of the unit cell corresponds to OR-Ia (defined as $\left[\bar{1}10\right]_{Cu} \parallel \left[10\bar{1}0\right]_{\alpha}$, with the $\left[\bar{1}10\right]_{Cu}$ crystalline direction indicated by the yellow arrow). The expected signal for OR-Ia is given

by the yellow circles. Notice that the OR-II signal (specifically OR-IIb) would be superimposed on the major Sapphire peaks, rendering them invisible.

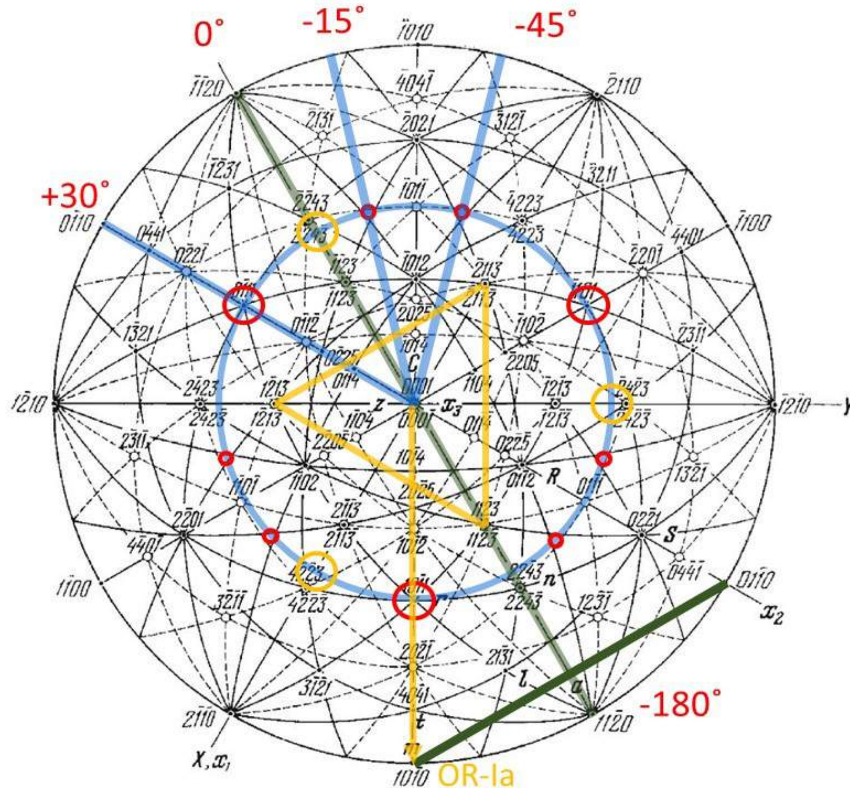

Figure B.4: Upgraded version of the stereographic procjection of Figure B.2. The stereographic projection is taken from [12].

Figure B.5 shows a superposition of the Cu and Sapphire signals. The three large peaks at positions $-60°$, $60°$ and $+-180°$ are attributed to the Cu signal. Most of the minor peaks can in turn be attributed to the Sapphire background. The position of the Cu peaks indicates that the deposited layer is OR-Ib oriented, as opposed to the OR-Ia shown in Figure B.4. Indeed, since they both are thermodynamically equivalent, it should not be surprising that they can both result from the same procedure. Very small OR-Ia peaks are nevertheless visible (the clearest one is located at $\Phi = 0°$). Note that these peaks are more than three orders of magnitude lower. They are due to very small OR-Ia grains inside the spot. The spot size of the X-Ray beam on the sample is relatively large (X-Rays are impossible to focus by conventional means, and the sample is not perpendicular to the beam during a Phi scan), close to the size of the wafer. The defects which are systematically located at the edges of the sample could therefore be visible in a Phi scan, given that the noise level is low enough.The definitions of the ORs are given again hereunder:

$$
\begin{aligned}
OR-Ia \equiv (111)_{Cu} \parallel (0001)_{\alpha} \quad & \wedge \quad \left[\bar{1}10\right]_{Cu} \parallel \left[10\bar{1}0\right]_{\alpha} \\
& \vee \quad \left[\bar{1}10\right]_{Cu} \parallel \left[0\bar{1}10\right]_{\alpha} \\
& \vee \quad \left[\bar{1}10\right]_{Cu} \parallel \left[\bar{1}100\right]_{\alpha} \\
OR-Ib \equiv (111)_{Cu} \parallel (0001)_{\alpha} \quad & \wedge \quad \left[\bar{1}10\right]_{Cu} \parallel \left[1\bar{1}00\right]_{\alpha} \\
& \vee \quad \left[\bar{1}10\right]_{Cu} \parallel \left[\bar{1}010\right]_{\alpha} \\
& \vee \quad \left[\bar{1}10\right]_{Cu} \parallel \left[01\bar{1}0\right]_{\alpha} \\
OR-IIa \equiv (111)_{Cu} \parallel (0001)_{\alpha} \quad & \wedge \quad \left[\bar{1}10\right]_{Cu} \parallel \left[2\bar{1}\bar{1}0\right]_{\alpha} \\
& \vee \quad \left[\bar{1}10\right]_{Cu} \parallel \left[\bar{1}\bar{1}20\right]_{\alpha} \\
& \vee \quad \left[\bar{1}10\right]_{Cu} \parallel \left[\bar{1}2\bar{1}0\right]_{\alpha} \\
OR-IIb \equiv (111)_{Cu} \parallel (0001)_{\alpha} \quad & \wedge \quad \left[\bar{1}10\right]_{Cu} \parallel \left[1\bar{2}10\right]_{\alpha} \\
& \vee \quad \left[\bar{1}10\right]_{Cu} \parallel \left[\bar{2}110\right]_{\alpha} \\
& \vee \quad \left[\bar{1}10\right]_{Cu} \parallel \left[11\bar{2}0\right]_{\alpha}
\end{aligned}
$$

B.4 Conclusion

This appendix provides the necessary tools for deriving all the information contained in an XRD Phi scan. This information of of capital importance for assessing the quality of the crystalline structure of the sputterred and annealed Cu layers.

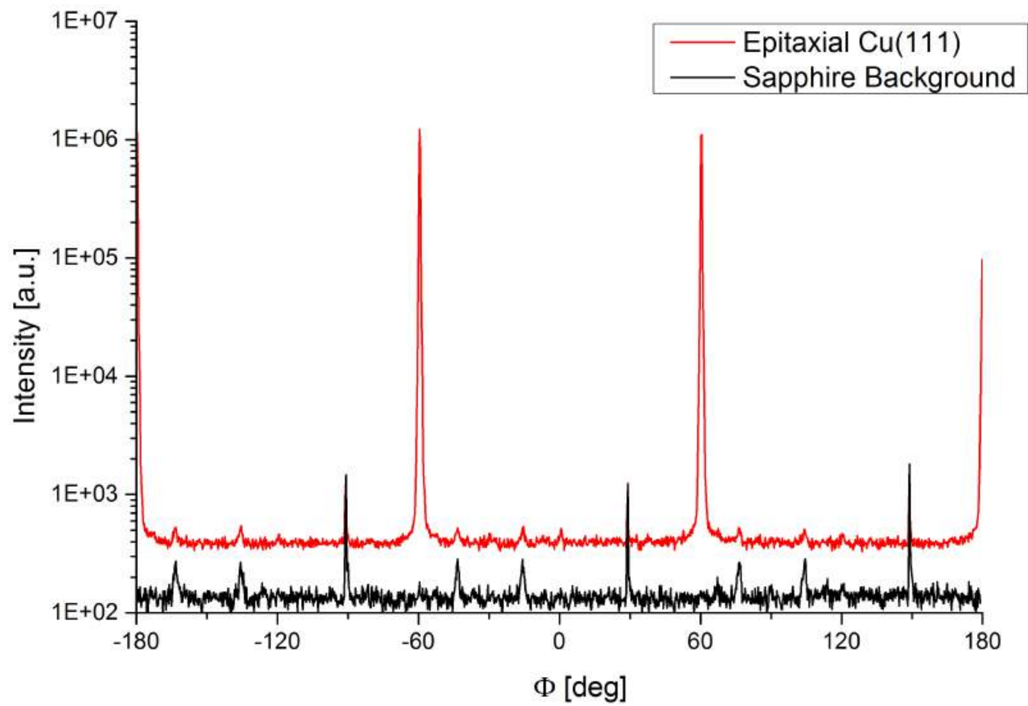

Figure B.5: Phi scan of an epitaxial $Cu\,(111)$ layer on Sapphire. Both the curves of Cu and the Sapphire background are shown.

Appendix C

Additional Figures

In this Appendix, additional figures will be shown. These do not contain capital information, but can be useful in understanding some of the concepts or conclusions of this thesis.

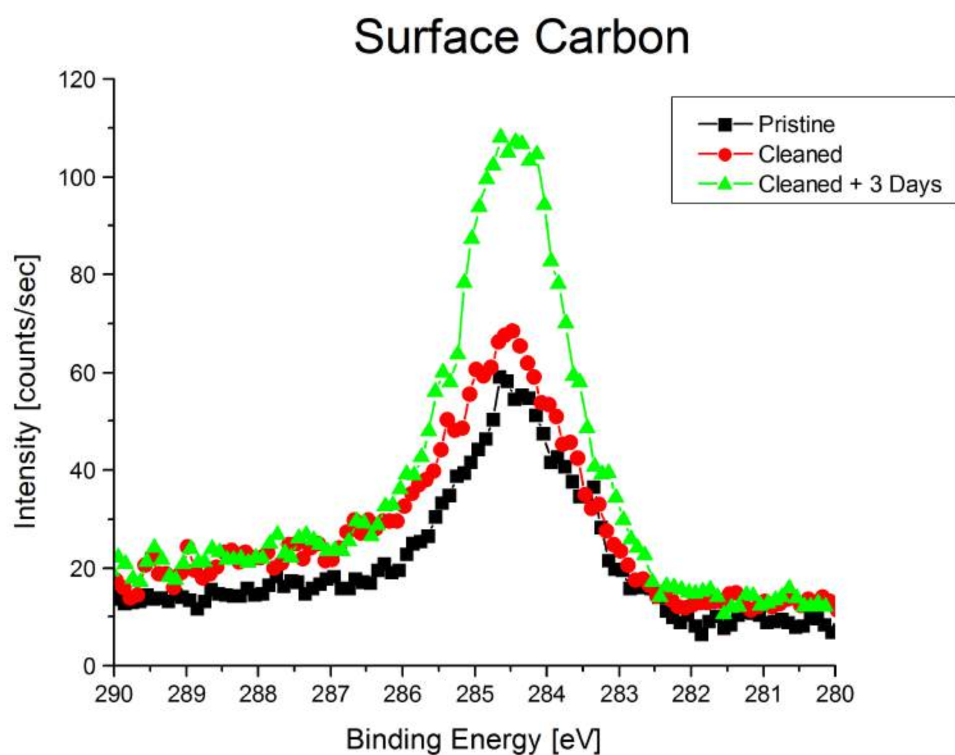

Figure C.1: Surface XPS spectra for C on pristine Sapphire wafers, after a chemical clean, and after three days of ageing in a Teflon container.

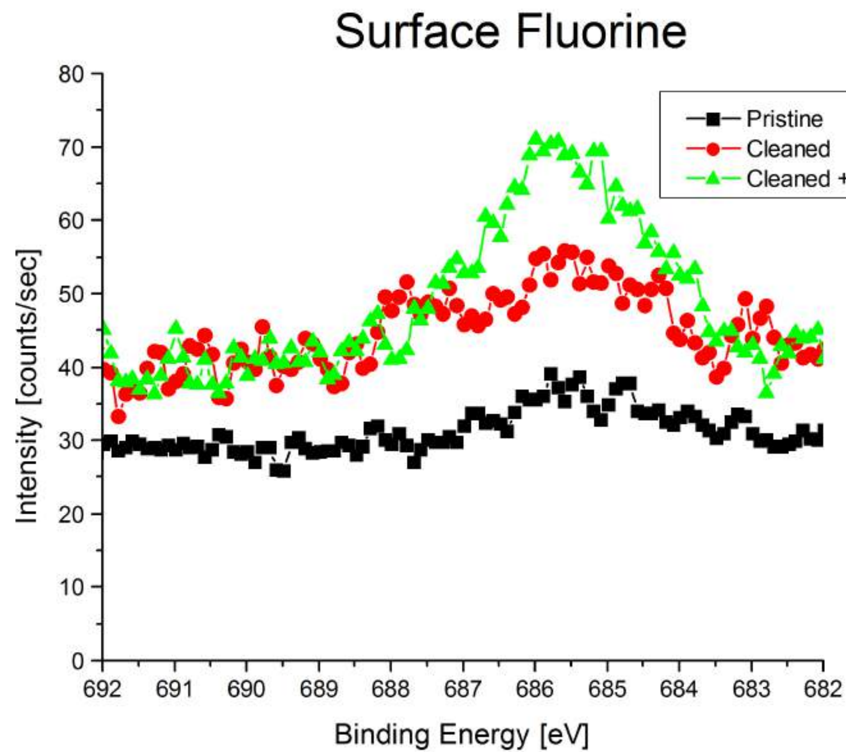

Figure C.2: Surface XPS spectra for F on pristine Sapphire wafers, after a chemical clean, and after three days of ageing in a Teflon container.

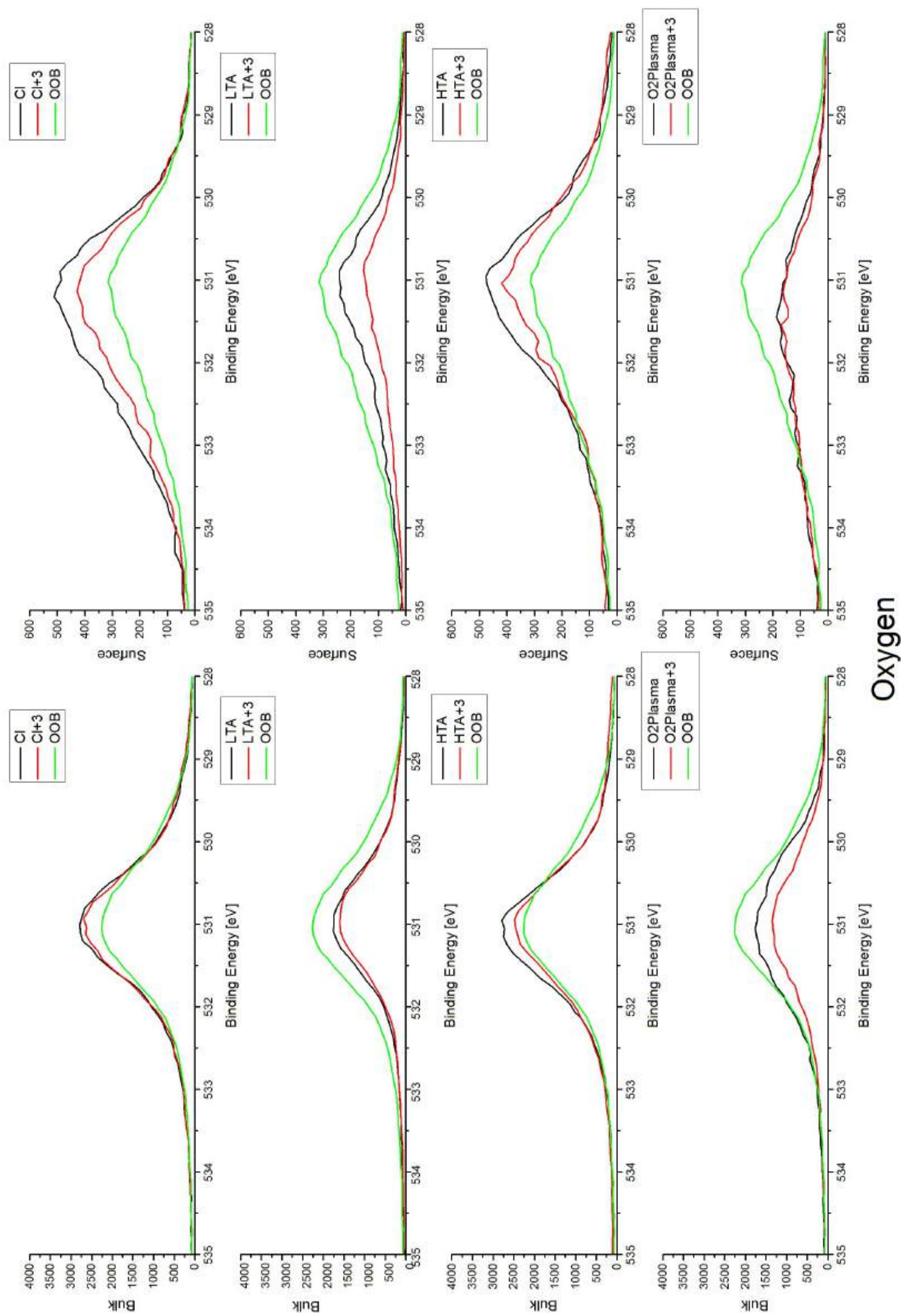

Figure C.3: XPS spectra for Oxygen.

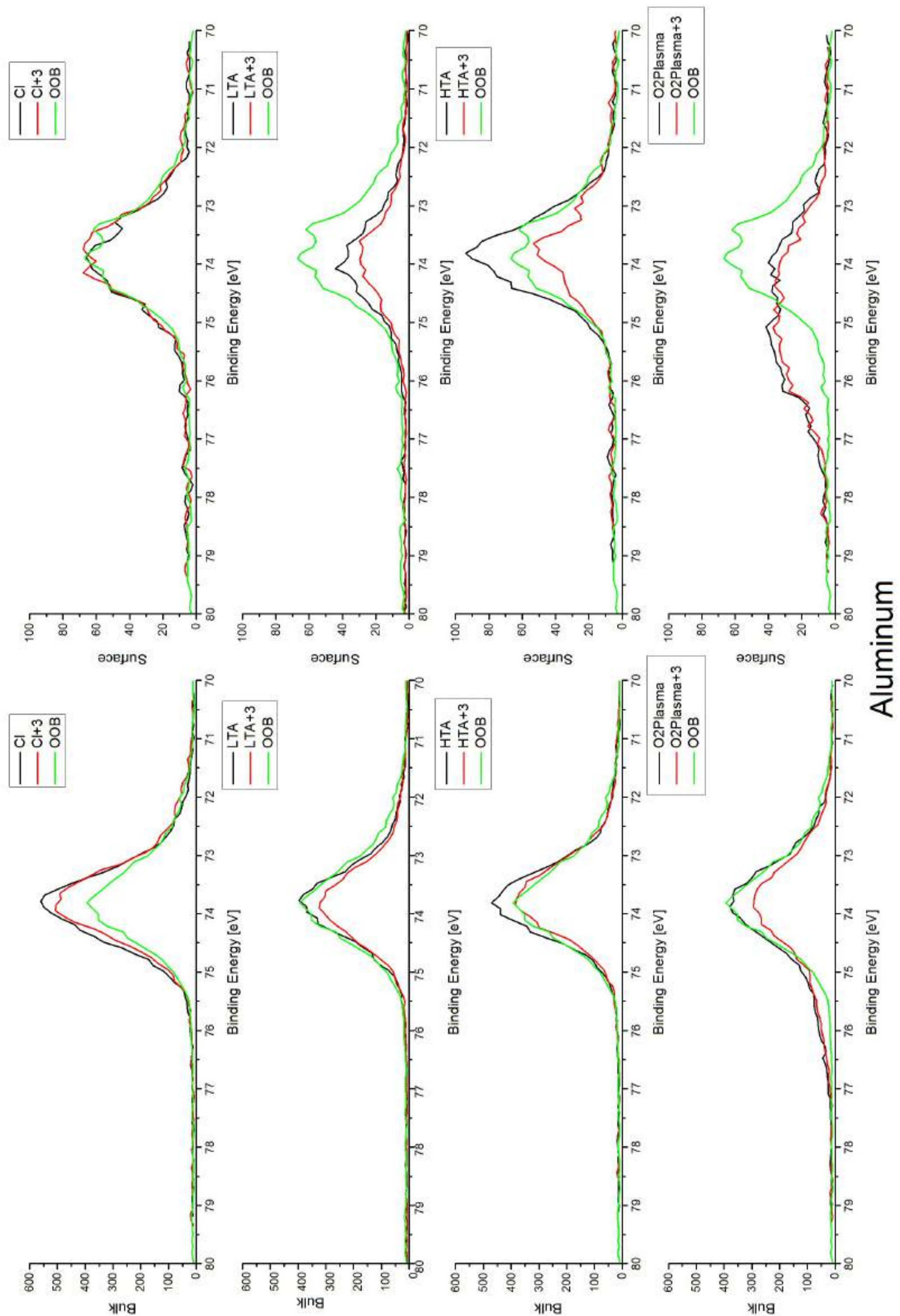

Figure C.4: XPS spectra for Aluminum.

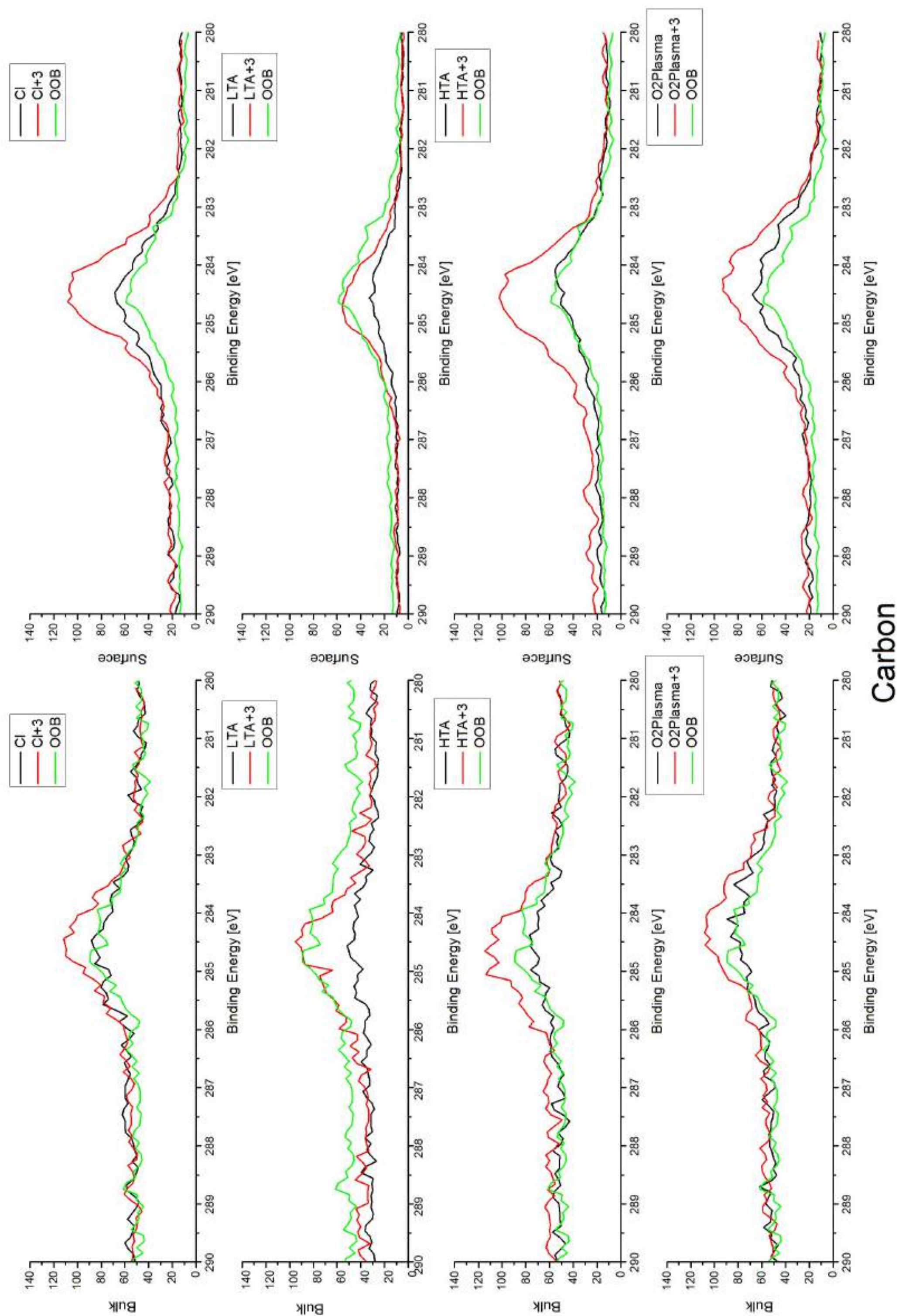

Figure C.5: XPS spectra for Carbon.

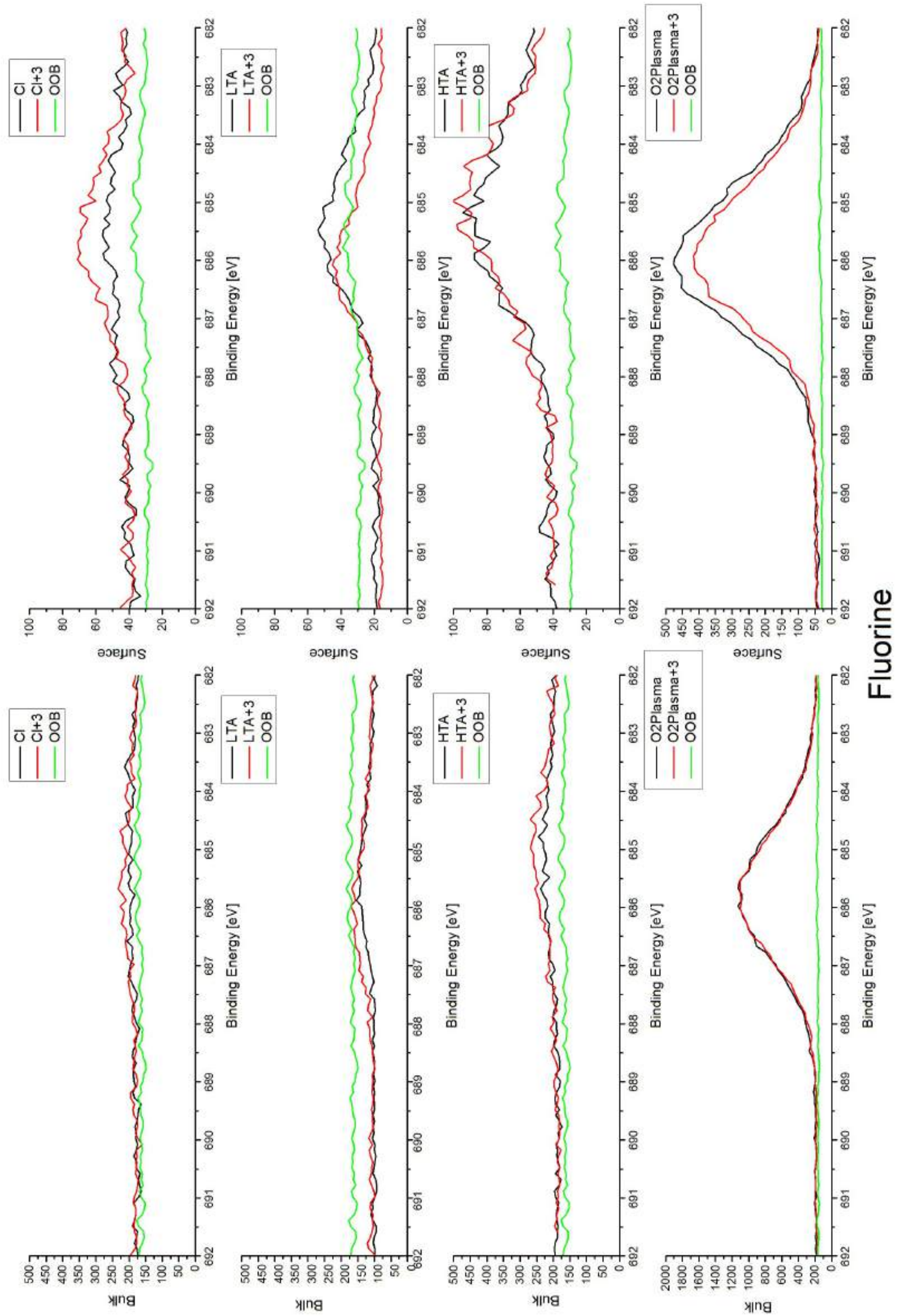

Figure C.6: XPS spectra for Fluorine.

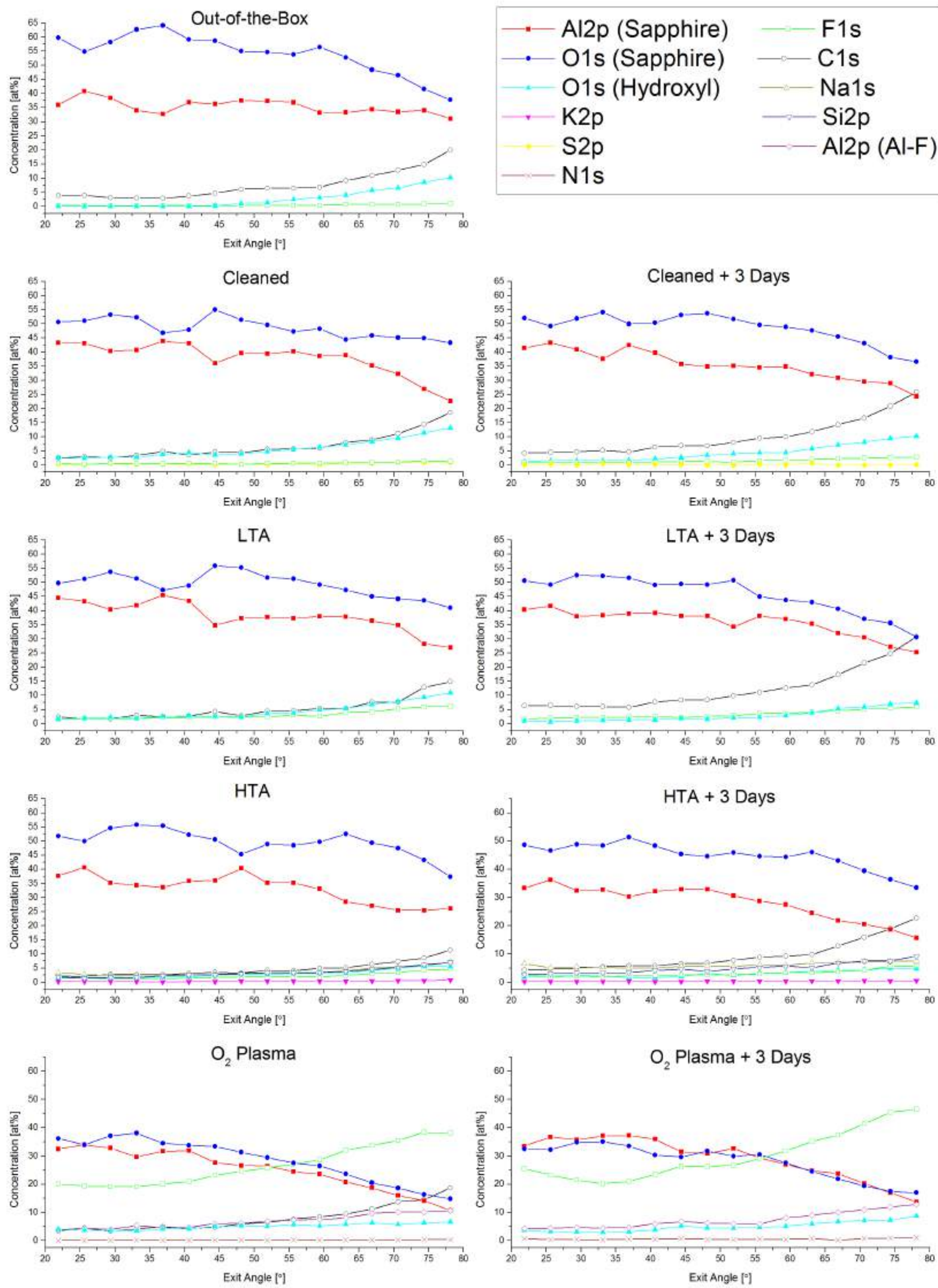

Figure C.7: XPS profiles derived from the XPS spectra.

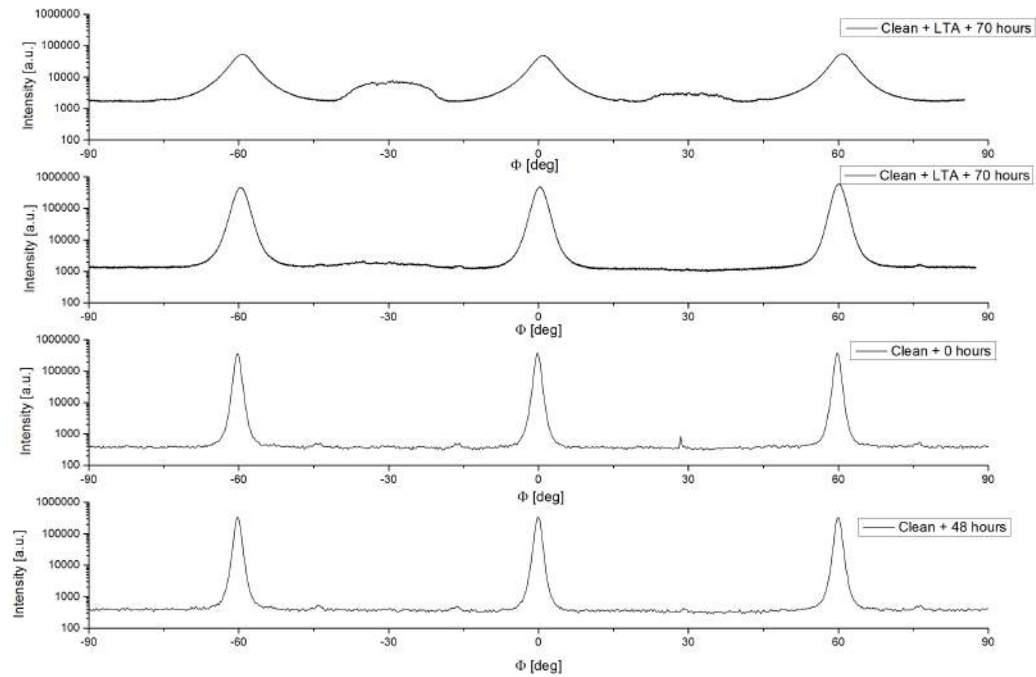

Figure C.8: XRD Phi scan of the relative stability of the Oxygen and Aluminum terminations. The two first samples underwent exactly the same treatment and underwent Cu sputtering at exactly the same parameters. Nevertheless, due to the unstabel O termination, the results vary very strongly. The two last samples were simply cleaned, and then underwent Cu sputtering after the indicated time. The sputtering parameters were different than those of the two first samples. Regardless of the time spent before Cu deposition, the results are identical, as opposed to the results of the Oxygen annealed samples.

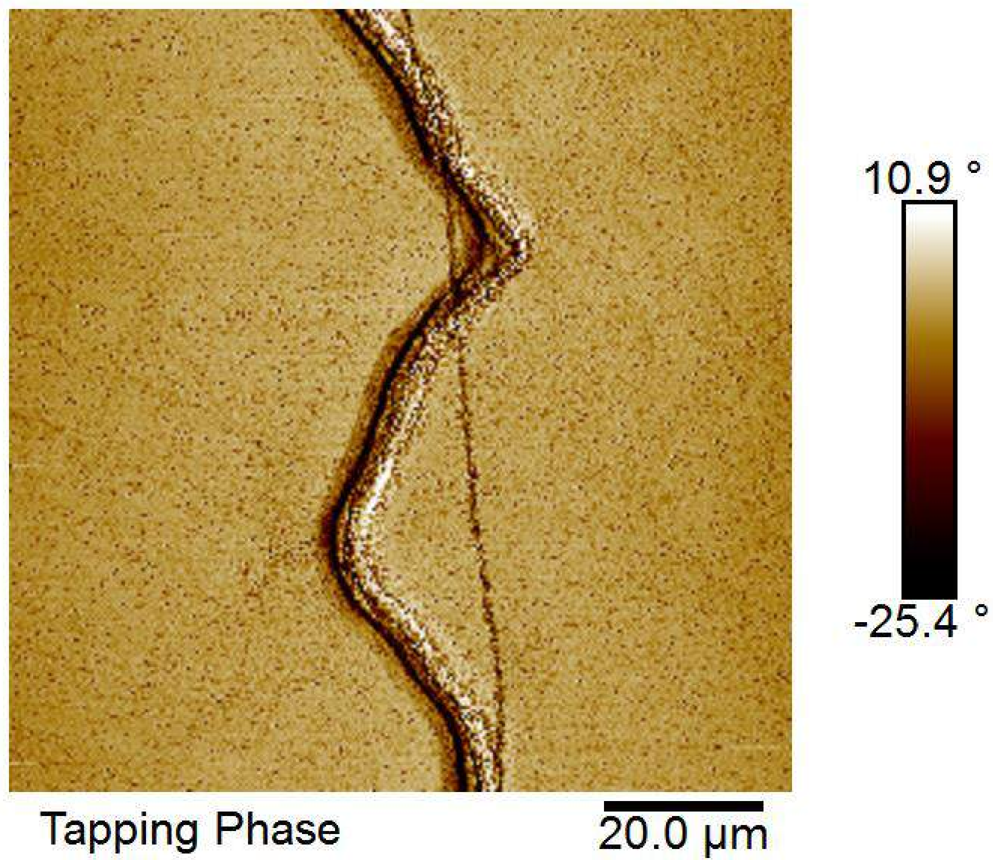

Figure C.9: Phase image of a Cu grain boundary. The diagonal stripe in the middle of the figure is ascribed to a Graphene grain boundary. Original figure is Figure 5.7d.

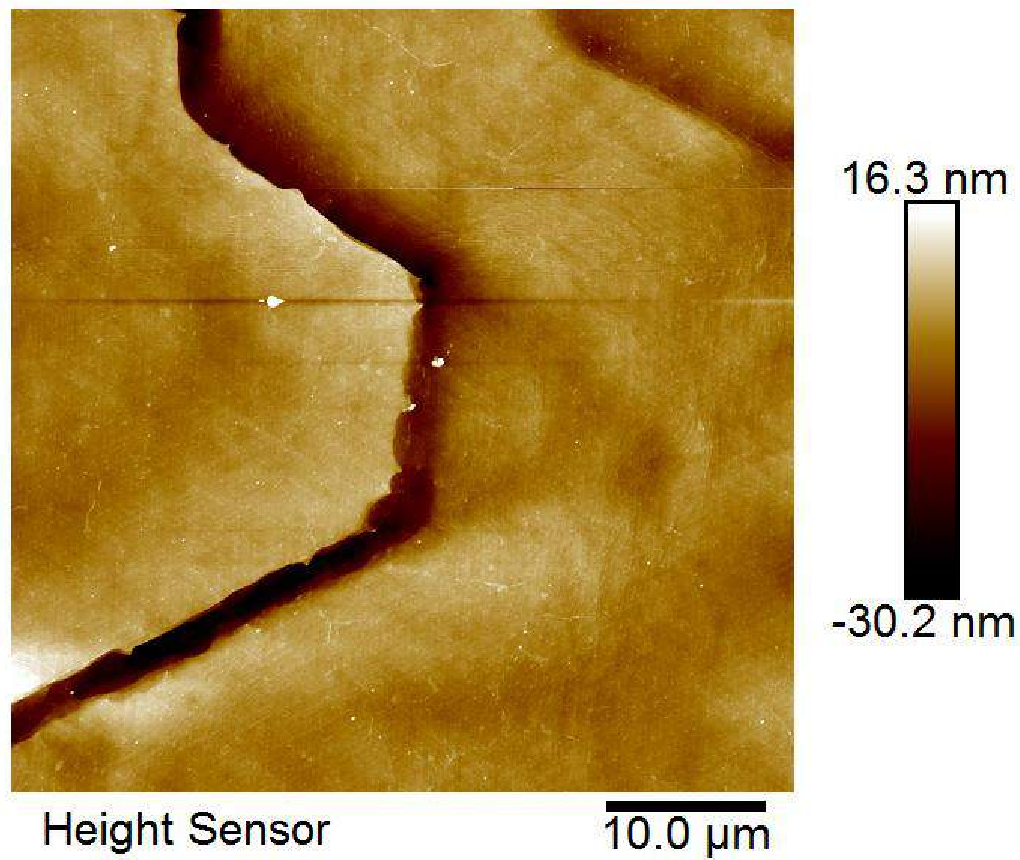

Figure C.10: AFM investigation of a grain boundary in an epitaxially grown *Cu* on Sapphire sample. The angle of 60° between the grain boundaries can be clearly seen in this image. The grain boundaries are approximately 30 *nm* deep, but are nevertheless visible under an optical microscope.

Bibliography

[1] D.L. Miller, M.W. Keller, J.M. Shaw, K.P. Rice, R.R. Keller, and K.M. Diederichsen. Giant secondary grain growth in Cu films on Sapphire. *AIP Advances*, 3(8), 2013.

[2] A.H. Castro Neto, F. Guinea, N.M.R. Peres, K.S. Novoselov, and A.K. Geim. The electronic properties of Graphene. *Reviews of Modern Physics*, 81(1):109, 2009.

[3] H. Ago, K. Kawahara, Y. Ogawa, S. Tanoue, M.A. Bissett, M. Tsuji, H. Sakaguchi, R.J. Koch, F. Fromm, T. Seyller, et al. Epitaxial growth and electronic properties of large hexagonal Graphene domains on Cu(111) thin film. *Applied Physics Express*, 6(7):075101, 2013.

[4] S. Curiotto, H. Chien, H. Meltzman, P. Wynblatt, G.S. Rohrer, W.D. Kaplan, and D. Chatain. Orientation relationships of Copper crystals on c-plane Sapphire. *Acta Materialia*, 59(13):5320–5331, 2011.

[5] J.A. Thornton. Influence of apparatus geometry and deposition conditions on the structure and topography of thick sputtered coatings. *Journal of Vacuum Science & Technology*, 11(4):666–670, 1974.

[6] E.A. Soares, M.A. Van Hove, C.F. Walters, and K.F. McCarty. Structure of the α-Al_2O_3(0001) surface from low-energy electron diffraction: Al termination and evidence for anomalously large thermal vibrations. *Physical Review B*, 65(19):195405, 2002.

[7] M.L. Kronberg. Plastic deformation of single crystals of Sapphire: basal slip and twinning. *Acta Metallurgica*, 5(9):507–524, 1957.

[8] P.J. Eaton and P. West. *Atomic Force Microscopy*, volume 10. Oxford University Press Oxford, 2010.

[9] W. Vandervorst and H. Bender. Fysische materiaalkarakterisatie voor elektronische componenten. www.toledo.kuleuven.be, 2015. Course ID H03O4a.

[10] K.E. Van Holde, W.C. Johnson, P.S. Ho, et al. *Principles of Physical Biochemistry*. Pearson/Prentice Hall Upper Saddle River, NJ, 2006.

[11] T.F. Chung, T. Shen, H. Cao, L.A. Jauregui, W. Wu, Q. Yu, D. Newell, and Y.P. Chen. Synthetic Graphene grown by Chemical Vapor Deposition on Copper foils. *International Journal of Modern Physics B*, 27(10), 2013.

[12] E.R. Dobrovinskaya, L.A. Lytvynov, and V. Pishchik. *Sapphire: material, manufacturing, applications*. Springer Science & Business Media, 2009.

[13] J.R. Davis et al. *Copper and Copper alloys*. ASM international, 2001.

[14] K.S. Novoselov, A.K. Geim, S.V. Morozov, D. Jiang, Y. Zhang, S.V. Dubonos, I.V. Grigorieva, and A.A. Firsov. Electric field effect in atomically thin Carbon films. *Science*, 306(5696):666–669, 2004.

[15] F. Xia, D.B. Farmer, Y. Lin, and P. Avouris. Graphene field-effect transistors with high on/off current ratio and large transport band gap at room temperature. *Nano Letters*, 10(2):715–718, 2010.

[16] S. Sato. Graphene for nanoelectronics. *Japanese Journal of Applied Physics*, 54(4):040102, 2015.

[17] J. Brandenburg, R. Hühne, L. Schultz, and V. Neu. Domain structure of epitaxial Co films with perpendicular anisotropy. *Physical Review B*, 79(5):054429, 2009.

[18] J. Lahiri, T. Miller, L. Adamska, I.I. Oleynik, and M. Batzill. Graphene growth on Ni(111) by transformation of a surface carbide. *Nano Letters*, 11(2):518–522, 2010.

[19] J. Coraux, M. Engler, C. Busse, D. Wall, N. Buckanie, F.J.M. Zu Heringdorf, R. Van Gastel, B. Poelsema, T. Michely, et al. Growth of graphene on Ir(111). *New Journal of Physics*, 11(2):023006, 2009.

[20] P. Sutter, J.T. Sadowski, and E. Sutter. Graphene on Pt(111): Growth and substrate interaction. *Physical Review B*, 80(24):245411, 2009.

[21] B. Chen, H. Huang, X. Ma, L. Huang, Z. Zhang, and L.M. Peng. How good can CVD-grown monolayer Graphene be? *Nanoscale*, 6:15255–15261, 2014.

[22] P.W. Sutter, J.I. Flege, and E.A. Sutter. Epitaxial Graphene on Ruthenium. *Nature Materials*, 7(5):406–411, 2008.

[23] L. Gao, J.R. Guest, and N.P. Guisinger. Epitaxial Graphene on Cu(111). *Nano Letters*, 10(9):3512–3516, 2010.

[24] S.Y. Kwon, C.V. Ciobanu, V. Petrova, V.B. Shenoy, J. Bareno, V. Gambin, I. Petrov, and S. Kodambaka. Growth of semiconducting Graphene on Palladium. *Nano Letters*, 9(12):3985–3990, 2009.

[25] J.H. Lee, E.K. Lee, W.J. Joo, Y. Jang, B.S. Kim, J.Y. Lim, S.H. Choi, S.J. Ahn, J.R. Ahn, M.H. Park, et al. Wafer-scale growth of single-crystal monolayer Graphene on reusable Hydrogen-terminated Germanium. *Science*, 344(6181):286–289, 2014.

[26] S. Bhaviripudi, X. Jia, M.S. Dresselhaus, and J. Kong. Role of kinetic factors in Chemical Vapor Deposition synthesis of uniform large area Graphene using Copper catalyst. *Nano Letters*, 10(10):4128–4133, 2010.

[27] H.K. Yu, K. Balasubramanian, K. Kim, J.L. Lee, M. Maiti, C. Ropers, J. Krieg, K. Kern, and A.M. Wodtke. Chemical Vapor Deposition of Graphene on a peeled-off epitaxial Cu(111) foil: A simple approach to improved properties. *ACS Nano*, 8(8):8636–8643, 2014.

[28] C.P. Khattak, P.J. Guggenheim, and F. Schmid. Growth of 15-inch diameter Sapphire boules. In *AeroSense 2003*, pages 47–53. International Society for Optics and Photonics, 2003.

[29] S.H. Oh, C. Scheu, T. Wagner, and M. Rühle. Control of bonding and epitaxy at Copper/Sapphire interface. *Applied Physics Letters*, 91(14):141912, 2007.

[30] B. Hu, H. Ago, Y. Ito, K. Kawahara, M. Tsuji, E. Magome, K. Sumitani, N. Mizuta, K. Ikeda, and S. Mizuno. Epitaxial growth of large-area single-layer Graphene over Cu(111)/Sapphire by atmospheric pressure CVD. *Carbon*, 50(1):57–65, 2012.

[31] D.L. Miller, M.W. Keller, J.M. Shaw, A.N. Chiaramonti, and R.R. Keller. Epitaxial (111) films of Cu, Ni, and Cu_xNi_y on α-$Al_2O_3(0001)$ for Graphene growth by Chemical Vapor Deposition. *Journal of Applied Physics*, 112(6):064317, 2012.

[32] Y. Lee, S. Bae, H. Jang, S. Jang, S.E. Zhu, S.H. Sim, Y.I. Song, B.H. Hong, and J.H. Ahn. Wafer-scale synthesis and transfer of Graphene films. *Nano Letters*, 10(2):490–493, 2010.

[33] W. Liu, H. Li, C. Xu, Y. Khatami, and K. Banerjee. Synthesis of high-quality monolayer and bilayer Graphene on Copper using Chemical Vapor Deposition. *Carbon*, 49(13):4122–4130, 2011.

[34] L. Gao, W. Ren, H. Xu, L. Jin, Z. Wang, T. Ma, L. Ma, Z. Zhang, Q. Fu, L.M. Peng, et al. Repeated growth and bubbling transfer of Graphene with millimetre-size single-crystal grains using Platinum. *Nature Communications*, 3:699, 2012.

[35] C. Scheu, M. Gao, S.H. Oh, G. Dehm, S. Klein, A.P. Tomsia, and M. Rühle. Bonding at Copper–Alumina interfaces established by different surface treatments: a critical review. *Journal of Materials Science*, 41(16):5161–5168, 2006.

[36] S.H. Oh, C. Scheu, T. Wagner, E. Tchernychova, and M. Rühle. Epitaxy and bonding of Cu films on Oxygen-terminated α-$Al_2O_3(0001)$ surfaces. *Acta Materialia*, 54(10):2685–2696, 2006.

[37] G. Dehm, H. Edongue, T. Wagner, S.H. Oh, and E. Arzt. Obtaining different orientation relationships for Cu films grown on α-$Al_2O_3(0001)$ substrates by magnetron sputtering. *Zeitschrift für Metallkunde*, 96(3):249–254, 2005.

[38] S. Lee, J.Y. Kim, T.W. Lee, W.K. Kim, B.S. Kim, J.H. Park, J.S. Bae, Y.C. Cho, J. Kim, M.W. Oh, et al. Fabrication of high-quality single-crystal Cu thin films using radio-frequency sputtering. *Scientific Reports*, 4, 2014.

[39] F. Cuccureddu, S. Murphy, I.V. Shvets, M. Porcu, H.W. Zandbergen, N.S. Sidorov, and S.I. Bozhko. Surface morphology of c-plane Sapphire (α-Alumina) produced by high temperature anneal. *Surface Science*, 604(15):1294–1299, 2010.

[40] I. Batyrev, A. Alavi, and M.W. Finnis. Ab initio calculations on the $Al_2O_3(0001)$ surface. *Faraday Discussions*, 114:33–43, 1999.

[41] X.G. Wang, A. Chaka, and M. Scheffler. Effect of the environment on α-$Al_2O_3(0001)$ surface structures. *Physical Review Letters*, 84(16):3650, 2000.

[42] S. Blonski and S.H. Garofalini. Molecular dynamics simulations of α-Alumina and γ-Alumina surfaces. *Surface Science*, 295(1):263–274, 1993.

[43] A. Hashibon, C. Elsässer, and M. Rühle. Structure at abrupt Copper–Alumina interfaces: An ab initio study. *Acta Materialia*, 53(20):5323–5332, 2005.

[44] C. Niu, K. Shepherd, D. Martini, J. Tong, J.A. Kelber, D.R. Jennison, and A. Bogicevic. Cu interactions with α-$Al_2O_3(0001)$: effects of surface hydroxyl groups versus dehydroxylation by Ar-ion sputtering. *Surface Science*, 465(1):163–176, 2000.

[45] J.A. Kelber, C. Niu, K. Shepherd, D.R. Jennison, and A. Bogicevic. Copper wetting of α-$Al_2O_3(0001)$: Theory and experiment. *Surface Science*, 446(1):76–88, 2000.

[46] J.F. Sanz and N.C. Hernández. Mechanism of Cu deposition on the α-$Al_2O_3(0001)$ surface. *Physical Review Letters*, 94(1):016104, 2005.

[47] F. Dwikusuma, D. Saulys, and T.F. Kuech. Study on Sapphire surface preparation for III-nitride heteroepitaxial growth by chemical treatments. *Journal of The Electrochemical Society*, 149(11):G603–G608, 2002.

[48] S. Curiotto and D. Chatain. Surface morphology and composition of c-, a-and m-Sapphire surfaces in O_2 and H_2 environments. *Surface Science*, 603(17):2688–2697, 2009.

[49] O. Kurnosikov, L. Pham Van, and J. Cousty. High-temperature transformation of vicinal (0001)-Al_2O_3-α surfaces: an AFM study. *Surface and Interface Analysis*, 29(9):608–613, 2000.

[50] T. Kimoto, A. Itoh, and H. Matsunami. Step bunching in Chemical Vapor Deposition of 6H– and 4H–SiC on vicinal SiC(0001) faces. *Applied Physics Letters*, 66(26):3645–3647, 1995.

[51] P.R. Ribič and G. Bratina. Behavior of the (0001) surface of Sapphire upon high-temperature annealing. *Surface Science*, 601(1):44–49, 2007.

[52] M. Yoshimoto, T. Maeda, T. Ohnishi, H. Koinuma, O. Ishiyama, M. Shinohara, M. Kubo, R. Miura, and A. Miyamoto. Atomic-scale formation of ultrasmooth surfaces on Sapphire substrates for high-quality thin-film fabrication. *Applied Physics Letters*, 67(18):2615–2617, 1995.

[53] C.V. Vasant Kumar and A. Mansingh. Effect of target-to-substrate distance on the growth and properties of RF-sputtered Indium Tin Oxide films. *Journal of Applied Physics*, 65(3), 1989.

[54] V. Assuncao, E. Fortunato, A. Marques, H. Aguas, I. Ferreira, M.E.V. Costa, and R. Martins. Influence of the deposition pressure on the properties of transparent and conductive ZnO: Ga thin-film produced by RF sputtering at room temperature. *Thin Solid Films*, 427(1):401–405, 2003.

[55] V. Chawla, R. Jayaganthan, and R. Chandra. Influence of sputtering pressure on the structure and mechanical properties of nanocomposite Ti-Si-N thin films. *Journal of Materials Science & Technology*, 26(8):673–678, 2010.

[56] J.A. Thornton. Influence of substrate temperature and deposition rate on structure of thick sputtered Cu coatings. *Journal of Vacuum Science & Technology*, 12(4):830–835, 1975.

[57] V. Chawla, R. Jayaganthan, A.K. Chawla, and R. Chandra. Microstructural characterizations of magnetron sputtered Ti films on glass substrate. *Journal of Materials Processing Technology*, 209(7):3444–3451, 2009.

[58] Z. Sun, Z. Yan, J. Yao, E. Beitler, Y. Zhu, and J.M. Tour. Growth of Graphene from solid Carbon sources. *Nature*, 468(7323):549–552, 2010.

[59] A. Guermoune, T. Chari, F. Popescu, S.S. Sabri, J. Guillemette, H.S. Skulason, T. Szkopek, and M. Siaj. Chemical Vapor Deposition synthesis of Graphene on Copper with Methanol, Ethanol, and Propanol precursors. *Carbon*, 49(13):4204–4210, 2011.

[60] X. Li, C.W. Magnuson, A. Venugopal, J. An, J.W. Suk, B. Han, M. Borysiak, W. Cai, A. Velamakanni, Y. Zhu, et al. Graphene films with large domain size by a two-step Chemical Vapor Deposition process. *Nano Letters*, 10(11):4328–4334, 2010.

[61] G. Nandamuri, S. Roumimov, and R. Solanki. Chemical Vapor Deposition of Graphene films. *Nanotechnology*, 21(14):145604.

[62] H. Wang, G. Wang, P. Bao, S. Yang, W. Zhu, X. Xie, and W.J. Zhang. Controllable synthesis of submillimeter single-crystal monolayer Graphene domains on Copper foils by suppressing nucleation. *Journal of the American Chemical Society*, 134(8):3627–3630, 2012.

[63] M. Regmi, M.F. Chisholm, and G. Eres. The effect of growth parameters on the intrinsic properties of large-area single layer Graphene grown by Chemical Vapor Deposition on Cu. *Carbon*, 50(1):134–141, 2012.

[64] K.M. Reddy, A.D. Gledhill, C.H. Chen, J.M. Drexler, and N.P. Padture. High quality, transferrable Graphene grown on single crystal Cu(111) thin films on basal-plane Sapphire. *Applied Physics Letters*, 98(11):113117, 2011.

[65] S. Nie, W. Wu, S. Xing, Q. Yu, J. Bao, S. Pei, and K.F. McCarty. Growth from below: bilayer Graphene on Copper by Chemical Vapor Deposition. *New Journal of Physics*, 14(9):093028, 2012.

[66] C.M. Orofeo, H. Hibino, K. Kawahara, Y. Ogawa, M. Tsuji, K. Ikeda, S. Mizuno, and H. Ago. Influence of Cu metal on the domain structure and carrier mobility in single-layer Graphene. *Carbon*, 50(6):2189–2196, 2012.

[67] H.I. Rasool, E.B. Song, M.J. Allen, J.K. Wassei, R.B. Kaner, K.L. Wang, B.H. Weiller, and J.K. Gimzewski. Continuity of Graphene on polycrystalline Copper. *Nano Letters*, 11(1):251–256, 2010.

[68] Q. Yu, L.A. Jauregui, W. Wu, R. Colby, J. Tian, Z. Su, H. Cao, Z. Liu, D. Pandey, D. Wei, et al. Control and characterization of individual grains and grain boundaries in Graphene grown by Chemical Vapour Deposition. *Nature Materials*, 10(6):443–449, 2011.

[69] J.M. Wofford, S. Nie, K.F. McCarty, N.C. Bartelt, and O.D. Dubon. Graphene islands on Cu foils: the interplay between shape, orientation, and defects. *Nano Letters*, 10(12):4890–4896, 2010.

[70] X. Li, W. Cai, L. Colombo, and R.S. Ruoff. Evolution of Graphene growth on Ni and Cu by Carbon isotope labeling. *Nano Letters*, 9(12):4268–4272, 2009.

[71] Sapphire substrates retailer. www.roditi.com/SingleCrystal/Sapphire/C-Plane.html. Accessed: 27/03/2015.

[72] A. Arranz, C. Palacio, D. Garcia-Fresnadillo, G. Orellana, A. Navarro, and E. Munoz. Influence of surface hydroxylation on 3-aminopropyltriethoxysilane growth mode during chemical functionalization of GaN surfaces: an angle-resolved X-Ray Photoelectron Spectroscopy study. *Langmuir*, 24(16):8667–8671, 2008.

[73] N. Oyabu, O. Custance, I. Yi, Y. Sugawara, and S. Morita. Mechanical vertical manipulation of selected single atoms by soft nanoindentation using near contact atomic force microscopy. *Physical Review Letters*, 90(17):176102, 2003.

[74] D.W.L. Hukins et al. *X-Ray Diffraction by disordered and ordered systems.* Pergamon Press, 1981.

[75] W.E. Lee and K.P.D. Lagerlof. Structural and electron diffraction data for Sapphire (α-Al_2O_3). *Journal of electron microscopy technique*, 2(3):247–258, 1985.

[76] N.K. Verma. *Physics for Engineers.* PHI Learning, 2013.